Search for baryons with two charm quarks

by Mark Edward Mattson

A Dissertation

Submitted to the Department of Physics,
Mellon College of Science,
in partial fulfillment of the requirements for the degree of

Doctor of Philosophy

Carnegie Mellon University
April 2002

Thesis Supervisor: Professor James Russ

Abstract

Using data from the SELEX experiment, we searched for baryons having two charm quarks. No one has yet observed a doubly-charmed baryon. We investigated the reconstruction $\Lambda_c^+ K^- \pi^+ \pi^+$, a decay mode consistent with a baryon having *ccu* quarks. We observe an excess of 20 events above an expected background of 31 events, at a mass of 3.76 GeV/c^2. We observe differences between the signal events and the background. The mass resolution, mass, and decay mode are consistent with a *ccu* baryon. The mass and production are higher than theoretical predictions for the ground state Ξ_{cc}^{++}. If the signal is real and not a doubly-charmed baryon, then it is not accounted for by current physics.

Acknowledgments

I am grateful to my parents and siblings, for their support and care over the years.

I am grateful to Prof. James Russ for his patience, guidance, and wisdom. When I would lose direction, he would nudge me back on track. He is the reason I joined the SELEX experiment.

I have learned a lot from the other members of SELEX. It has been interesting to see the experiment from its early building stages through data taking to the post run analysis.

Special thanks to Dr. Peter Cooper, Jurgen Engelfried, Sasha Kushnirenko, Soon Jun, Jianming You, and Bob Braunger, for their help in wading through the analysis software.

Thanks to friends at CMU, Fermilab, and Naperville, for life outside physics.

The SELEX Collaboration

G.P. Thomas
Ball State University, Muncie, IN 47306, U.S.A.

E. Gülmez
Bogazici University, Bebek 80815 Istanbul, Turkey

R. Edelstein, S.Y. Jun, A.I. Kulyavtsev[1], A. Kushnirenko, D. Mao[2], P. Mathew[3], M. Mattson, M. Procario[4], J. Russ, J. You[1]
Carnegie-Mellon University, Pittsburgh, PA 15213, U.S.A.

A.M.F. Endler
Centro Brasileiro de Pesquisas Físicas, Rio de Janeiro, Brazil

P.S. Cooper, J. Kilmer, S. Kwan, J. Lach, E. Ramberg, D. Skow, L. Stutte
Fermilab, Batavia, IL 60510, U.S.A.

V.P. Kubarovsky, V.F. Kurshetsov, A.P. Kozhevnikov, L.G. Landsberg, V.V. Molchanov, S.B. Nurushev, S.V. Petrenko, A.N. Vasiliev, D.V. Vavilov, V.A. Victorov
Institute for High Energy Physics, Protvino, Russia

Li Yunshan, Mao Chensheng, Zhao Wenheng, He Kangling, Zheng Shuchen, Mao Zhenlin
Institute of High Energy Physics, Beijing, P.R. China

M.Y. Balatz[5], G.V. Davidenko, A.G. Dolgolenko, G.B. Dzyubenko, A.V. Evdokimov, M.A. Kubantsev, I. Larin, V. Matveev, A.P. Nilov, V.A. Prutskoi, A.I. Sitnikov, V.S. Verebryusov, V.E. Vishnyakov
Institute of Theoretical and Experimental Physics, Moscow, Russia

U. Dersch[6], I. Eschrich[7], I. Konorov[8], H. Krüger[9], J. Simon[10], K. Vorwalter[11]
Max-Planck-Institut für Kernphysik, 69117 Heidelberg, Germany

I.S. Filimonov[5], E.M. Leikin, A.V. Nemitkin, V.I. Rud
Moscow State University, Moscow, Russia

A.G. Atamantchouk[5], G. Alkhazov, N.F. Bondar, V.L. Golovtsov, V.T. Kim, L.M. Kochenda, A.G. Krivshich, N.P. Kuropatkin[1], V.P. Maleev, P.V. Neoustroev, B.V. Razmyslovich, V. Stepanov, M. Svoiski, N.K. Terentyev[12], L.N. Uvarov, A.A. Vorobyov
Petersburg Nuclear Physics Institute, St. Petersburg, Russia

I. Giller, M.A. Moinester, A. Ocherashvili[13], V. Steiner
Tel Aviv University, 69978 Ramat Aviv, Israel

J. Engelfried[1], A. Morelos
Universidad Autónoma de San Luis Potosí, San Luis Potosí, Mexico

M. Luksys
Universidade Federal da Paraíba, Paraíba, Brazil

V.J. Smith
University of Bristol, Bristol BS8 1TL, United Kingdom

M. Kaya, E. McCliment, K.D. Nelson[14], C. Newsom, Y. Onel, E. Ozel, S. Ozkorucuklu, P. Pogodin
University of Iowa, Iowa City, IA 52242, U.S.A.

L.J. Dauwe
University of Michigan-Flint, Flint, MI 48502, U.S.A.

M. Gaspero, M. Iori
University of Rome "La Sapienza" and INFN, Rome, Italy

L. Emediato, C.O. Escobar[15], F.G. Garcia[1], P. Gouffon, T. Lungov[16], M. Srivastava, R. Zukanovich-Funchal
University of São Paulo, São Paulo, Brazil

A. Lamberto, A. Penzo, G.F. Rappazzo, P. Schiavon
University of Trieste and INFN, Trieste, Italy

[1]Now at Fermilab, Batavia, IL 60510, U.S.A.
[2]Present address: Lucent Technologies, Naperville, IL
[3]Present address: SPSS Inc., Chicago, IL
[4]Present address: DOE, Germantown, MD
[5]deceased
[6]Present address: Infinion, München, Germany
[7]Now at Imperial College, London SW7 2BZ, U.K.
[8]Now at Physik-Department, Technische Universität München, 85748 Garching, Germany
[9]Present address: The Boston Consulting Group, München, Germany
[10]Present address: Siemens Medizintechnik, Erlangen, Germany
[11]Present address: Deutsche Bank AG, Eschborn, Germany
[12]Now at Carnegie-Mellon University, Pittsburgh, PA 15213, U.S.A.
[13]Present address: Imadent Ltd., Rehovot 76702, Israel
[14]Now at University of Alabama at Birmingham, Birmingham, AL 35294
[15]Now at Instituto de Física da Universidade Estadual de Campinas, UNICAMP, SP, Brazil
[16]Now at Instituto de Física Teórica da Universidade Estadual Paulista, São Paulo, Brazil

Contents

List of Figures

List of Tables

Chapter 1

Search for a new baryon

This thesis details the work done while searching for a previously unseen particle, a baryon with two charm quarks.

The rest of this chapter wil give some of the theoretical background behind this search.

Chapter 2 will give information about the SELEX detector, which was used to collect the data used for this work.

The next chapter will be the analysis done to generate the data sample, followed by the results. Chapter 5 is a short interpretation of the results.

At the end are appendices for work done for the analysis software. Although that work is not directly tied to this analysis, that information is being documented since a considerable amount of the author's efforts was spent developing software that was part of the foundation of all analysis done by SELEX.

1.1 Simplified History

A scientific theory should account for the results of past experiments, predict the outcome of current experiments, and have implications for future experiments. An example is the Mendeleev Periodic Table from chemistry. When it was created in 1869, chemists were trying to find a framework for organizing the elements. The Periodic Table had the virtue that it organized elements into groups by common chemical properties. Based on the Table, Mendeleev left spaces in his table for previously unseen elements. He made predictions of mass and chemical properties based on the elements in the same group.

By 1886, not only were scandium, gallium, and germanium discovered, but there was spectacular agreement between prediction and experiment.

Elements are also composed of smaller units called atoms. In 1913, Niels Bohr presented a model of the atom that included the latest atomic and quantum theory. It provided an explanation for Mendeleev's table, and allowed physicists to calculate, in great detail, spectroscopic results obtained by experiments. Rather than memorizing the properties of dozens of atoms, scientists could concentrate on protons and electrons. (The discovery of the neutron by James Chadwick in 1932 would allow an explanation for isotopes of the same element.) Atomic theory had simplified the situation by presenting a model that could construct an atom from the right number of protons and electrons, and make calculations of that atom that could be verified by experiment.

The world of the subatomic became increasingly more complicated. In 1928, Paul Dirac gave a quantum theory that incorporated Einstein's special relativity. It predicted electron spin and the existence of antimatter, both which were later experimentally verified. Paul Anderson found the positron (antielectron) in 1932, and the muon in 1937. Powell, Lattes and Occhiolini discovered the pion in 1947. Between cosmic ray experiments and the accelerators of the 1950's, physicists discovered the particles which are now known as kaons, lambdas, cascades, and rhos.

Particle physics deals with the framework to organize the many subatomic particles. Much like the Periodic Table for chemistry, particles are organized for similar properties. The framework predicts previously unseen particles. This thesis is a search for one of those particles.

1.2 Standard Model

The current picture of particle physics is given by the Standard Model.. Forces between the fundamental particles are mediated by photons (electromagnetic force), W^+- and Z^0 bosons (weak), and eight coloured gluons (strong). (Gravity, the fourth force, is ignored at this scale.) Matter is organized into leptons and hadrons. Leptons, like the electron, appear to be pointlike, and do not feel the strong force. Hadrons, like the proton, have a substructure, and are coupled to the strong force.

In 1961, Gell-Mann and Ne'eman proposed mathematics to describe the zoo of hadrons. The SU(2) group is an internal symmetry where the strong

force acts equally between protons and neutrons. This symmetry was extended to include "strangeness". The SU(3) math predicted a new particle Ω^-, which was discovered in Brookhaven in 1964. Also in 1964, Gell-Mann and Zweig formed the quark model to explain why only certain representations of SU(3) were found. Quarks (a word abstracted from the novel Finnegan's Wake by James Joyce) are the (pointlike) particles that make up hadrons. Hadrons are divided into mesons, which are made of quark-antiquark pairs, and baryons, made of three quarks. With the three "flavours" of quarks (up, down, and strange) and the SU(3) mathematics, the particle physics situation was greatly simplified. Except for the proton, free hadrons will decay to other, lighter particles. With a knowledge of which properties are conserved (electrical charge, baryon number, etc.) and the forces involved, the quark content of a particle can be assigned based on the (known) values of the decay particles.

There are currently six flavours of quarks: up, down, strange, charm, bottom (or beauty), and top. If the SU(6) symmetry was perfect, all hadrons would have the same mass. Different hadron masses mean that the symmetry is broken, presumably due to different quark masses. With assumptions about how the symmetry fails, relationships can still be made for the hadrons. Mass predictions, like ($m_K^2 = \frac{1}{4}(3m_\eta^2 + m_\pi^2)$), are remarkably accurate compared to experiment.

1.3 Quantum Chromodynamics

The theory that describes the strong force from gluons is called Quantum Chromodynamics, or QCD for short. A full description would require a textbook[1]. The important points for this discussion are:

- Quarks have a charge called colour, which have been labeled green, blue, and red. Antiquarks come in three anti-colors. Color was motivated by a desire to account for particles like the Δ^{++}, which is formed from three identical quarks. The particle is a fermion, which means that its wave function should be totally antisymmetric. The spin, space, and flavor functions are symmetric, so the property of color allows the wave function to be antisymmetric. Another piece of evidence comes from the decay of π^0 into two photons. The decay rate formula depends on the square of the number of colours. With three different colours, theory matches experiment to within a few per cent. With only one

colour, the formula is off by a factor of 9.

- Observed particles must form a color singlet. That can be done by having three quarks, one of each color, or from a quark antiquark pair (ex. $r\overline{r}$). Particles with two matter quarks would be a colour triplet object, none of which have been observed.

- Lepton-nucleon scattering shows that, at high momentum transfer (small wavelengths), the quarks in a hadron behave as if they are free. This phenomenon is known as asymptotic freedom. The 4-momentum transfer squared is labeled q^2. The strong coupling constant α_s decreases as q^2 increases.

- The strong coupling constant α_s increases as q^2 decreases. As q approaches a value, known as Λ_{QCD}, α_s is of order 1 and perturbative QCD theory becomes unreliable. Λ_{QCD} is in the range of 100 to 500 MeV. The binding energy for forming hadrons from quarks and gluons should be on the scale of a few times Λ_{QCD}.

- Single quarks, a colour triplet object, have not been found. This is known as confinement. At large distances, the strong force increases linearly. The work necessary to pull a quark free from a hadron will be much larger than needed to create quark-antiquark pairs.

1.4 Baryon multiplet

The quark flavours, in order of increasing mass, are up, down, strange, charm, bottom (or beauty), and top. The first three quarks (up to strange) are referred to as light quarks, since their masses are lighter than the QCD binding energy. Charm, bottom, and top are heavy quarks, since their masses are above Λ_{QCD}. There are many particles with a specific combination of quark flavours, excited states with different spin and angular momentum configurations. For now, we are concerned with the first four quarks, up to charm. Figure 1.1 shows the expected ground state (lowest mass) baryons. Moving "up" in the multiplet increases the charm content of the baryon.

The important feature for this thesis is that all baryons with zero or one charm quark listed in the figure have been found. No baryons with two or three charm quarks have been found. The QCD framework is successful enough that it would be surprising if doubly charmed baryons were never found. Those particles are heavy enough that they are expected to be hard to produce. Experiments up to the present were assumed to not have enough statistics to find a signal.

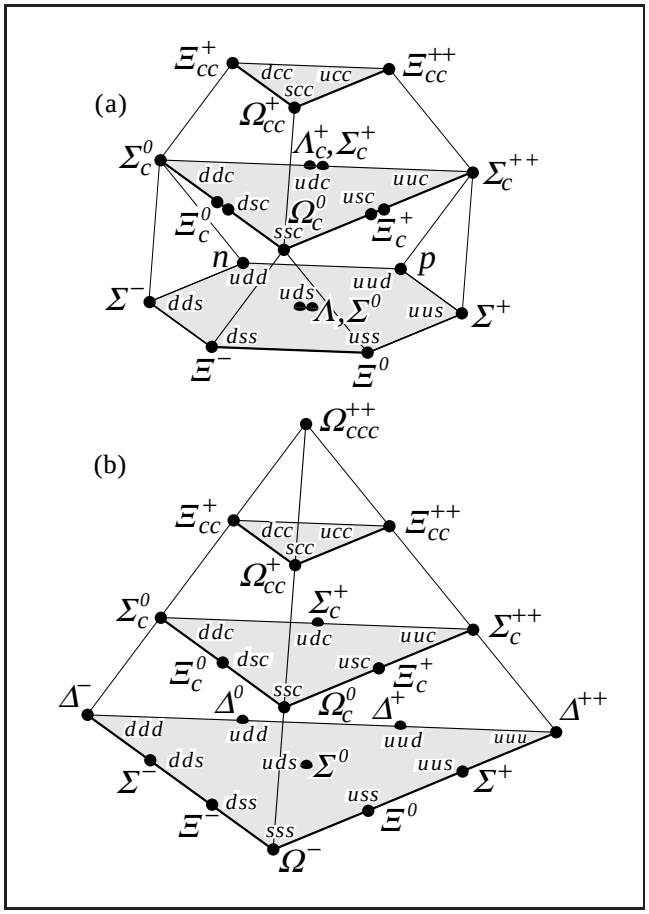

Figure 1.1: SU(4) multiplets of baryons made of u, d, s, and c quarks. (a) The 20-plet with an SU(3) octet. (b) The 20-plet with an SU(3) decuplet. All baryons in a multiplet have the same spin and parity.[2].

1.5 Predictions for Ξ_{cc}^{++}

Doubly charmed baryons have not been seen experimentally. In the absence of data, theorists have made predictions to guide the experimentalist. Information about heavy quarks has to be extrapolated from baryons with one heavy quark, and mesons. (Mesons with two heavy quarks, like charm-anticharm and bottom-anticharm, have been observed.) Most predictions of the properties of doubly charmed baryons are based on Heavy Quark Effective Theory (HQET), specifically the article by Savage and Wise[3]. With m_Q being the mass of the heavy quark, HQET allows a systematic $1/m_Q$ expansion for the properties of the doubly heavy baryons, in terms of the corresponding properties in heavy mesons. That paper relates doubly heavy antibaryons with mesons having only one heavy quark, but the predictions should apply for matter baryons as well. The key points are the following:

- The two heavy antiquarks will form a small weakly bound color triplet system. The binding is due to the strong force, and will be modeled by a two-body Coulomb interaction.

- The size of the ground "state" of the two heavy antiquarks will be of order $1/\alpha_s(m_Q)m_Q$, which will be small compared to the strong interaction scale $(1/\Lambda_{QCD})$.

- The two heavy antiquarks system can be treated as a point object, acting like an extra heavy (matter) quark. This $(\bar{Q}\bar{Q})\bar{q}$ baryon can then be related to $Q\bar{q}$ mesons.

SELEX members have given overviews for how to search for doubly charmed baryons.[4, 5] For this analysis, the four properties of interest are decay modes, mass, lifetime, and production cross section. These will show which mass reconstructions to use, where to look on the mass plots, the effectiveness of cuts based on vertex separation, and how much of signal might be seen in the absence of background. Table 1.1 shows the properties of some of the more important particles involved in this search. A complete listing of properties of all known hadrons are available from the Particle Data Group [2].

Mesons				
Particle	quarks	mass in GeV/c^2	τ in seconds	$\gamma c\tau$ for $\gamma = 100$
π^+, π^-	$u\overline{d}, d\overline{u}$	0.140	2.6×10^{-8}	780 m
K^+, K^-	$u\overline{s}, s\overline{u}$	0.494	1.3×10^{-8}	390 m
$D^+ \to K^-\pi^+\pi^+$	$c\overline{d}$	1.869	1.06×10^{-12}	3.2 cm
$D^0 \to K^-\pi^+(\pi^-\pi^+)$	$c\overline{u}$	1.865	0.42×10^{-12}	1.3 cm
$D_s^+ \to K^+K^-\pi^+$	$c\overline{s}$	1.969	0.47×10^{-12}	1.4 cm
Baryons				
Particle	quarks	mass in GeV/c^2	τ in seconds	$\gamma c\tau$ for $\gamma = 100$
p^+	uud	0.938	∞	∞
Σ^-	sdd	1.189	0.80×10^{-10}	2.4 m
$\Lambda_c^+ \to p^+K^-\pi^+$	cud	2.285	0.21×10^{-12}	0.6 cm
$\Xi_c^+ \to p^+K^-\pi^+$	cus	2.466	0.35×10^{-12}	1.1 cm
Ω_c^0	css	2.7	0.06×10^{-12}	0.2 cm

Table 1.1: Guide for the properties of some of the more important particles for SELEX. γ is the relativistic Lorentz boost. A factor of 100 was used to give a scale for the distances the particles will travel (before decaying) in the SELEX data.

1.5.1 Decay modes

To simplify the systematics, the decay modes of interest involve charged particles produced before the SELEX tracking detectors, and with a long enough lifetime to make it through all of the detectors without decaying to other particles. This will allow high precision measurement for position and momentum, which will be needed to minimize the width of a mass peak. For the SELEX experiment, protons and charged pions and kaons are considered "stable". Most decay modes will involve those particles. Strange baryons will not be used, as they are likely to decay part of the way through the detector, which can cause tracking mistakes.

The charm quark is assumed to (weakly) decay to a strange quark and a W^+. Semi-leptonic decays have the problem of missing neutrino momentum, which complicates main reconstruction. We will only consider W^+ decaying to a π^+ or multiple charged mesons. The decay of charm to a down quark is Cabbibo suppressed and will be ignored in our search.

The decay mode to be examined will be $\Xi_{cc}^{++} \rightarrow \Lambda_c^+ K^- \pi^+ \pi^+$, with $\Lambda_c^+ \rightarrow p^+ K^- \pi^+$. This decay is illustrated in figure 1.2. Bjorken stated that more than 50% of the final states could be expected to go through Λ_c or Ξ_c channels [6]. By requiring a clean Λ_c^+ sample, the background should be greatly reduced. A possibility is that the decay passes through certain resonances, specifically $\Xi_{cc}^{++} \rightarrow \Sigma_c^{++} K^{0*}$, with $\Sigma_c^{++} \rightarrow \Lambda_c^+ \pi^+$ and $K^{0*} \rightarrow K^- \pi^+$.

The modes $\Xi_{cc}^{++} \rightarrow \Xi_c^+ \pi^+$ and $\Xi_{cc}^{++} \rightarrow \Xi_c^+ \pi^+ \pi^+ \pi^-$ can also be looked at. Unfortunately, the only sample of Ξ_c^+ that does not involve strange baryons in the decay, is the Cabbibo suppressed $\Xi_c^+ \rightarrow p^+ K^- \pi^+$, which has an order of magnitude less events than the Λ_c^+ sample.

1.5.2 Mass

The simplest possible mass prediction is to get the mass difference when replacing a strange or down quark with a charm quark, then adding that mass to the single charmed baryon. That gives two extrapolations,

$ccu = csu + (csu - ssu) = 2(\Xi_c^+) - \Xi^0 = 2(2466)$ - 1315 = 3617 MeV

$ccu = cdu + (cdu - ddu) = 2(\Lambda_c^+) - n = 2(2285)$ - 940 = 3630 MeV

This is a gross oversimplification, but it does give a rough estimate.

Bjorken makes his mass prediction starting with the Ω_{ccc}, which should be related to the J/ψ by

$$m(QQQ)/m(Q\bar{Q}) \cong 3/2 + \text{constant}/m^{4/3} + \text{constant}/ln^2(m/m_0)$$

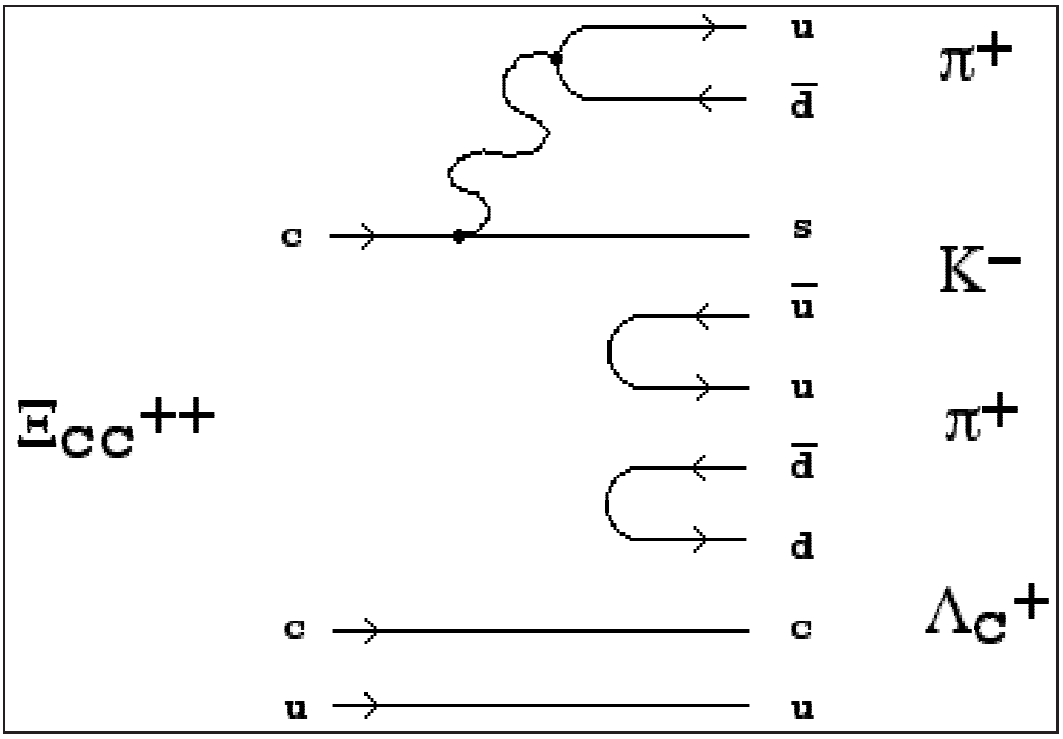

Figure 1.2: Decay mode of $\Xi_{cc}^{++} \to \Lambda_c^+ K^- \pi^+ \pi^+$.

The correction terms are binding contributions from a linear plus coulomb two-body potential. With observed particles

$$\Delta/\rho = 1.60, \qquad \Delta/\omega = 1.58, \qquad \Omega/\phi = 1.64$$

he makes the estimate that

$$ccc/\psi = 1.59 \pm .03 \qquad bbb/\Upsilon = 1.56 \pm .02$$

He assumes the validity of the "equal-spacing" rule for the masses of all J = 3/2 baryons to interpolate the other baryons. He then used a hyperfine splitting analysis by DeRujula, et al. [7] and quoted their results, relative to to the J = 3/2 baryons. The value for the ccu baryon mass is 3635 MeV. While this analysis has the right mass for the Ξ_c and Ω_c baryons, it was 40-50 MeV low for the Λ_c and Σ_c.

Itoh et al used an eight parameter computer formula to obtain predictions for the 30 particles, including the *ccu* baryon mass at 3649 MeV [8]. A quenched lattice QCD calculation gave a mass around 3.60 GeV. [9]

Ebert et al [10] calculated the mass spectra of doubly heavy baryons using relativistic quark model. The light quark is treated completely relativistically, while an expansion using the inverse mass is used for the heavy quarks. They used HQET to simplify the calculations to a two body system (a light quark, and a heavy diquark).

Some of the mass predictions found in the literature are listed in Table 1.2. The important point is that the uncertainties given for each prediction are smaller that the variation between the predictions. Also, even with similar methods, there are variations due to the choice of parameters, like the quark masses, binding energy, relativistic approximations, and so on.

1.5.3 Lifetime

For HQET, as the mass of the heavy quark becomes infinitely large (compared to the light quarks), the heavy quark decay is unaffected by the light quarks. This is the spectator decay model. All hadrons with the same heavy quark should have the same lifetime, corrected for phase space differences.

Calculations from HQET have been applied for the singly-charmed hadrons. For the charm mesons, the D^+, D^0 and D_s^+ have equal semileptonic decay rates. Since the charm quark is not infinitely heavy, there are corrections in the hadronic decay modes. Pauli interference between similar quarks in the

Reference	mass Ξ_{cc}	mass Ξ^*_{cc}
Bjorken [6]	3.64	3.70
Itoh et al [8]	3.65	3.73
Lewis et al [9]	3.60	3.68
Ebert et al (2002) [10]	3.62	3.727
Kiselev and Likhoded [11]	3.48	3.61
Tong et al [12]	3.74	3.86
Roncaglia et al [13]	3.66	3.81
Ebert et al (1997) [14]	3.66	3.74
Körner et al [15]	3.61	3.68
Kaur [16]	3.71	3.79

Table 1.2: Predicted Ξ_{cc} masses in GeV/c^2. The first four are mentioned in this text, the rest were discussed by Kiselev and Likhoded[11].

D^+ decay is the largest contribution for the difference in the D^+ and D^0 lifetimes. For the differences between the D_s and the D^0, the size and sign of the W-annihilation term are too complex to be currently calculated. The charm baryons are more complex, in particular the $O(1/m_c^3)$ terms. For instance, W annihilation/scattering terms are not helicity suppressed as they are for the mesons. Experimental results show there is about a factor of 15 difference for the lifetimes of the D^+ and the Ω_c^0. A more thorough description for singly charmed hadron lifetimes is available in the thesis by Kushnirenko [17].

The simplest estimate would be to take half the Λ_c^+ lifetime, since there are two charm quarks in the baryon that can decay. The light quark is assumed not to interfere with the decay of the charm quark. That would give $\tau = .10$ picoseconds. Starting with the spectator decay model for the doubly charmed baryon lifetime, Kiselev et al. [18] compare the lifetime to the D^+. This gives $\tau(\Xi_{cc}) \sim 1/2\tau(D^+) = .53$ ps. Further corrections to the calculations led them to the result $\tau = 0.43$ ps.

1.5.4 Cross section

The charm production cross section is roughly 25 μb, while the inelastic scattering cross section is roughly 25 mb. We might expect the production of doubly charmed baryons to be suppressed by a factor of 10^{-3} compared

to singly charmed baryons.[5]

$\sigma(c\bar{c}c\bar{c})/\sigma(c\bar{c}) \approx \sigma(c\bar{c})/\sigma(in.) \sim 10^{-3}$

This does not account for how likely two charm quarks will form a diquark, and also does not address hadronization, how the quarks form the hadrons.

Aoki et al.[19] reported a low statistics measurement of double to single open charm pair production, for $D\bar{D}D\bar{D}$ to $D\bar{D}$ for central and diffractive events, of 10^{-2}. NA3[20] found a ratio of $\sigma(\psi\psi)/\sigma(\psi) \approx 3 \times 10^{-4}$. Kiselev et al.[11] used leading order perturbative QCD to calculate the cross section from gluon-gluon and quark-antiquark production. They estimate cc-diquark production to total charm production to be $\sigma_{cc}/\sigma_{charm} \sim 10^{-4} - 10^{-3}$ for collider experiments and $\sim 10^{-6} - 10^{-5}$ for fixed target experiments. Günter and Saleev[21] consider non-perturbative hadronic interactions at high energies and large transverse momenta. The model is that charm quarks present in colliding protons, due to intrinsic charm, could result in the doubly charmed baryon production cross section being twice as high as predictions based on leading QCD alone.

1.5.5 Comments on current theory

During this overview, I had problems with two issues. This may be because I am not as experienced with the topics as the authors of the papers, I feel they still need to be addressed.

The first involves the HQET predictions for doubly charmed baryons. In the introductions for the predictions, most papers restate the HQET predictions, especially that the heavy quarks form a diquark of small size. Some mention that this is a prediction, others make it sound like an established fact. For comparison, the quark-quark attractive force should be half that of the quark-antiquark force. The QCD potential suggests that the ψ and $\psi\prime$ mesons are roughly 0.4 and 0.8 fm in size. For scale, the charge radius of a proton, a baryon with only light quarks, is $R_{rms} = 0.80$ fm.

HQET is the best guide for this class of particles, in the absence of experimental data to help the theorists. It is still a model, not a calculation from first principles. The mass predictions based on HQET have a range of values. The lifetime results for D^+ and D^0 raise the question of applicability of HQET for charm decays. The Pauli interference term, of order $O(1/m_c^3)$, is as big as the first term in the expansion. The convergence of the series for charm hadrons and the influence of higher order terms is unknown.

At the end of the Savage and Wise paper [3], they state clearly

> The results of this paper are primarily of pedagogical value. For charm and bottom quarks the size of the $c\bar{c}$ and $b\bar{b}$ bound systems are not very much less than $1/\Lambda_{QCD}$... However, this work does provide a starting point...

The second issue involves the possibility of success in the search. Going into this search, the chance of finding a reasonable signal seemed unlikely, but Berezhnoi et al [22] state, in their abstract: "In the E781 experiment the observation of Ξ_{cc} and Ξ^*_{cc} is practically unpossible." I feel compelled to respond to this. My impression is that their statement is based on their production cross section estimate $\sigma_{(cc)}/\sigma_{charm} \sim 10^{-6} - 10^{-5}$, and that the SELEX goal was to have on the order of 10^5 fully reconstructed charm hadrons.

First, their estimate might be overly pessimistic. Other models have a higher ratio, so while there is uncertainty about the cross section, a search is reasonable. Second, their model involved perturbative QCD, which may not be the only production mechanism for SELEX. The SELEX data set is efficient for high x_F events, where other mechanisms, like intrinsic charm, might play a larger role. Third, an observation depends on signal and background. If there are only a handful of reconstructed doubly charmed baryons, it could be seen, as long as it is not buried in random background.

Chapter 2

Experiment

2.1 Background

Experiment 781 is also known as SELEX, short for Segmented Large x_F baryon spectrometer. The experiment was designed to have excellent position and momentum resolution for forward interactions and decays. Data was taken during the 1996-97 Fermilab fixed target program. The collaboration had about 115 physicists from 20 institutions worldwide. The experiment took place in the Proton Center beamline. The detector was placed in PC4 hallway. Figure 2.1 shows the layout of the experiment.

The experiment directs a beam of particles from the accelerator at a stand of materials, the fixed targets. The trigger detector and electronics look for an interaction between the beam and the targets. The spray of particles produced by this primary interaction will travel downstream (in the direction of the particle beam) through the rest of the experiment. The hallway is divided into spectrometers, regions free of magnetic field where (stable) charged particles will travel in a straight line. Magnetic fields between spectrometers will deflect charged particles, providing information about momentum. The position of particles will be determined by a combination of proportional wire chambers (PWC) and silicon detectors. Ring imaging Cherenkov (RICH) detectors and transition radiation detectors will help to decide the type of particle. The rest of the chapter will provide more information about the components of the experiment, starting from the particle beam and moving downstream through the experiment hallway.

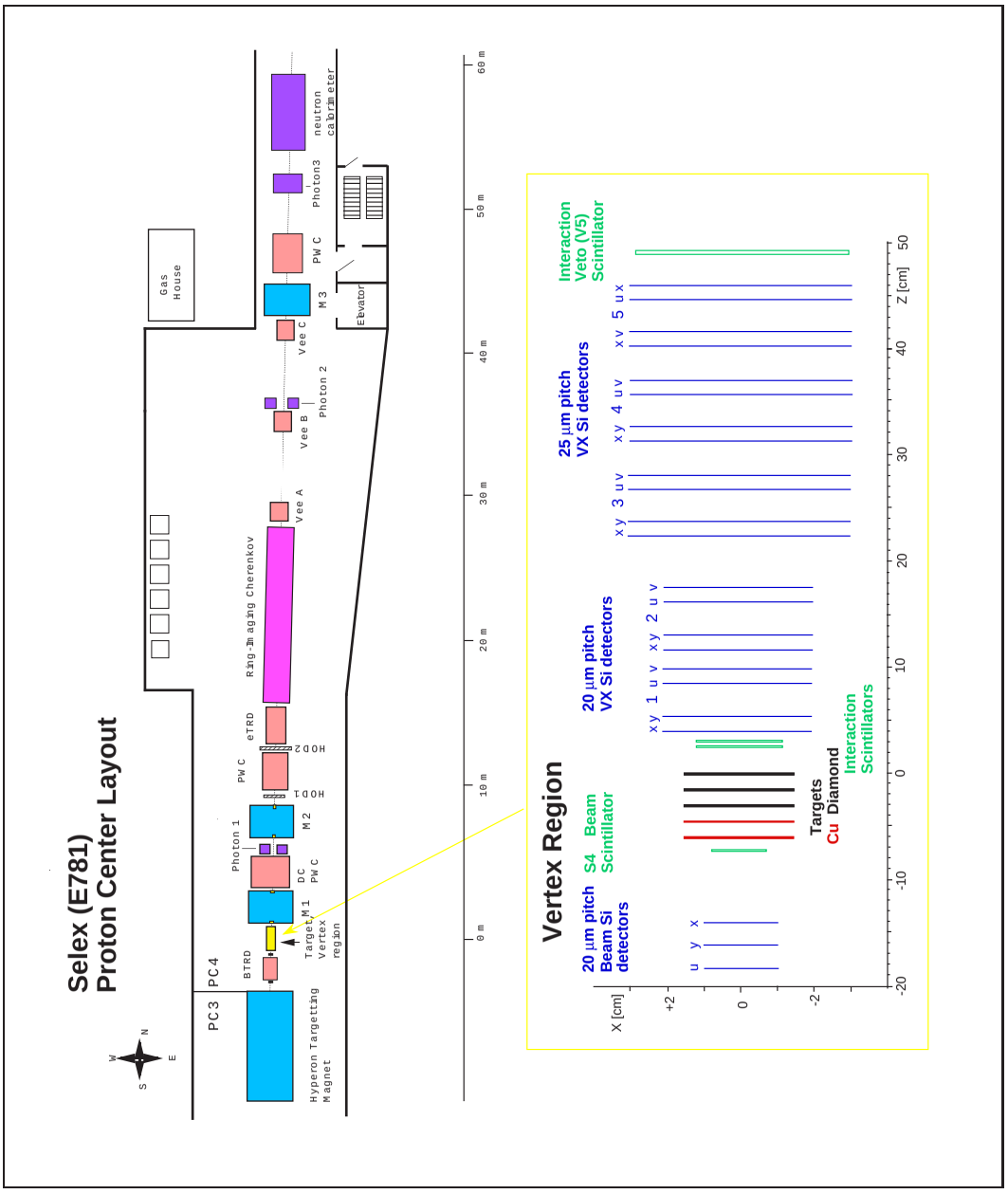

Figure 2.1: Schematic view of SELEX spectrometer and vertex region

2.2 SELEX Coordinate System

The three SELEX coordinate systems are global, local, and detector. The global coordinate system has the z-axis is along the beam direction, the y-axis is vertically up and the x-axis completes a right-handed coordinate system. The origin is in the center of the last charm target, with $z = 0$ at the downstream surface.

The SELEX system is divided into spectrometers, regions free of magnetic field where stable particles should travel in straight lines. The local coordinate system for a spectrometer starts and ends at analysis magnets, where charged particles are deflected by the magnetic fields (figure 2.2). For instance, the M1 coordinate system has $z = 0$ at the center of the M1 magnet, and ends at the center of the M2 magnet (where the M2 coordinate system starts). There is no analysis magnet between the beam and vertex spectrometers, but they are separated since an interaction between a beam particle and a target will produce very different tracking environments for the two spectrometers. Both use the global coordinates.

The detector coordinate system is specific for each detector plane. x_d is the readout direction. For silicon strips and wire chambers, no information about a track's y_d position is known, other than the fact the particle did not pass outside of the detector. When converting from detector to global (or local) coordinates, x_p planes give information about a track's global x position, and y_p planes yield y information. u_p and v_p projections are normally at $\pm 45^0$ angle with respect to x, y axis.

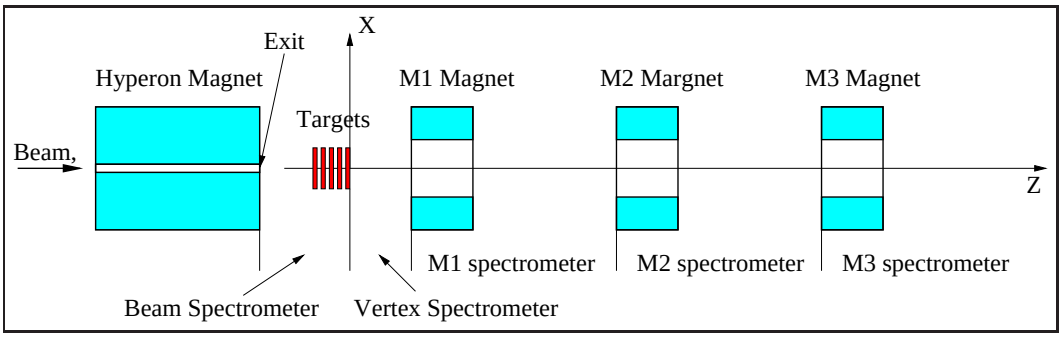

Figure 2.2: Schematic view of SELEX spectrometer (off-scale)

2.3 Hyperon Beam

The Tevatron accelerator produced 800 GeV protons, which were directed to the different fixed target experiment halls. For SELEX, that beam hit a 1 interaction length beryllium target. Forward going secondary particles enter a narrow (about $0.5 \times 0.5\,\mathrm{cm}$) 7.3 m long curved channel inside the 3.5 T hyperon magnet. The tungsten walls of the channel served to collimate the beam position and energy (Figure 2.3). By changing the magnet polarity, field strength, and beam targeting angle, the composition of the secondary beam could be modified. Since the relative fraction of hyperons in the secondary beam grows with the energy[23, 24], charm data taking used a $600 \pm 50\,\mathrm{GeV}$ hyperon beam. At the target region, the 600 GeV negative secondary beam consisted of approximately 50.9% π^-, 46.3% Σ^-, 1.6% K^- and 1.2% Ξ^-. With the opposite magnet polarity, the secondary beam consisted of approximately 89.2% protons, 5.7% π^+, 2.7% Σ^+ and 2.4% K^+ [25].

2.4 Beam Spectrometer

The beam spectrometer consists of everything before (and including) the last charm target. This include the hyperon magnet.

2.4.1 Beam Transition Radiation Detectors

Beam particles were tagged with the 10 Beam Transition Radiation Detectors (TRDs). Each module has a radiator made of 200 polypropylene foils $17\,\mu$m thick followed by 3 proportional wire chambers filled with the mixture of Xe+30% CH_4 gas, to detect transition radiation [27]. A relativistic particle crossing the boundary of media with different dielectric constants emits transition radiation photons. Typically the energy of such photons is a few keV. The probability of radiation of transition radiation photon is proportional to the Lorentz γ-factor. A lighter particles, like pions, would produce more TRD hits than baryons, like sigmas, of the same energy.

The total number of hits in the Beam TRD was used to separate the baryon component from the meson component of the beam (Figure 2.4). Beam TRD information was used in the trigger (Section 2.9) to increase the fraction of Σ^- beam particles in the recorded interactions.

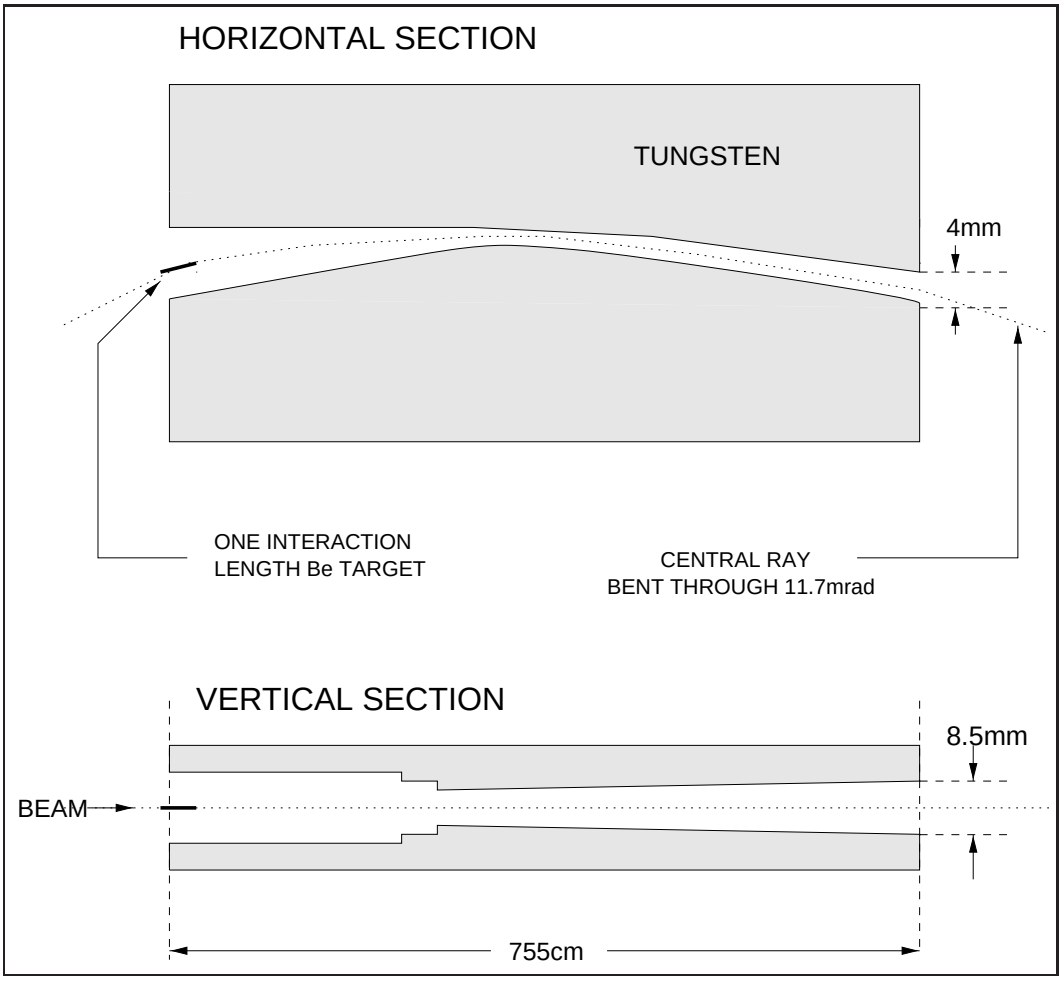

Figure 2.3: Schematic layout of the hyperon beam magnet [26].

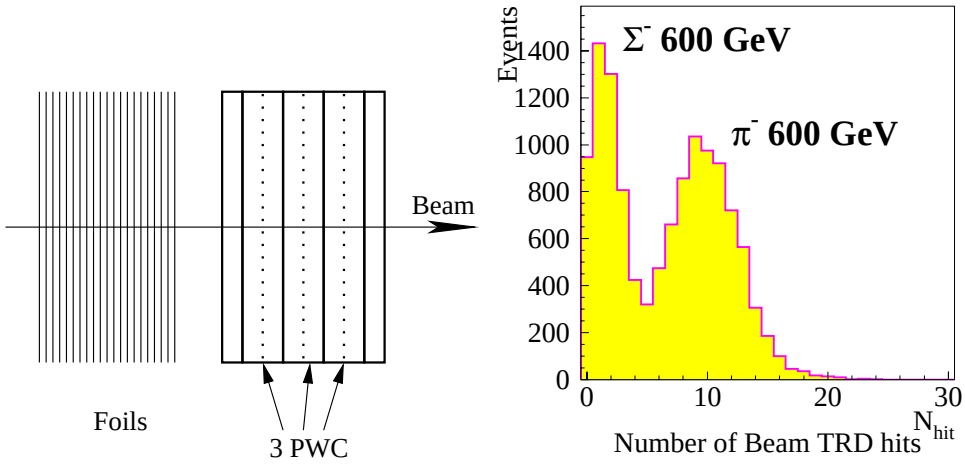

Figure 2.4: Schematic layout of the Beam TRD. Σ^-/π^- separation using the number of hits in the Beam TRD.

2.4.2 Beam Silicon Detectors

Eight beam silicon single sided detectors (SSD) were used to measure beam track position and direction of motion. Each detector has 1024 strips of 20 μm pitch, covering a 2×2 cm area. The strips are read out by SVX chips. Due to the integration gate of the readout electronics being a few microseconds long, information about previous beam tracks from the 1 MHz beam were sometimes stored in the beam SSD hit output along with the triggering beam.

2.4.3 Hardware Scattering Trigger Silicon Detectors

These silicon detectors were designed to improve resolution of pions with the small scattering angles [28], to aid study of Primakoff physics. The four detectors have 50 μm pitch strips and short 80 ns gates, so only hits from the triggering beam particle were read out. Since the beam silicon can have information from multiple beam particles, this system was used in the decision algorithm that decides which beam track caused the trigger.

2.4.4 Targets

The segmented target stack consisted of 5 foils, separated by 1.5 cm. All of the targets represented a combined interaction length of 4.3% for protons.

Target properties are summarized in Table 2.1.

target	material	thickness [mm]	z [cm]	Atomic number A	Density [g/cm^3]	Inter length [%]
1	copper	1.6	-6.13	63.5	8.96	1.06
2	copper	1.1	-4.62	63.5	8.96	0.76
3	diamond	2.2	-3.10	12	3.20	0.82
4	diamond	2.2	-1.61	12	3.20	0.82
5	diamond	2.2	-0.11	12	3.20	0.82

Table 2.1: Charm target properties

2.5 Vertex Spectrometer

The vertex spectrometer starts at the downstream edge of the last target, and ends at the middle of the M1 magnet.

2.5.1 Vertex Silicon Detectors

The vertex silicon detectors were mounted in five stations of four detectors each. Each station had detectors rotated in different angles, to cover the x_p, y_p, u_p and v_p projections (Figure 2.5). The u_p and v_p detectors on the fifth station were only rotated 15 degrees, to improve x projection information, which was used for momentum calculation.

The stations were mounted on a special granite optical bench along with the targets, for support and alignment stability. Each of the detectors has greater than 98% hit detection efficiency and spatial resolution about 6.5 μm (Figure 2.6 [26]).

The first two stations consisted of 5-cm detectors. The silicon plane has 2560 strips of 20 μm pitch, covering an active area of 5.1 $\times$ 5.0 cm^2. Every strip is read out in the 3.1 $\times$ 5.0 cm^2 middle area of the detector, where the hit density is the largest. On the edges every other strip is read out, because of low hit density. Only low energy tracks will reach this outer region, and their resolution will be dominated by multiple scattering.

The next three stations consisted of mosaic detectors. Each mosaic detector was build out of three 8.3 $\times$ 3.2 cm^2 silicon planes. Each plane had

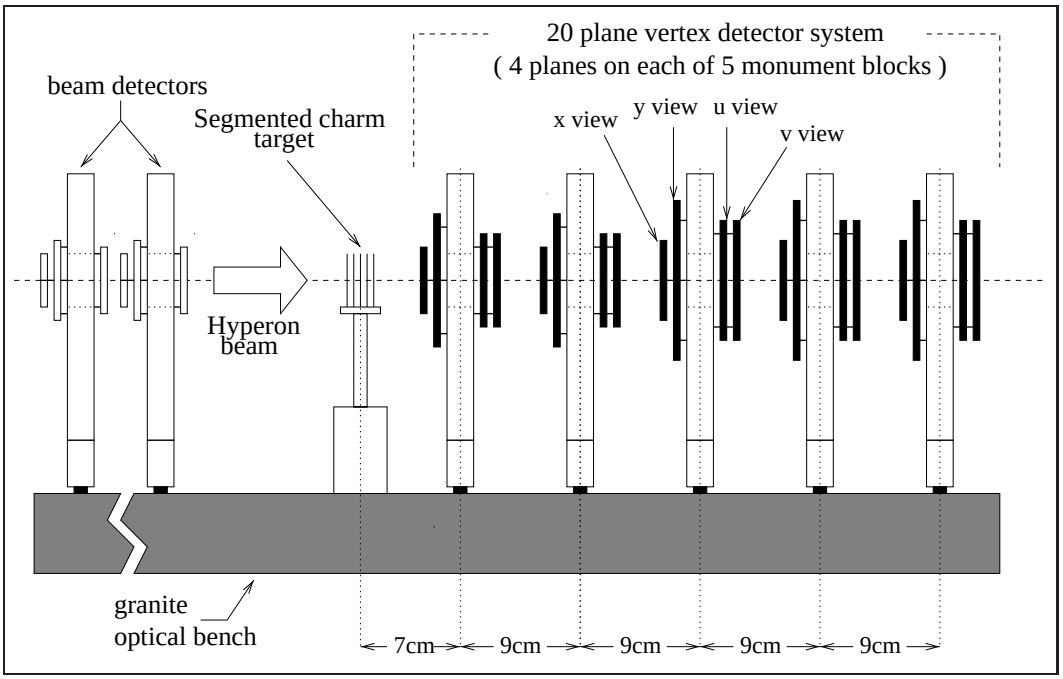

Figure 2.5: Beam and vertex silicon layout [26].

1280 strips of 25 μm pitch. The center panel has every strip read out, and the outer panels have every other strip readout. The outer panels covered tracks angles greater than 80 mradian, which were much fewer tracks than the center panel.

The silicon strips were connected to silicon vertex (SVX) chips that were adapted to fixed target experiments, specifically for SELEX.[29] The chips were controlled by the SVX Readout Sequencer (SRS). For a more in depth investigation of the vertex silicon, including the SVX readout system, consult the thesis by Mathew [26].

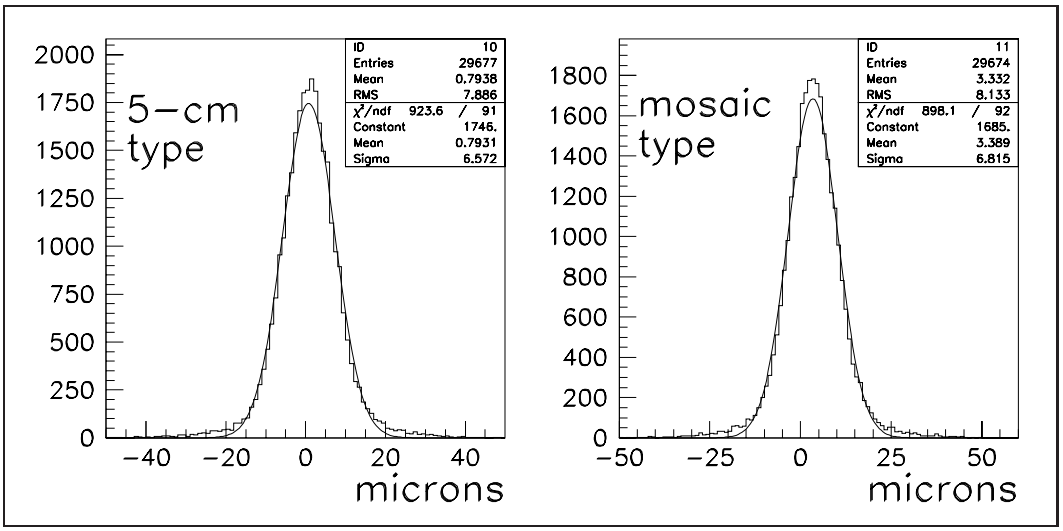

Figure 2.6: Typical resolutions of vertex detectors [26].

2.6 M1 Spectrometer

The M1 spectrometer is bounded by the M1 and M2 magnets. Low momentum particles (< 2.5 GeV) from the primary interaction will be swept aside by the M1 magnet. Tracking is done with large acceptance wire chambers, and silicon detectors for high momentum particles. This spectrometer is necessary to determine momentum for soft tracks produced upstream and for charged tracks made downstream of the vertex silicon by strange particle decays.

2.6.1 M1 Magnet

The center of the M1 magnet lies at a global z position of 190 cm. The aperture size is 61 cm (horizontal) by 51 cm (vertical). The magnetic field in the center is 11.98 kG, and the magnet produces a p_t kick of 0.73 GeV for a 1 GeV charged particle.

2.6.2 M1 Multiwire Proportional Chambers

The M1 spectrometer has 3 wire chambers of 4 sensitive planes. Each chamber covers the x, y, u and v projections (Figure 2.7). Each plane has 3 mm wire spacing and a $2 \times 2\,\mathrm{m}^2$ active area. The M1 PWCs have greater than 90% hit detection efficiency with 0.9 mm spatial resolution.

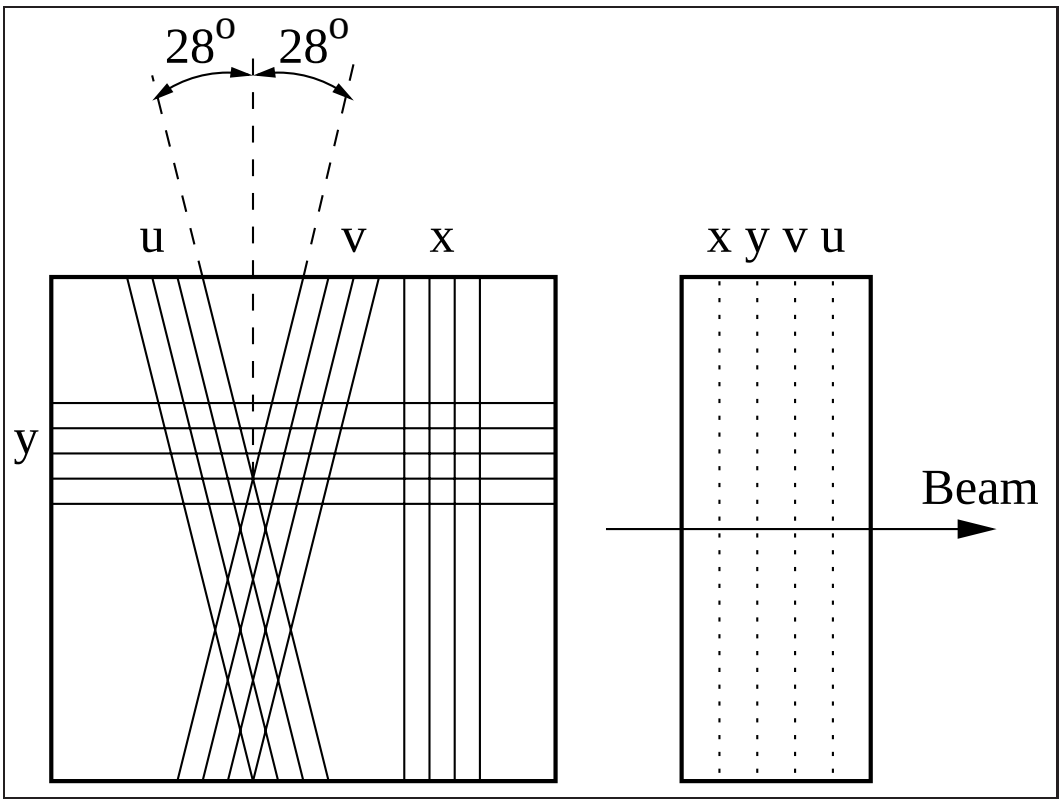

Figure 2.7: Schematic layout of M1 PWC chamber.

2.6.3 Large Area Silicon Detectors

There are three stations of Large Area Silicon Detectors located at the end plates of the M1 and M2 magnets (figure 2.8). These detectors are designed to improve position resolution of high momentum tracks.

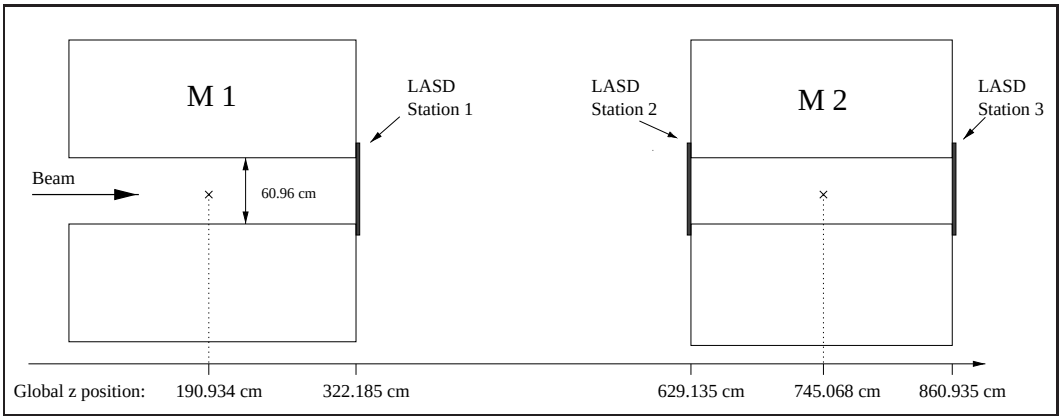

Figure 2.8: Location of the three LASD stations [30].

The two stations in the M1 spectrometer are called LASD1 and LASD2. Each station had 2 detectors of double-sided silicon detectors (DSD) with $50\,\mu$m strip pitch and $3.2 \times 2.6\text{cm}^2$ sensitive area. The other two detectors in a station were single-sided (SSD) with $50\,\mu$m strip pitch and $3.2 \times 3.2\text{cm}^2$ sensitive area. Each DSD was treated as two planes, measuring hits in x and y projections. The SSD planes covered the u and v projections. Detectors have 95-99% hit detection efficiency and the spatial resolution about $15\,\mu$m. Figure 2.9 shows the station layout and the resolution.[31], [30].

2.7 M2 Spectrometer

2.7.1 M2 Magnet

The center of the M2 magnet lies at a global z position of 745 cm. The aperture size is 61 cm (horizontal) by 25 cm (vertical). The magnetic field in the center is 14.66 kG, and the magnet produces a p_t kick of 0.84 GeV for a 1 GeV charged particle. Charged particles from the primary interaction will be swept aside if they are below 15 GeV.

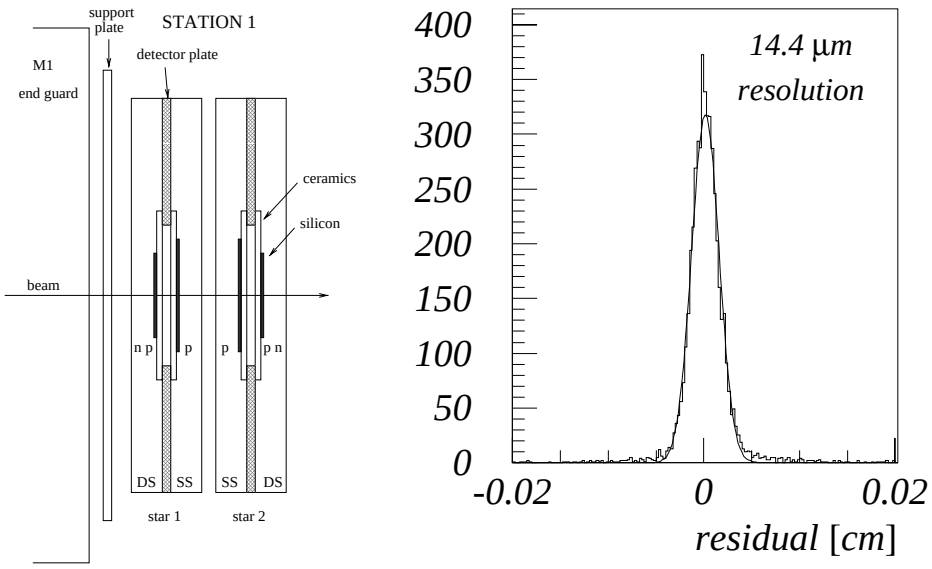

Figure 2.9: Layout and resolution of LASD. First figure shows schematic side-view of the LASD station with a sequence of a double sided, two single sided and another double sided detector. Second plot shows the resolution of the single sided detector [31]

2.7.2 M2 Multiwire Proportional Chambers

The M2 PWC system consists of 7 chambers with 2 mm wire spacing. The 3 upstream chambers have a $60 \times 60\,\mathrm{cm}^2$ aperture. The 4 downstream chambers have a $60 \times 100\,\mathrm{cm}^2$ aperture (Figure 2.10). Each chamber has 2 sensitive planes in 2 orthogonal projections. Five chambers cover the x and y projections, the other two chambers covering u and v. The chambers have greater than 95% hit detection efficiency with 0.6 mm spatial resolution [32].

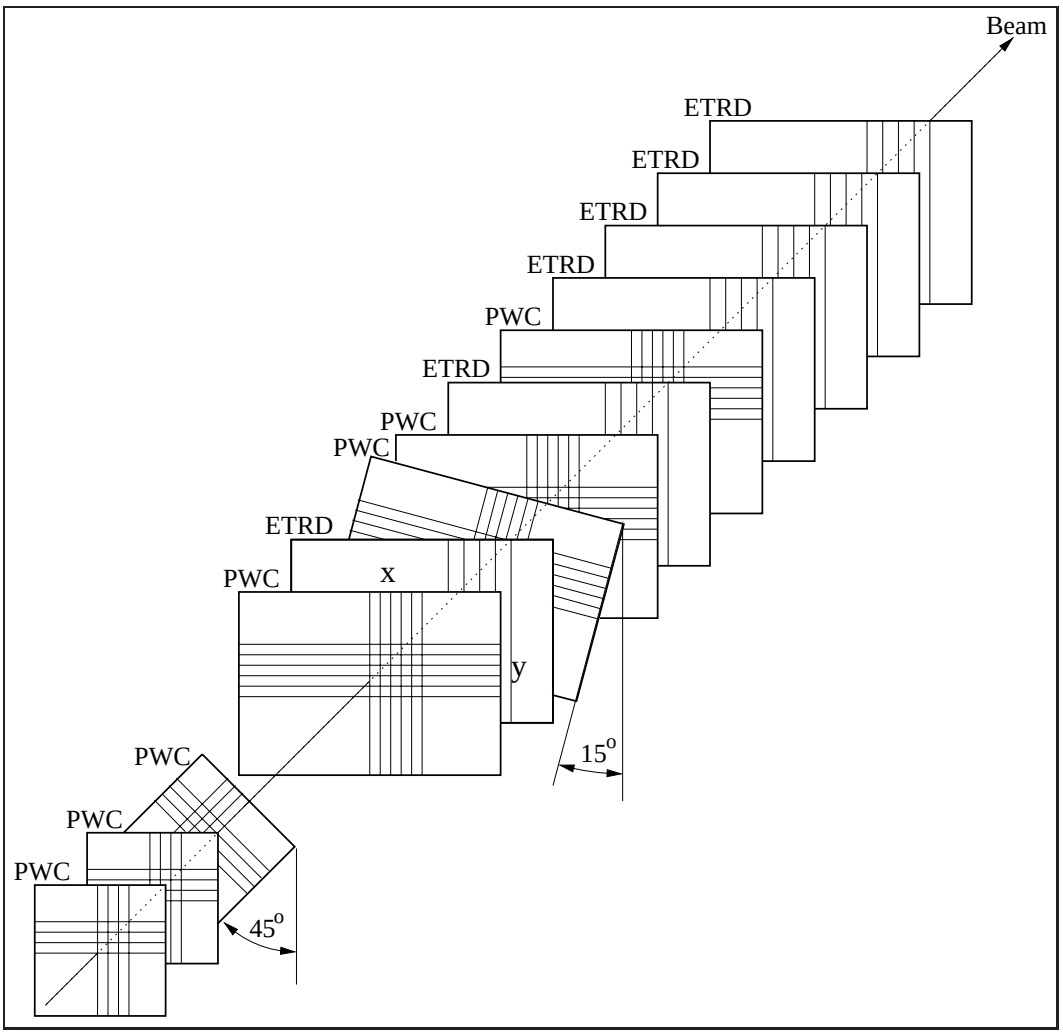

Figure 2.10: Schematic layout of M2 PWC chamber.

2.7.3 LASD

LASD3 is mounted on the downstream end plate of the M2 magnet. The station is similar to the M1 LASD stations.

2.7.4 Ring Imaging Cherenkov Counter

The RICH detector was the primary source of particle identification for the SELEX experiment. Particles passed through a 10 m long vessel filled with Ne gas. Since the relativistic particles are traveling faster than the speed of light for that medium, cherenkov is emitted. The light was reflected on the spherical mirrors with 20 m curvature, and focused on a 2848 phototube array, forming rings on its surface. (Figure 2.11)

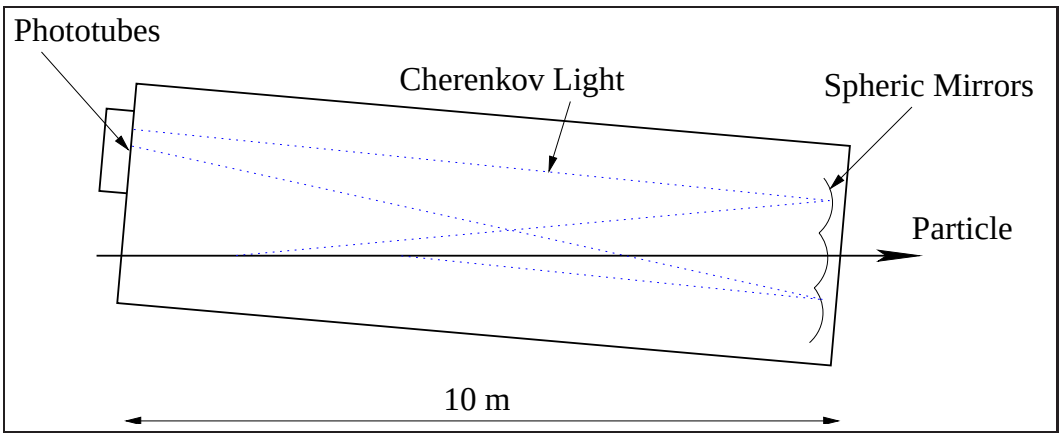

Figure 2.11: Schematic view of RICH detector.

The RICH detector was used to identify the likelihood that a track was an electron, muon, pion, kaon, proton, hyperon (like a Σ), or background. K/π separation was possible up to 165 GeV. Since many charm decays have kaons in the final state, the separation of the kaons from the more numerous pions is a vital feature for any charm experiment. The RICH allowed a 2 σ seperation between kaons and pion for 100 GeV/c^2 tracks (figure 2.12).

The ring radius grows with the velocity of the particle (Figure 2.13). The $\beta = 1$ particle has a ring radius of 11.5 cm, with 13.6 hits on the ring. Each hit was measured with spatial resolution 5.5 mm, and ring radius r was measured with $\sigma_r = 1.8$ mm resolution in multi-track events, which allowed π/K separation up to 165 GeV [33]).

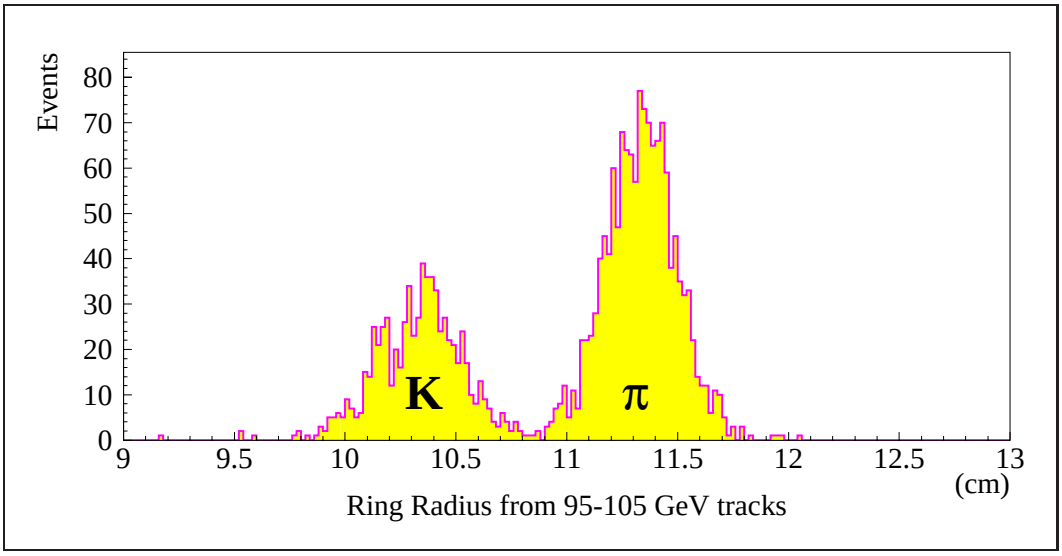

Figure 2.12: K/π separation at 95-105 GeV. [33].

2.8 Other SELEX Apparatus

The following systems were not used for this analysis, but may be of interest for further SELEX studies.

2.8.1 Electron Transition Radiation Detectors

The six ETRDs were positioned in the M2 spectrometer, to separate electrons from the hadrons. The transition radiation was generated in 200 polypropylene foils 17 μm thick positioned in front of each chamber. The radiation was detected by $103 \times 63\text{cm}^2$ MPWC chambers with 4 mm wire spacing and filled with the mixture of Xe and methane [32]. Since electrons have a smaller rest mass than any hadron, an electron will have a higher γ-factor than a hadron of the same momentum. This will result in more clusters counted (Figure 2.14).

2.8.2 Lead Glass Electromagnetic Calorimeters

Three lead glass detectors were used to identify and measure the energy of the photons and electrons. Also known as Photon Detectors, they were positioned at the end of M1, M2 and M3 spectrometers (Figure 2.1). Each

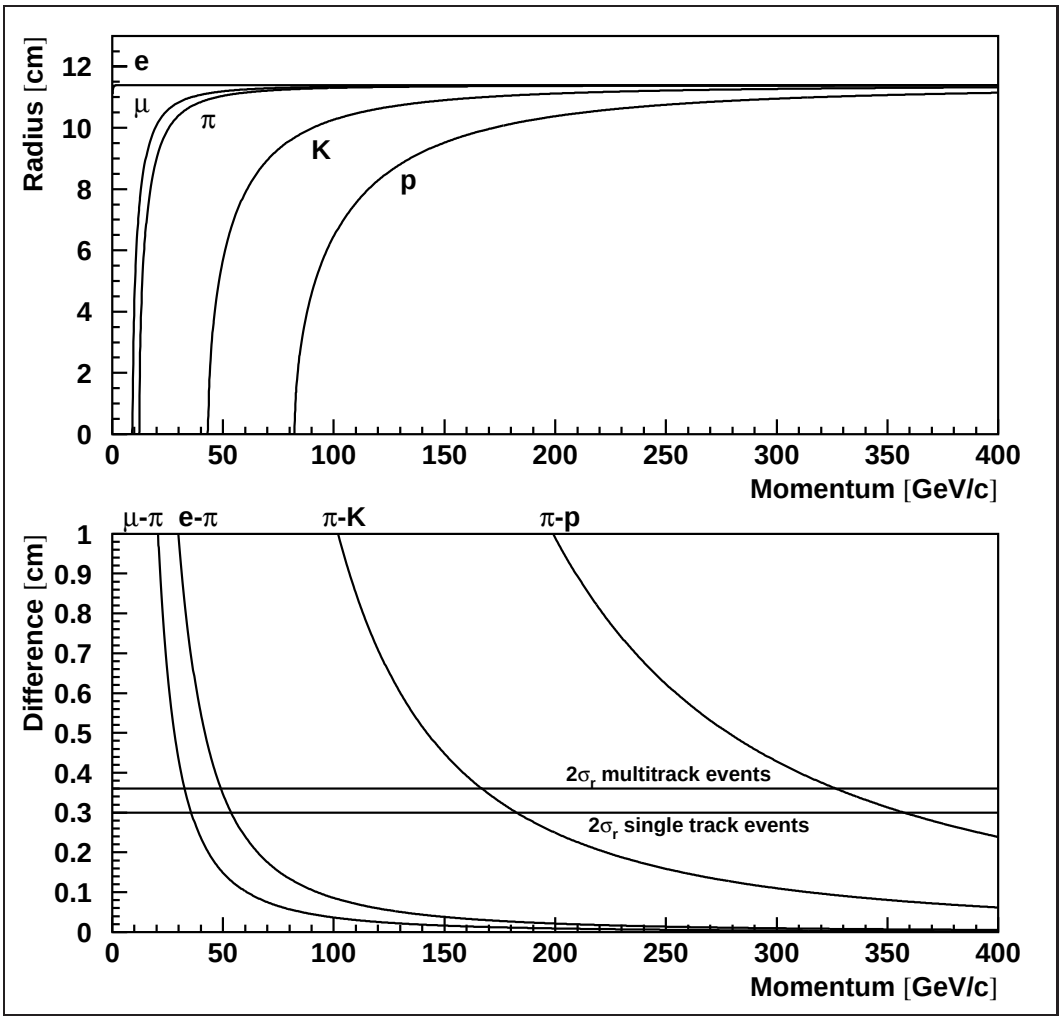

Figure 2.13: Ring radii (top) and separation (bottom) for different particles. The two horizontal lines on the lower plot show the achieved resolutions for the single track multiple tracks, respectively [33].

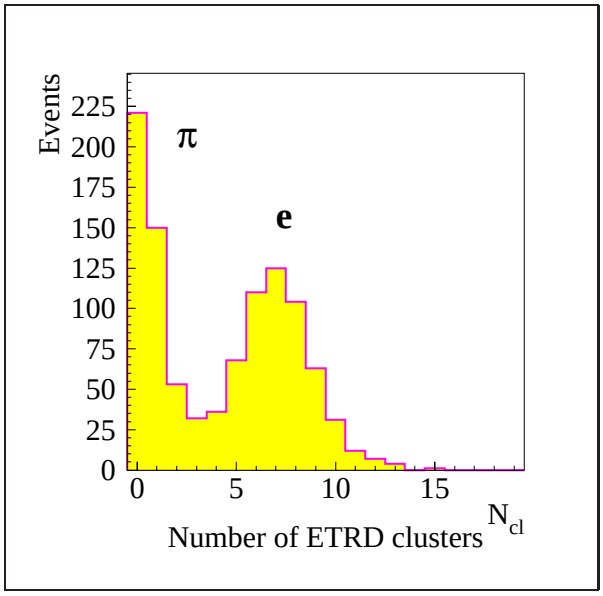

Figure 2.14: e/π separation using electron TRD

detector has hole in the middle to let beam and high energy particles through. Lead glass has density $4.1\,\mathrm{g/cm^3}$ and radiation length 2.5 cm. The first 2 calorimeters were composed of blocks of 2 different sizes, smaller size blocks $4.25\times4.25\times34\,\mathrm{cm^3}$ covering inside of the detector and bigger size blocks $8.5\times 8.5\times34\,\mathrm{cm^3}$ covering the outside of the detector [34]. The third calorimeter was built out of the same size blocks $3.8\times3.8\times45\,\mathrm{cm^3}$ [35].

2.8.3 Vector Drift Chambers

Tracking downstream of the RICH is done with three stations of vector drift chambers (VDC), known as VeeA, VeeB, VeeC [36]. The first 2 stations were located in in M2 spectrometer and the the third one in M3 spectrometer (Figure 2.1). Each station had three chambers with a $116\times116\,\mathrm{cm^2}$ aperture, about 90% efficiency and $\sim 100\mu$m resolution. The stations measured tracks in x, y, u or in x, y, v projections. Each chamber has 8 sensitive planes in the fine cells of the center region of the chamber. In the coarse cells it has 6 sensitive planes. So each chamber measured a track projection with up to 8 hits, allowing position and direction measurements. [36]

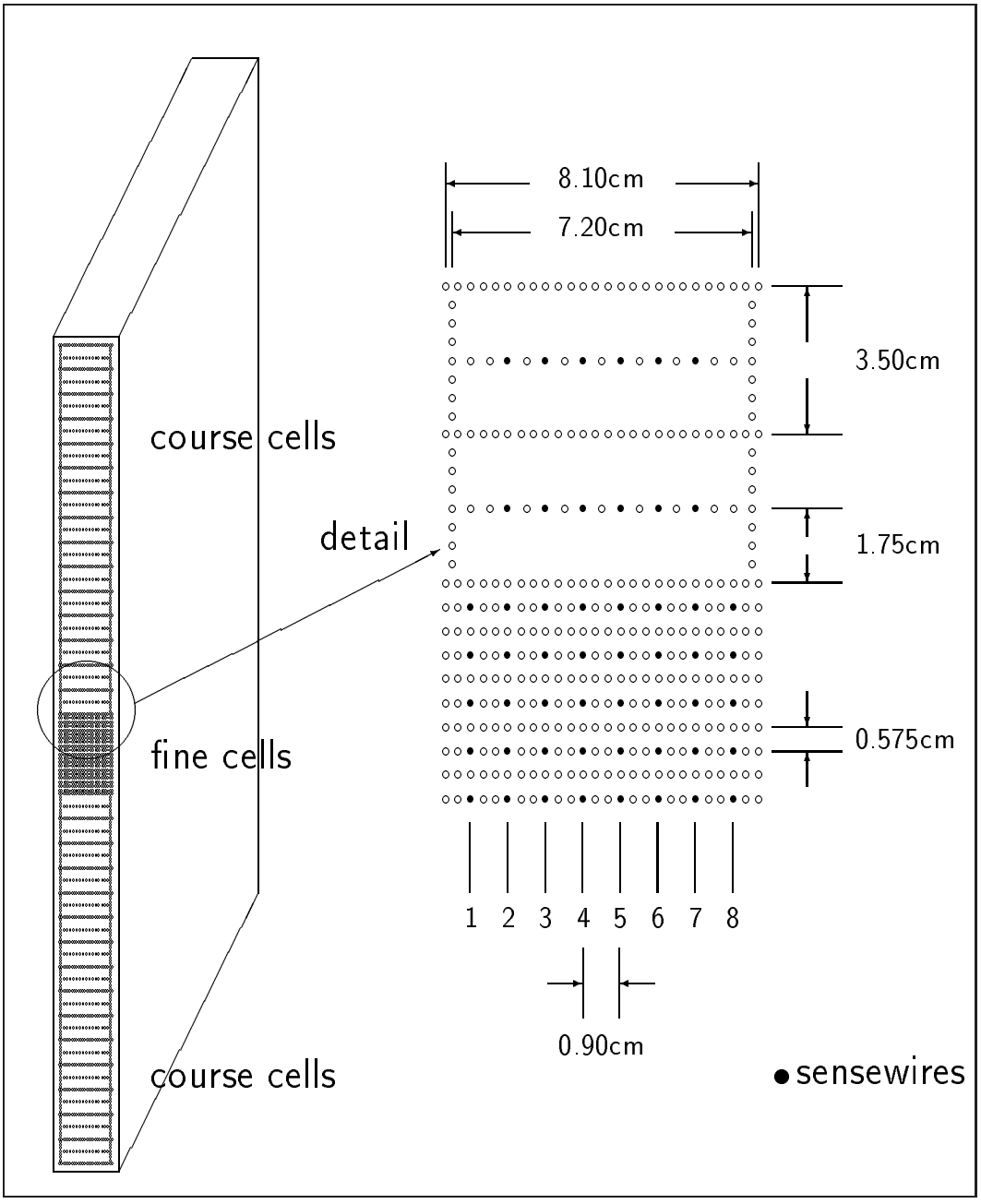

Figure 2.15: VDC chamber layout

2.8.4 M1 Drift Chambers

The M1 spectrometer has 2 drift chambers, each with 2 sensitive planes measuring hits in x projection. Chambers have $2.4 \times 1.7\,\mathrm{m}^2$ acceptance, they are about 80% efficient and has about 0.7 mm resolution [37].

2.9 Trigger and data acquisition system

The SELEX trigger used a set of scintillation counters (S1-S4), veto counters (VH1,VH2), interaction counters (IC) and 2 hodoscopes (H1,H2) shown on Figure 2.16. The T0 trigger defined a beam particle as the coincidence of S1,S2,S4 counters with no hits in veto counters VH1 and VH2. This was to prevent beam interactions before the charm targets (with the beam silicon, for example).

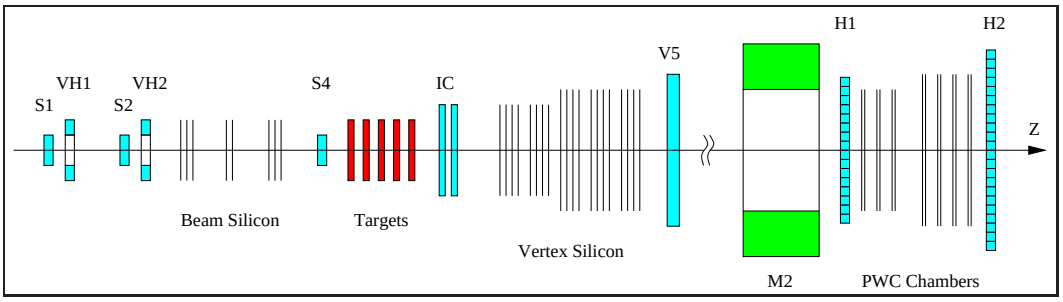

Figure 2.16: Schematic view of SELEX trigger elements

The next task of the trigger is to determine if there was an interaction in the charm targets. Most charm experiments also very loose triggers [38, 39], selecting just events with interactions. Aside from the secondary vertex from the charm particle decay, it is difficult to find kinematic features distinct from background. The charm mass is not big enough to make an efficient trigger on events with large transverse momenta p_T, which is common in b-physics experiments.

The interaction counters produced an output signal which amplitude was proportional to the number of particles that crossed them (Figure 2.17). The IC consisted of the two separate thin counters, and amplitude of the signal in each counter was measured. Using the smaller amplitude from the two counters for the particle multiplicity test greatly suppressed the effects of the Landau fluctuations of the amplitude in the individual counters [40].

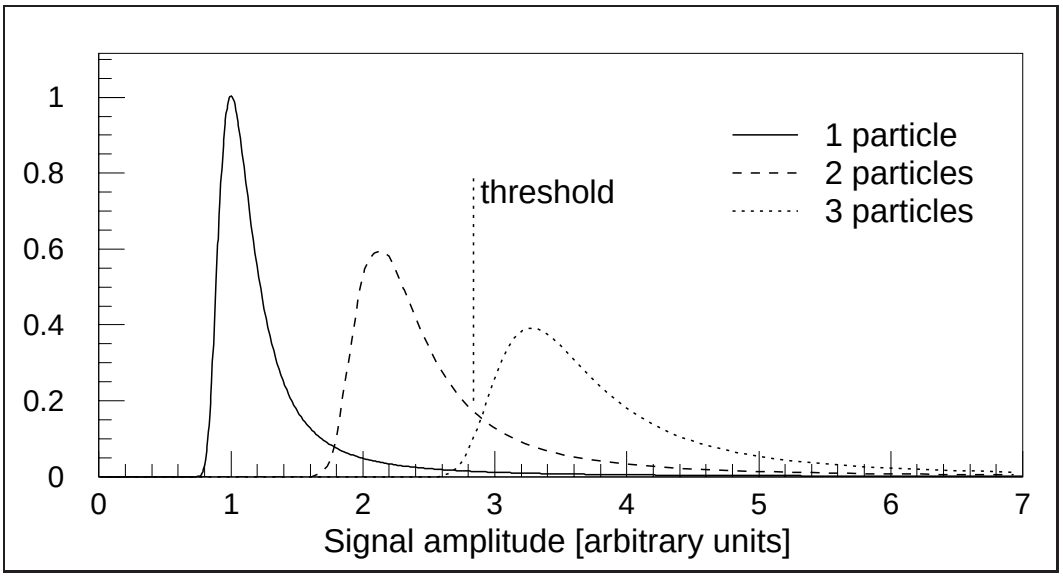

Figure 2.17: Simplified picture of multiplicity measurements in the interaction counters using the amplitude of the signal [40]. If the amplitude of the signal was greater than the threshold than multiplicity was considered to be greater than 3. The long tails of the amplitude spectra are due to the Landau fluctuation of the ionization losses. Combining information from the two counters greatly reduced the effect of the Landau fluctuations.

The T1 trigger required a signal from the interaction counters, a signal from the Beam TRD and 2 hits in the positive region of the hodoscope H1 [41],[42]. An interaction in the targets was defined as the signal from the interaction counter IC larger than signal from 3 minimum ionizing particles. In early runs the Beam TRD was not used, so that data contained both π^- and Σ^- beam particles. In later runs the Beam TRD was used to trigger only on baryons (Σ^-, p).

The hodoscopes lie downstream of the M2 analysis magnet. The SELEX experiment was designed to observe large x_F charm hadrons. Since the charm quark has a positive charge, we expect to find more positive tracks in the M2 spectrometer, compared to non-charm background.

Along with the charm trigger, there were other triggers which included a hadron-electron scattering trigger to measure electromagnetic radii of hadrons [40], an exotic trigger to study certain 3-prong events [43], and special calibration triggers to check apparatus performance. Each trigger acted independently of the others.

For high x_F charm, the relativistic boost is enough that there should be evidence of secondary vertex from the charm decay, distinct from the primary interaction vertex from the beam track and the charm target. To this end, events that pass the trigger are passed to a software filter. The code did a full reconstruction involving the beam track and (high momentum) tracks that reach the M2 spectrometer. Any tracks that reached the RICH were also given particle identification. An event will then pass the Filter if it has RICH identified particles that we associate with charm decay, or if one or more of the tracks appears to miss the primary vertex. A more complete overview overview of the Filter is in Appendix B.

Special studies showed that the Online Filter decreased the background by a factor of 8 and was about 50% efficient for a typical charm signal. The events taken with the filter off were processed by the full offline analysis code to find the D meson and Λ_c charm events. The same events were run through the filter, offline, to see which charm events passed. While the filter lost some charm events, the amount of charm per recorded event increases with a significant reduction in the number of data tapes written. Processing of all the tapes took us about half a year, so the factor of 8 played an important role in speeding up physics results.

As events passed the trigger, the detectors were signaled to read out their information, which was digitized, packed and buffered into dual-ported memories [42]. There were about 80000 trigger events read out during a

20-second (slow) beam spill, followed by 40 seconds of no beam. The events were passed to a 17-processor SGI Challenge computer, with each processor running an independent (but identical) version of the SELEX Online Filter code. Events that passed the filter were written out to disk. Events on disk were sampled by the monitoring program to check the apparatus performance during data-taking. Size of one event was about 6.5 kB. Events from disk were combined in 200 MB files, which were written to tapes and stored for the further processing. SELEX charm trigger rates are summarized in Table 2.2.

trigger/beam	definition	rate
proton beam	800 GeV protons from Tevatron	$4 \cdot 10^{10}$ Hz
Σ^-/π^- beam	600 GeV secondary beam	600 kHz
T0	$\mathrm{S1} \cdot \overline{\mathrm{VH1}} \cdot \mathrm{S2} \cdot \overline{\mathrm{VH2}} \cdot \mathrm{S4} \cdot \mathrm{V5}$	20 kHz
T1	$\mathrm{T0} \cdot (IC > 3) \cdot \mathrm{BTRD} \cdot (\mathrm{H1}, \mathrm{H2} > 2\,\mathrm{pos})$	4 kHz
Online filter	Event has more than just a primary vertex	500 Hz

Table 2.2: SELEX charm trigger rates

The schematic diagram of the SELEX trigger and DAQ is shown in Figure 2.18.

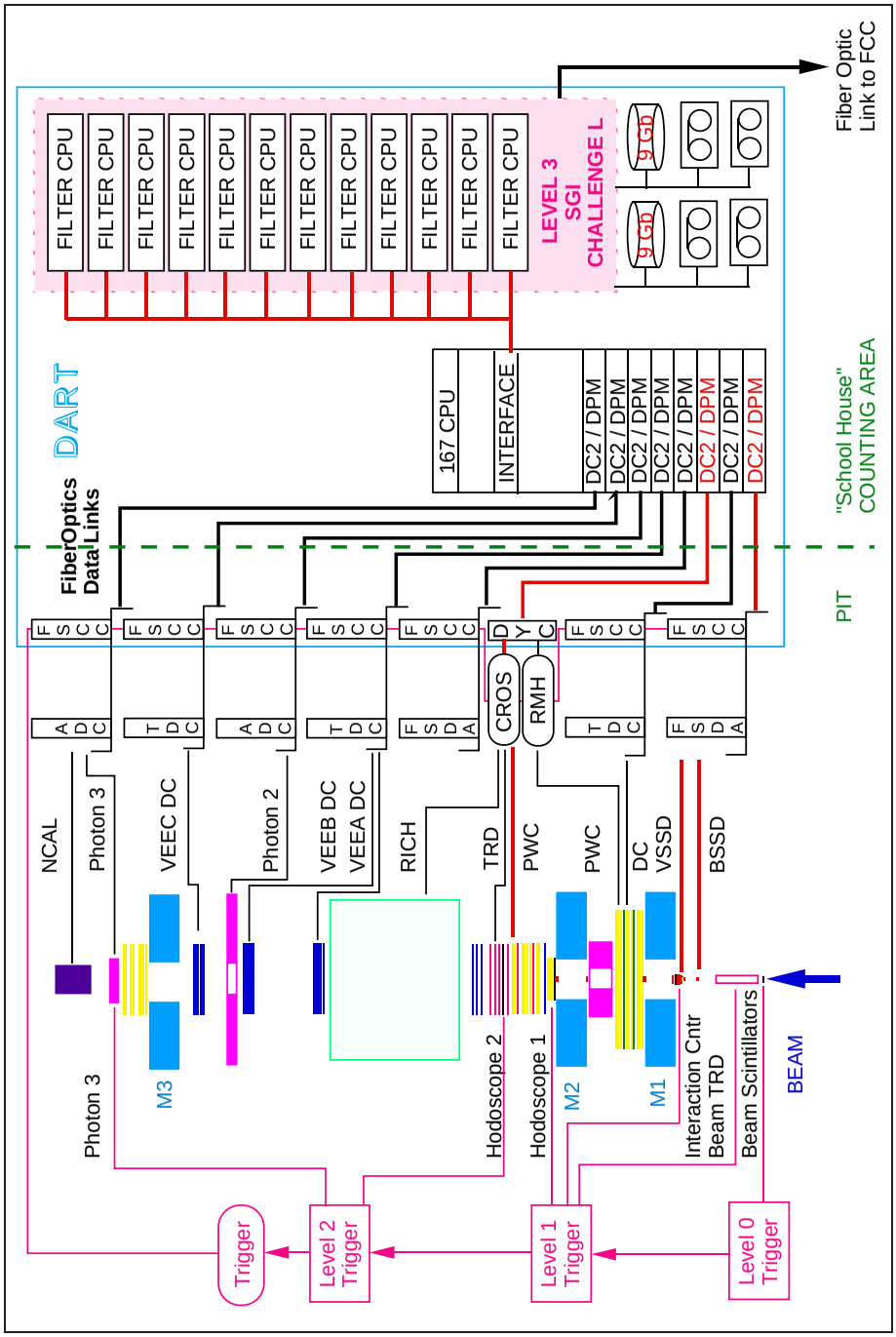

Figure 2.18: Schematic view of SELEX Trigger and DAQ systems

Chapter 3

Analysis

This chapter will detail what data were used, how it was analyzed, and what cuts were used to form the final signal sample. The definitions and procedures are described here, with the results in the next chapter.

The reconstruction of interest is $\Xi_{cc}^{++} \to \Lambda_c^+ K^- \pi^+ \pi^+$, with $\Lambda_c^+ \to p^+ K^- \pi^+$. This mode has all charged tracks, and two decay vertices.

3.1 Fixed Target Run

The SELEX experiment received beam starting in July 1996. Since this was a new experiment, the first months were used to get the trigger, detectors, and software operating at a high enough level for quality data taking. Data was written to tape during these initial months, but it was decided not to use them in later analyzes. Data taken after February 1997 was used in the charm analysis. The first set of data had a combination π^- and Σ^- beam. The next set included the Beam TRD in the T1 trigger (Section 2.9) to select mostly Σ^- interactions to be written to the tape. For the third set, the polarity of the hyperon beam was reversed, which provided beam composed of mostly protons (Figure 3.1). Overall, the experiment took data for almost year and a half.

Periodic alignment runs were taken to At the same time, a small sample of data was written without selection by the online filter. During all of the runs, the detector performance and the Online Filter were monitored. Special runs were also taken to study π^-, Σ^- and p total cross sections [44], [25]. Also, each day three small (about 100K events) data sets were collected

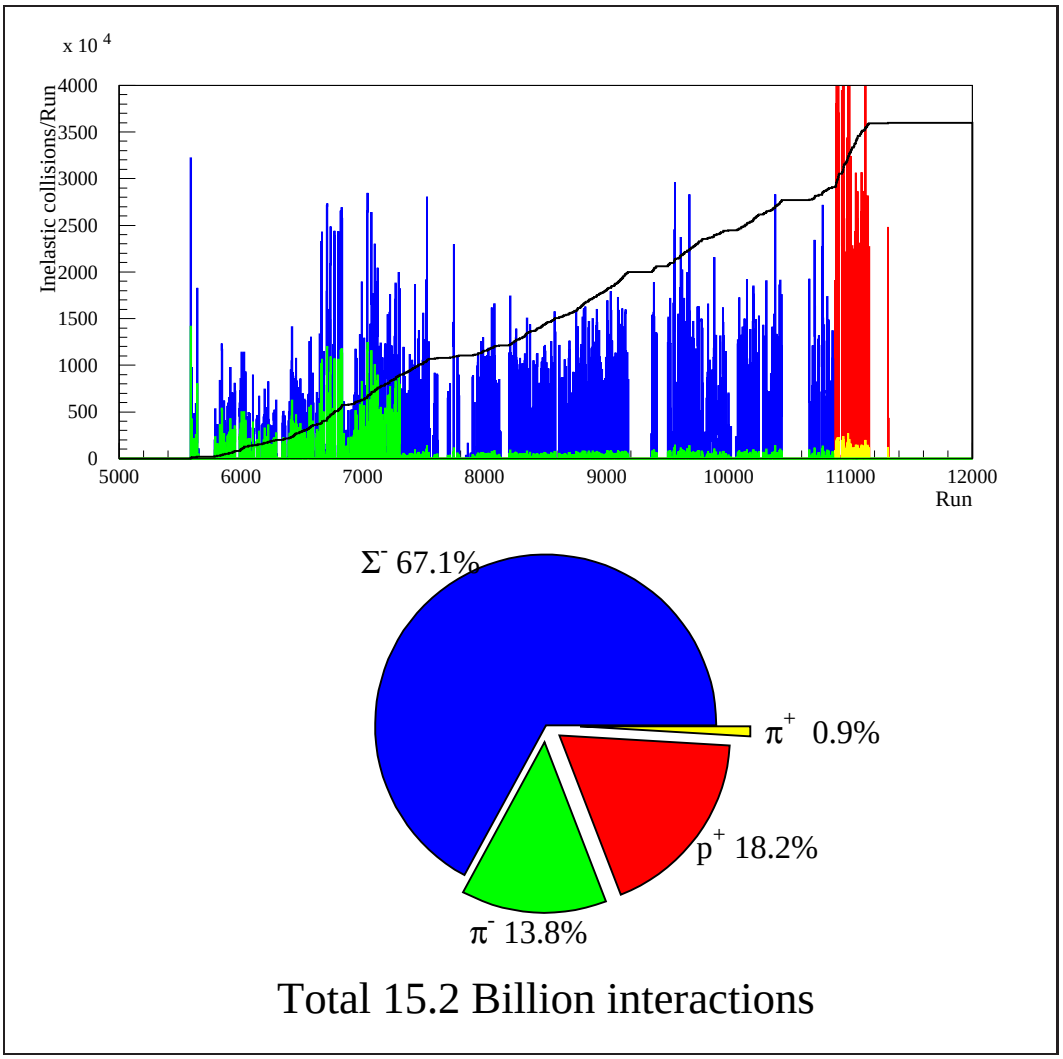

Figure 3.1: SELEX data sets

with the filter off. The first two were with the trigger accepting only beam tracks without interactions. The first was with the analysis magnets (M1, M2) turned off, for the second they were turned back on. These were used to align the geometrical positions of silicon detectors and downstream PWC chambers. The third used the normal trigger configuration, to provide an unfiltered data set that was used to test filter timing and performance offline.

3.2 Data Set

Charm data refers to events written to tape that passed the trigger and filter requirements. The trigger requirements were that a beam particle interacted in the target stack, with multiple charged tracks passing through the interaction counters. The hodoscope counters, after the second analysis magnet (M2) need to detect particles, especially in the positive side (the side where positive charged particles would be deflected by the magnets). This requirement tests for high momentum tracks, which would be associated with high x_F events, and for high momentum positive tracks that might come from charm. The online filter requirements are explained in more detail in appendix B. In brief, the filter removed events that could not be analyzed or having all high momentum tracks coming from the primary interaction vertex. A charm hadron will travel a distance away from the primary vertex, depending on its lifetime, and form a secondary decay vertex. This will show up in reconstructions as a track that misses the primary vertex. The filter checks the miss distance of all found tracks compared to the primary vertex.

Once the data taking was finished, the charm set was analyzed with the full analysis software, which took several months. The pass over the data ("Pass 1") was used to observe charm signal, improve alignment tables, and to continue development of the analysis software. A loose set of cuts were used to select events with charm baryon candidates. These events were stripped off, and this subset of the data will be referred to as the "(charm) Baryon Restrip".

3.3 Standard Analysis

The analysis software is known as SOAP, SELEX Online/Offline Analysis Program. The same code was used for the filter (online) and for later analysis

(offline), although not in the same configuration. The program was designed to be highly flexible and customizable. The online version was optimized for speed, and concentrated on high momentum track reconstruction, vertexing, and particle identification. The offline version included analysis software for all detector systems, based on what the user wanted to find. The following subsections will describe in brief the steps done for this search.

3.3.1 Unpacking

The first step is to unpack the data that was written to tape for a particular event. For each detector, the hardware creates a list of which wire/silicon strip/phototube had a signal, or hit. At the software level, this list of hits is converted to positions in the detector's local coordinate system. These hits will be used to fit the path of particles passing through the detectors.

For systems like the wire chambers, each wire that is read out is given a detector hit. For the vertex silicon, the hardware is designed to measure the amount of charge present in each strip. A charged particle passing through the silicon will leave behind, on average, one MIP (minimum ionizing particle) worth of freed electrons. If two charged particles pass through the same strip, we expect to read out (roughly) two MIPs of charge. At the same time, the charge deposited by the particle can diffuse to neighboring strips before it is read out. To take care of these two processes, a routine is written to "cluster" the vertex silicon information. Based on how many neighboring strips are read out and the sum of the charges read out, an algorithm is used to calculate how many charged particles passed through a local area, and the (charge-weighted) position of those particles.[26]

Accurate tracking depends on having high efficiency for generating hits for real particles, and good rejection for electronic noise that could be treated as a hit. Noise hits were suppressed at both the detector (hardware) level, and at the offline (software) level by requiring enough charge to suppress noise fluctuations just above the electronic threshold but much less than one MIP equivalent.

3.3.2 Tracking

SOAP has a number of different routines written to try to find the path of particles through the detectors. The most general situation involves the M1 and M2 PWCs, and the vertex silicon. Since these detectors are in magnetic

field free regions, charged particles should pass through the detectors in a straight line. The algorithms assemble a list of hits from a particular detector system, and tries to determine if they are consistent with a line fit. If the code determines that the fit is of high enough quality (based on chi-square to the fit, and the number of detector hits used), those hits are marked as used, and a track segment is added to a list. A segment is assumed to be the path of a charged particle through a specific spectrometer.

A separate list of tracks is made, with links to one or more track segments, although at most one segment per spectrometer. Each track is associated with a charged particle. If a track has segments on both sides of a magnet, a momentum fit is made. If the track passed through the eTRD or the RICH, the particle identification code will run after tracking to make a mass assignment.

If we have track information, we can use that to narrow the search in spectrometers that haven't been examined yet. The track is projected from where it is known in other detectors, into the searched spectrometer, to see if there are hits along the path. This procedure has been called "guiding", and greatly reduces time and confusion.

Going into much greater detail is outside of the scope of this thesis, considering the size of the software code and the number of routines involved. The algorithms have to account for fake hits from noise or hot electronics, missing hits from dead electronics, and confusion from other tracks that pass nearby. Since each detector plane only has information for one dimension, this can increase the ambiguity. The tracking code is optimized for long lived particles. If a particle decays part of the way through a set of detector planes, it is uncertain whether the code will miss it entirely, find a short segment (up to the decay point), or if it will combine a list of hits from more than one track to try to form a longer segment.

As an anecdote, there was one event where the M1 spectrometer had many particles passing through the PWCs. If the routines were run in a certain configuration, ten high quality segments were found. If the routines were run in a different configuration, ten high quality segments are found, involving many of the same hits, but with completely different fit parameters. That is another reason why using all available information, like in "guiding", is important to try to reduce ambiguity.

Figure 3.2 shows the tracking for an example Λ_c^+ event.

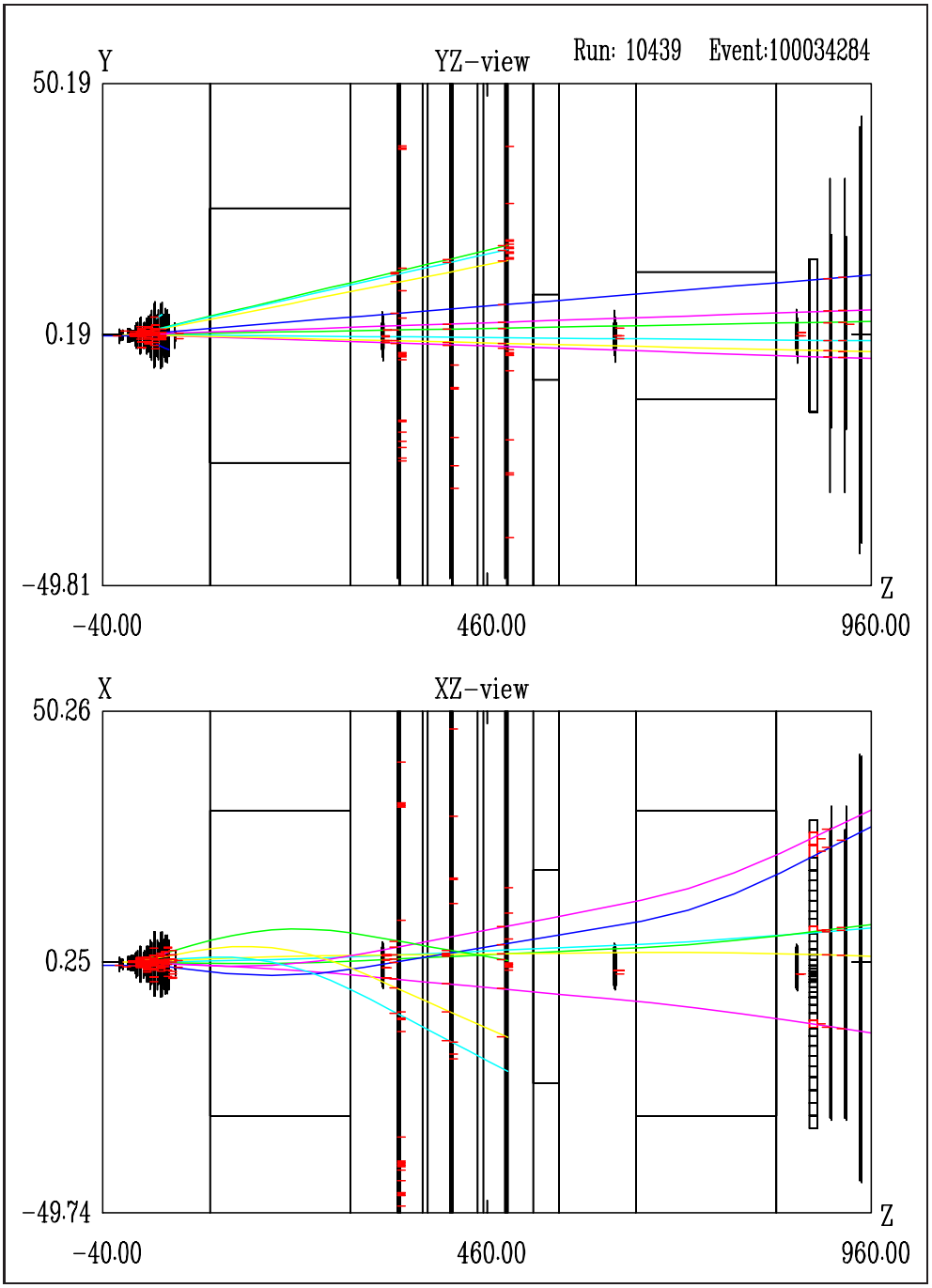

Figure 3.2: Event display of a sample Λ_c event. Horizontal and vertical axes are on different scales, in cm. The top projection is x-z view, while the bottom projection is y-z. The track paths are drawn based on the fit parameters and the expected trajectory through the magnets.

3.3.3 Particle Identification

The RICH software produces probabilities that the track is a certain particle, normalized to the hypothesis with the greatest probability. The track information from detectors outside the RICH determine the momentum and position of the ring center. Particles with different masses would have different radii, and the measured radius is compared with the predictions. A likelihood function was formed to describe how close the predicted radius matched the measured radius. The likelihoods were then normalized to that of the most likely hypothesis, which was assigned 1. The hypothesis of interest being checked are proton, kaon, pion, and background. (Information also exists for sigma, electron, and muon.) This procedure give the relative probability that a given track is a particular species.

The RICH detector is vital to reducing background. For the Λ_c^+, the proton and kaon tracks must be given particle identification consistent with being a proton and kaon, meaning that the hypothesis likelihood must be equal to or greater than the likelihood that the track is a pion. If we require a pion, the usual definition is that the normalized likelihood be greater than 0.1 .

Figure 3.3 shows the same example Λ_c^+ event, with the RICH phototubes.

3.3.4 Vertexing

The next task for SOAP is to look for the primary interaction vertex and any secondary vertices, space points where two or more tracks intersect. This will be a list of possible places for particle decay or interaction with material in the detector. The routines that look for intersections in the spectrometers far downstream of the target stack were not used for this study. The two routines that were run, vertex1 and vtx2, try to find vertices near the target stack. The primary vertex includes the beam track, the target foil where the beam particle interacted, and the charged long-lived tracks that were produced from this initial interaction. The secondary vertices represent places where short-lived particles (like charm hadrons) decay into charged tracks, or where particles from the primary interaction collided with material in the detector to produce a secondary interaction.

For this study, only vtx2 was used. While the two routines are similar and find many of the same vertices, they are not identical. The charm baryon restrip file represents all of the charm baryons found by vtx2 in the pass, but

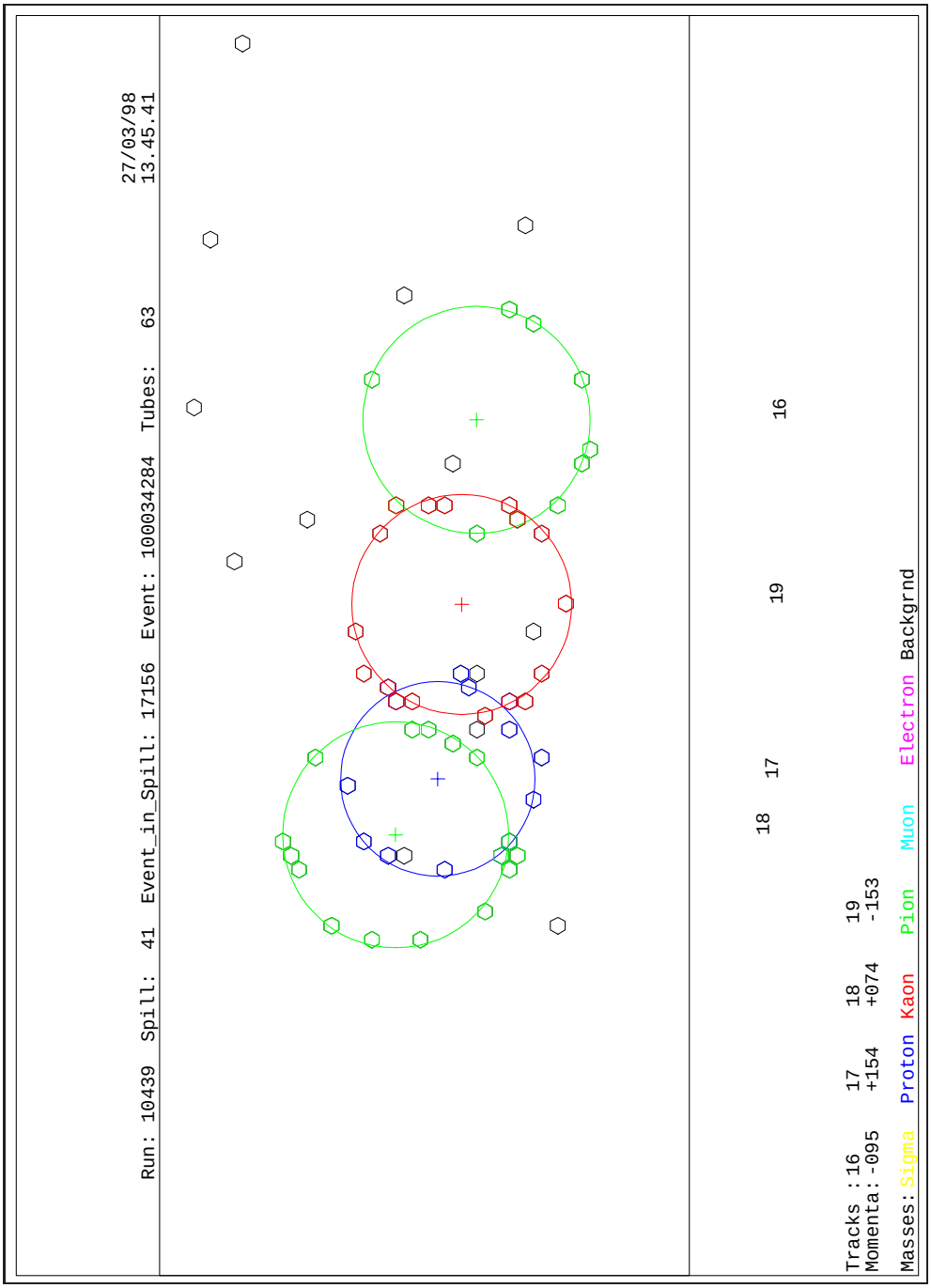

Figure 3.3: Rich view of a sample Λ_c event. The ring centers and particle momentum are based on tracking parameters. The circle is drawn for the most likely mass hypothesis.

only a majority of the vertex1 charm. More information on vertex1 is given in Mathew's thesis[26]. Vtx2 is described in detail by by Kushnirenko[17].

Vtx2 starts by generating a list of tracks that are believed to start near the target foils. In general, this consists of tracks with a vertex spectrometer segment, and another downstream segment to provide a momentum estimate. The beam track is included to improve primary vertex position resolution. If all tracks give a satisfactory χ^2 to a fit for a single primary vertex, the event was rejected. For events that fail this single vertex selection, all combinations of 2, 3, and 4 tracks in the track list were checked to see if they intersected at a common (secondary) vertex. The code makes a nonlinear fit to find the best three dimensional spacepoint for this vertex. The quality of the vertex is measured by χ^2, based on how far the tracks in the fit missed the spacepoint, weighted by the track parameters uncertainties. If this secondary vertex is judged of reasonable quality, a search is made for a primary vertex. The remaining tracks not involved with the secondary vertex fit are checked to see if a subset was found that would intersect with the beam track at one of the targets. A fit is made to find the primary vertex spacepoint. Based on the chi-square, tracks that miss the primary are removed, and the vertex is refit. If the code determines that the primary vertex is of reasonable quality, the secondary-primary vertex pair is added to the list of possible vertices, and the next permutation is tried.

Unlike tracking, where we try to make a unique association between tracks and (real) charged particles, vtx2 presents a list of multiple hypothesis. Within a secondary-primary vertex pair, a track can be assigned be assigned to only one of those two vertices, or not used at all. The primary vertices will be almost identical, with the major difference being which tracks are not used (since they were used for the secondary vertex). If we have a valid 3-track secondary vertex, we could reasonably expect to find the list of secondaries to include the three 2-track subsets.

A common source of background occurs where the code pulls the actual primary vertex into many secondary-primary pairs. These tend to lie close together and are suppressed by requiring a statistically significant separation between the secondary and primary vertex.

Figure 3.3 shows the primary and secondary vertices for the same example Λ_c^+ event shown earlier.

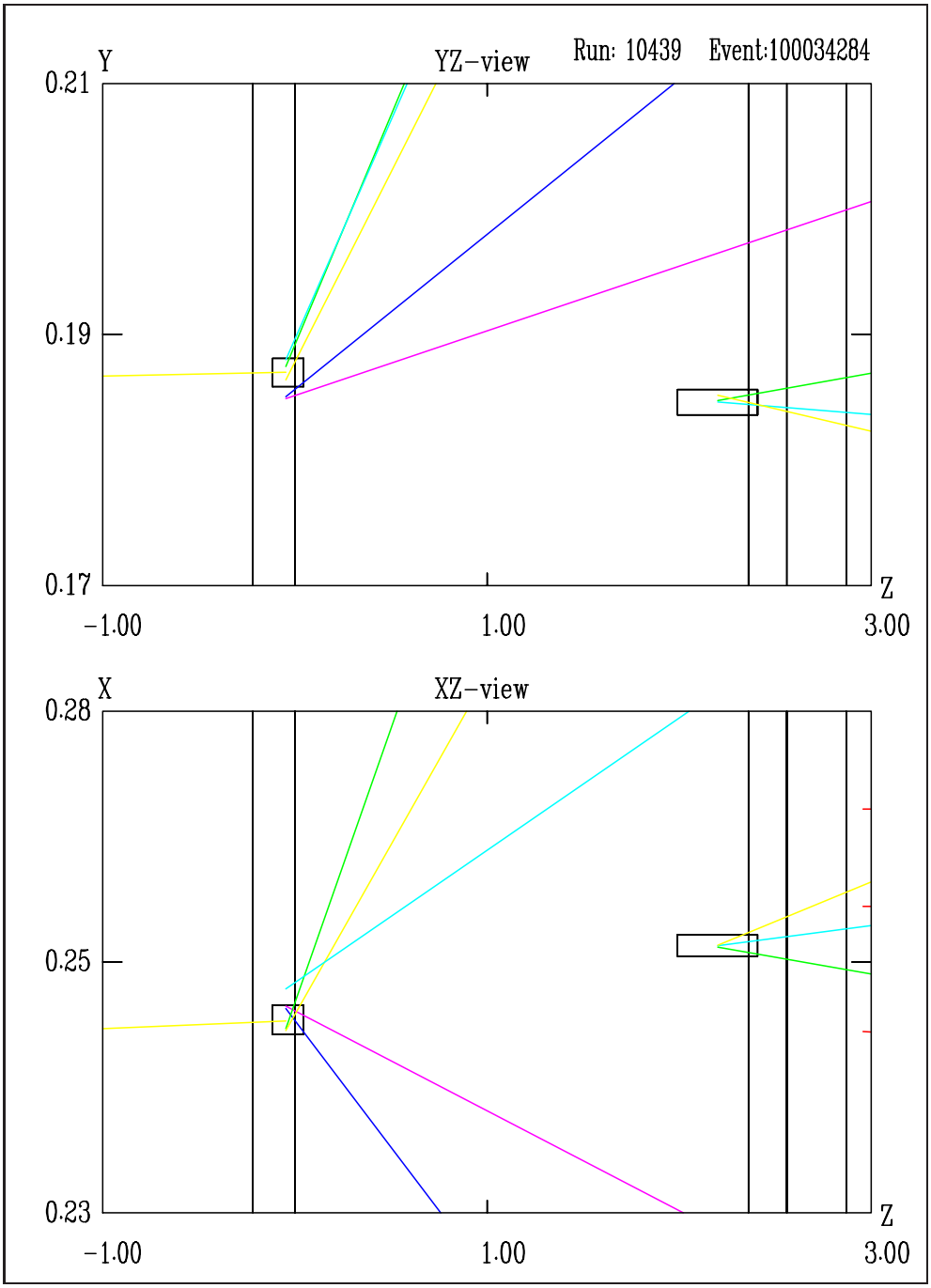

Figure 3.4: Vertex view of a sample Λ_c event. The scales are in cm. The boxes show the scale of the vertex errors.

3.3.5 Recon

The purpose of running the analysis software is to identify real particles that passed through the detector. A reconstruction is the recipe for combining tracks in the experiment to form a particle candidate. Masses are assigned to the tracks, so the relativistic mass and momentum can be computed for the combination of tracks. Random combinations of tracks will produce background in the mass plots. For real particles, the mass of the reconstruction should all be within a narrow range, depending on the detector resolution and the mass width of the particle. This should show up as a peak above background in the mass distribution for the reconstruction.

A table of reconstructions, or recons for short, is written by the user, to let SOAP know which particle decays the code should try to find. Each recon consists of a text title (usually the particle being reconstructed), the number of tracks that the particle decays into, the particle definitions made for those tracks, and any quality cuts made to reduce background. If a valid candidate is found, the momentum and mass of the recon is made, using the momentum of the tracks and the assigned particle mass for each of the tracks.

Similar to vertexing, there can be many candidates for a given reconstruction. In fact, the same set of tracks can form multiple candidates, as long as the particle mass assignments for the tracks are different. Since each reconstruction in the table can operate independently from the others, tracks can appear in many reconstructions.

The particle definitions may or may not use information from the particle id code. For example, most reconstructions that assign a kaon mass to a track require that the RICH probability for a kaon be higher than the probability that the track is a pion. This requires that the track passes through the RICH, which will limit the geometry of decays that will be found by the reconstruction. To increase the acceptance, some reconstructions will also use tracks that do not reach the RICH, and assume a given mass assignment.

For this search, we started with reconstructions involving the vertex list. Secondary vertices with the desired number of tracks are selected. All permutations of the tracks in the vertex are tried with the particle definitions. Each permutation that passes the cuts will be added to the list of recons. The same vertex can be used for more than one recon, but track/particle definition associations will be different. This will generate the list of $\Lambda_c^+ \to p^+K^-\pi^+$ candidates needed for the search.

The other type of reconstruction used is built from a combination of other reconstructions and tracks. For example, a D^* entry might include all D^0 reconstructions found earlier, with an additional charged pion added. For this search, the Λ_c^+ candidates are combined with three other tracks (not used in the Λ_c), to form the $\Xi_{cc}^{++} \to \Lambda_c^+ K^- \pi^+ \pi^+$ candidates.

3.3.6 Post-Recon Analysis

At this point, the SOAP code writes out its results. Part of the output is the recons found, in PAW ntuple format. The recons were designed to find all possible solutions, within the limitations of time and data space. To identify a real charm decay out of the candidate reconstruction list, the next step is for the user to apply more stringent requirements or cuts. A partial list of parameters for the recon candidates are defined below. Figure 3.5 is shown to help illustrate the cuts.

- L_z - separation between the primary and secondary vertex pair. For real particles, this will depend on Lorentz boosted lifetime.

- σ_z - uncertainty in the z separation between the two vertices. Each vertex has an error ellipse for its position. The z errors of the vertices added in quadrature. The size of the errors depends in part on the errors of each track used in the vertex, partly on the geometry of the tracks. In general, increasing the momentum results in larger z uncertainties.

- L/σ - weighted separation between the primary and secondary vertex pair. Since almost all of the motion is in the z direction, we use L_z/σ_z instead of the three-dimensional separation. This quantity is used to separate between short lifetime background and long lifetime signal, since both L and σ are Lorentz boosted.

- pointback - a measure of how well the secondary reconstruction momentum vector points back to the primary vertex. This depends on the positions of the two vertices, the momentum vector, and the size of the vertex spatial error ellipse.

- scut($index$) - a weighted measure of the distance by which a track misses the primary vertex. The x-y miss distance is weighted by the squares of the track transverse coordinate errors. For scut, each track in a reconstruction is compared to the primary vertex, and the values are ordered from largest to smallest. $index$ refers to the rank of the value in the list. For example, scut(2) is the value of the second largest weighted miss distance.

- p_t - Transverse momentum of the reconstruction, usually with respect to the beam direction. Sometimes it is the transverse momentum of a track with respect to the reconstruction.

- x_F - Feynman x, the fraction of the beam momentum available for this decay. The exact calculation uses $x_F = 2p^*_\parallel/\sqrt{s}$, where s is the center-of-mass energy, and $p^*_\parallel$ is the particle's momentum parallel to the beam direction. Since the tracks are at small angles compared to the z axis, and the momentum of the particles are much larger than their rest masses, $x_F \approx p_z/p_{beam}$.

3.4 Data Samples

Next we need to outline which reconstructions will be examined.

3.4.1 Λ_c Sample

To identify Λ_c^+ candidates we included a reconstruction requiring a three prong vertex with charge +1. The tracks were given p^+, K^-, and π^+ definitions. The p^+ and K^- tracks had to have RICH identification consistent with the definition. The third track was assigned to be a π^+, but was not required to reach the RICH. If it did, it was required to be consistent with being a π.

The normal Λ_c^+ sample has the cut $L/\sigma > 8$. For cases where the background needs to be reduced, we also apply the cuts pointback < 1200, and scut(2) > 4. The candidates that pass the additional cuts will be referred to as the "clean Λ_c sample". The signal region refers to all candidates within 20 MeV of 2285 MeV.

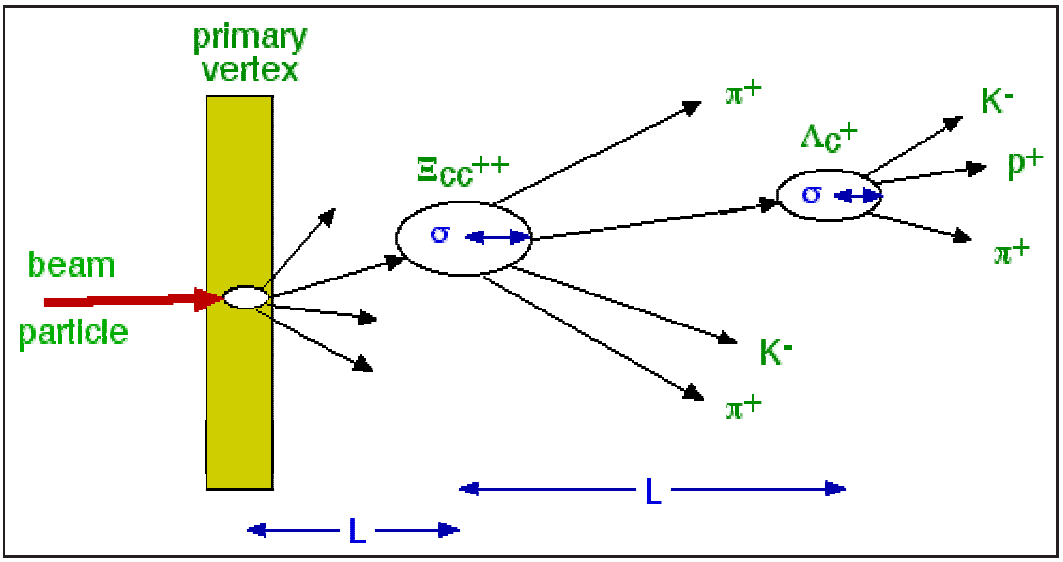

Figure 3.5: Illustration for analysis cuts.

The background is assumed to consist of random combinations of tracks, as well as mismeasured or partially constructed charm decays. Lifetime studies show that the background has two components, one very short lived, the other with a charm-like life. The L/σ cut removes the short, random background, and assures a reasonable separation of the decay point from the primary vertex. The pointback cut is used to remove background from strange decays or random track combinations that do not appear to be created from the primary interaction. The normal SELEX sample of Λ_c^+ candidates requires pointback < 12. However, since this search is for Λ_c^+ produced near, but not at, the primary vertex, the pointback cut was greatly relaxed. The scut selection is used to remove background where most of the tracks are from the primary vertex, with one stray track pulling the vertex fit downstream.

3.4.2 Search Sample

During the pass, the reconstruction $\Lambda_c^+ \rightarrow p^+k^-\pi^+$ was included, but not doubly charmed candidates. The data was reanalyzed independent of the pass to include these recons, as well as to implement improvements since Pass1. The charm baryon restrip file is small enough that the data can be

fully reanalyzed in days, instead of months.

For each Λ_c candidate, the event was searched to find three other tracks with net charge of +1. If the three tracks formed a vertex of adequate quality, the tracks were assigned particle identities of K^- and two π^+. That reconstruction was written out as a Ξ_{cc}^{++} candidate. Note that the primary vertex assigned to the Λ_c may contain some or all of the tracks used for the $K\pi\pi$ vertex, but the primary vertex assigned to the Ξ_{cc} candidate will not involve any of the six tracks used to make the reconstruction. Also, the vertex list was not used for the additional three tracks. We feed all combinations of $K\pi\pi$ tracks from the track list to the secondary vertex fitter.

Only Ξ_{cc} candidates from the clean Λ_c sample are used to minimize background. We apply a set of loose cuts to the raw Ξ_{cc} candidates to get a search sample. This set will be called the minimum bias cuts. The only assumptions are that we have two distinct decay vertices, with the second being a Λ_c coming from the first decay vertex. Also, these cuts have been used before (at different settings) to obtain the charm samples seen by SELEX.

- For the K$\pi\pi$ vertex, $\sigma_z < 1$ mm. This will reject poor vertex fits.

- L/$\sigma > 1$, for the primary and K$\pi\pi$ vertices. This will reduce background vertices that use tracks from the primary vertex.

- L/$\sigma > 1$, from the K$\pi\pi$ vertex to the Λ_c vertex. A cut requires a nonzero lifetime for the Λ_c candidate.

- Λ_c proper lifetime must be less than 2060 femtoseconds (ten Λ_c lifetimes), measured from the Λ_c vertex to the K$\pi\pi$ vertex. This should remove background from strange particles.

- Comparing the Ξ_{cc} candidate to the beam track, p_t must be between 0.2 and 2.0 GeV. This is the typical range for charm events; strange particles will be softer, and beauty particles will be harder.

- Remove $1.3 <$ L < 1.7 cm. We are seeing a build up of events around 1.5 cm, which is consistent with interactions in the next target foil. Reconstructions that occur at charm targets downstream of the primary

vertex are removed from consideration (for all vertex driven charm reconstructions), but the $K\pi\pi$ vertex fitting did not have the target check applied.

- For the K$\pi\pi$ vertex, the first π must have a larger p_z than the second. Without this cut, we would be double counting every candidate. For a pair of pions, they are free to form a 1-2 candidate, and a 2-1 candidate. This ambiguity was left in to make it easier to check for mass combinations, like Λ_c plus the first π to see if there is a resonance.

3.4.3 Monte Carlo simulation

To examine the expected performance of the analysis, a simulated Ξ_{cc} sample was generated. Since the production characteristics are not known, we made educated guesses based on the singly charmed Λ_c data sample.

A Ξ_{cc} was generated with a mass of 3.785 GeV, allowed to travel with a lifetime of half the Λ_c, then decays to a Λ_c, a K^-, and two π^+. The Λ_c moves with its appropriate lifetime, then decays to a proton, kaon, and pion. For all decays the daughter products are produced isotropically (in the center of mass frame), constrained by available momentum phase space. The generated Ξ_{cc} is given a transverse momentum with respect to the beam particle with a mean value of 1 GeV. The distribution follows the shape $d(N)/d(p_t) \sim exp(-apt^2)$. The fraction of the beam momentum has the distribution $d(N)/d(x_F) \sim (1 - x_F)^{3.5}$. Since the number of events with a large momentum fraction will be exponentially small, a separate sample was generated that was flat in x_F in case higher statistics were needed at high x_F.

To remove events that would not pass the SOAP analysis code, we apply some basic requirements. All tracks are required to have a momentum greater than 4 GeV. The proton and kaon of the Λ_c must make it past both magnet apertures, although they may not make it to the RICH.

A different sample without the Ξ_{cc} was generated, with the Λ_c produced from the primary interaction. Since we assume that almost all of the Λ_c events did not come from a doubly charmed baryon, it is useful to check if the systematics are artificially producing a signal. The Λ_c were produced flat in x_F and p_t.

The embedded charm event is added to a normal filtered event. The

real event is analyzed once to find a beam track and primary vertex. The embedded tracks are added using that starting point, rotated to account for the beam track momentum vector. The embedded tracks are extrapolated through the detector, and hits placed by the software based on detector hit efficiency. The analysis is then redone for the real plus embedded data.[45] The embedded particles will produce the signal, the underlying event provides the real background. Even with the online filter, most filtered events will not have charm in them. The software efficiencies and mass resolution found with embedded MC data were consistent with real data, for the high statistic strange (K_s, Λ_s^0) and charm (D mesons, Λ_c) samples.

The user needs to be aware of its limitations for production characteristics. For example, the embedded tracks are added to the underlying event, with nothing removed. The sum of the momentum of all tracks found, real and embedded, is likely to be more than momentum of the initial beam particle. Still, embedding has proven to be a useful tool in predicting detector response, such as geometrical acceptance and improving search algorithms. Although the overall x_F and p_T distributions will only be as accurate as the initial model, embedding will predict how well SOAP reconstructs events at a specific x_F and p_T.

3.5 Sideband subtraction procedure

The easiest way of estimating the number of signal events in a mass plot is to make a fit in PAW, with a gaussian for the signal, and a linear (or quadratic) fit for the background events. The primary problem is that the width of the gaussian is heavily influenced by events far away from the peak, the tails of the distribution. For a sample with limited statistics, the gaussian width for the fit is likely to be unreliable, especially if the background is not smooth. Another problem is that the signal is really a sum of many gaussians, with the same mean but different widths. If the detector had infinite resolution, the mass peak will be a spike, with a negligible width due to the uncertainty principle and a finite lifetime. In practice, there is limited precision, as well as the occasional outright tracking mistakes. The mass resolution depends on the momentum of the tracks, as well as which detectors are used for the track fit. In general, lower momentum tracks will have greater uncertainty, and will widen the mass peak distribution. So the PAW fit will be pulled wider by the events with poor mass resolution, and the overall peak shape

will be only pseudo-gaussian.

The standard SELEX procedure is to use embedding to obtain a value for the fit width, and then use that value in the PAW fit of the real data. Between the much higher statistics and the small, smooth background, the embedding width is expected to be more reliable than the real data for limited statistics. The embedded mass distribution has been verified with real data for the K_s and the larger charm hadron samples.

Once the width of the signal is fixed by embedding, we do a PAW fit for the real signal. This will establish the mean value of the mass, and an estimate of the signal size. The actual signal size will be determined by sideband subtraction. This will work if the background distribution is linear in mass. A mass region is chosen around the mean signal mass, which will consist of signal plus background. Another mass region of the same width is chosen from candidates away from the signal region, symmetric for mass above and below the signal. Since the background is linear, this will provide a count of the background. This can then be subtracted from the first value, to provide a sideband subtracted signal (sbs signal) count.

To show how this works, consider a signal at mass m_0, where essentially all the events N_0 are in the mass window $m_0 \pm w_0$. The number of background events at a given mass will be linear, given by $n_b = s(m - m_0) + b_0$. The signal plus background sample will have

$$\begin{aligned} N_{sig+back} &= N_0 + w_0(s(m - m_0 - w_0) + b_0 + s(m - m_0 + w_0) + b_0)/2 \\ &= N_0 + w_0(s(m - m_0) + b_0) \end{aligned}$$

Now we move away from signal region, and take mass sidebands from $m_0 - m_{sb} \pm (w_0/2)$ and $m_0 + m_{sb} \pm (w_0/2)$. This sample will have

$$\begin{aligned} N_{sideband} &= (w_0/2)(s(m - m_0 - m_{sb}) + b_0) + (w_0/2)(s(m - m_0 + m_{sb}) + b_0) \\ &= w_0(s(m - m_0) + b_0) \end{aligned}$$

which is the number of background events under the signal.

This technique will also be used to test the effectiveness of the cuts. A particular parameter is chosen, like x_F or p_T. The distribution for events for the (signal+back) region and the sidebands are plotted. We can then compare the sbs signal to the sidebands to see if there is a difference.

This will only work if the background is linear for the mass distribution, and that the distribution for other variables is the same regardless of the mass window chosen. An obvious problem will be mass reflections. An example of this are $\Lambda_c^+ \to p^+K^-\pi^+$ studies, where other charm like $D^+ \to K^+K^-\pi^+$ can appear in the plot if the K^+ can be defined as a proton. While this reflection will not have a charm mass, it will have the appropriate distribution for lifetime, x_F, and so on. If the reflection appears in a sideband, this will distort the sbs signal plot.

For this study into the unknown, we cannot account for mass reflections since we don't know what will contribute to it. The limitations of sideband subtraction were brought up to make it obvious which assumptions are being used.

3.6 Poisson distribution probability

For the next chapter, we will need to establish the significance of the signal size. The mass distribution will be divided into bins. The assumption is that the background will follow a Poisson distribution, with the probability given by P(n events) $= e^{-\lambda}\lambda^n/n!$, where the Poisson parameter λ is the mean number of events. The uncertainty is $\sqrt{\lambda}$. A linear fit to the mass distribution will provide the Poisson parameter for each mass bin. As the expected value λ gets larger, it will approach a gaussian distribution with mean of λ and $\sigma = \sqrt{\lambda}$.

The signal region will be excluded from the background fit. The Poisson parameter is computed for each mass bin, using the background fit. The number of events found in the signal region can then be compared to the expected number of events in the signal window, from the background fit. The probability that we would see a mass bump with n_{signal} events is given by:P $= \sum_i P_{Poisson}(i,\lambda) \times \delta(i)$, where $\delta(i)$ is 1 if $|i-\lambda| \geq |n_{signal}-\lambda|$, zero otherwise.

For a check, the same probability procedure will be done with sidebands. The signal region is still excluded, but a window of the same size, entirely in the sideband, will be selected. Those bins will also be removed, the remaining background is fit, and a probability for that sideband window to be a statistical fluctuation is computed. The sideband window will then be moved one bin, and the procedure repeated until the non-signal bins are all covered.

If all sideband regions have much higher probabilities than the signal, then we are more confident that the selected signal region is different than the rest of the mass distribution.

Chapter 4

Results

This chapter will show the results from real and embedded (simulated) data. The definitions and procedures used here were described in the last chapter.

4.1 Λ_c Sample

Figure 4.1a shows the mass plot for the Λ_c data sample, with a requirement the $L/\sigma > 8$. The bottom plot in that figure has the additional cuts that pointback < 1200, and scut(2) > 4. We enhance the signal-to-background ratio by a factor of 3. The candidates that pass the additional cuts will be referred to as the "clean Λ_c sample". Table 4.1 shows the results of the fits to the Λ_c sample.

Number of Events	Loose cuts	Tight cuts	Efficiency
signal (from gaussian fit)	2155	1656	77 %
background	5486	1340	24 %

Table 4.1: Λ_c yields for real data, before and after tight cuts. The fit was a gaussian for the signal plus a linear background. Background is the number of events in the mass plot, minus the signal size. Efficiency is the ratio of events after and before the cuts are applied.

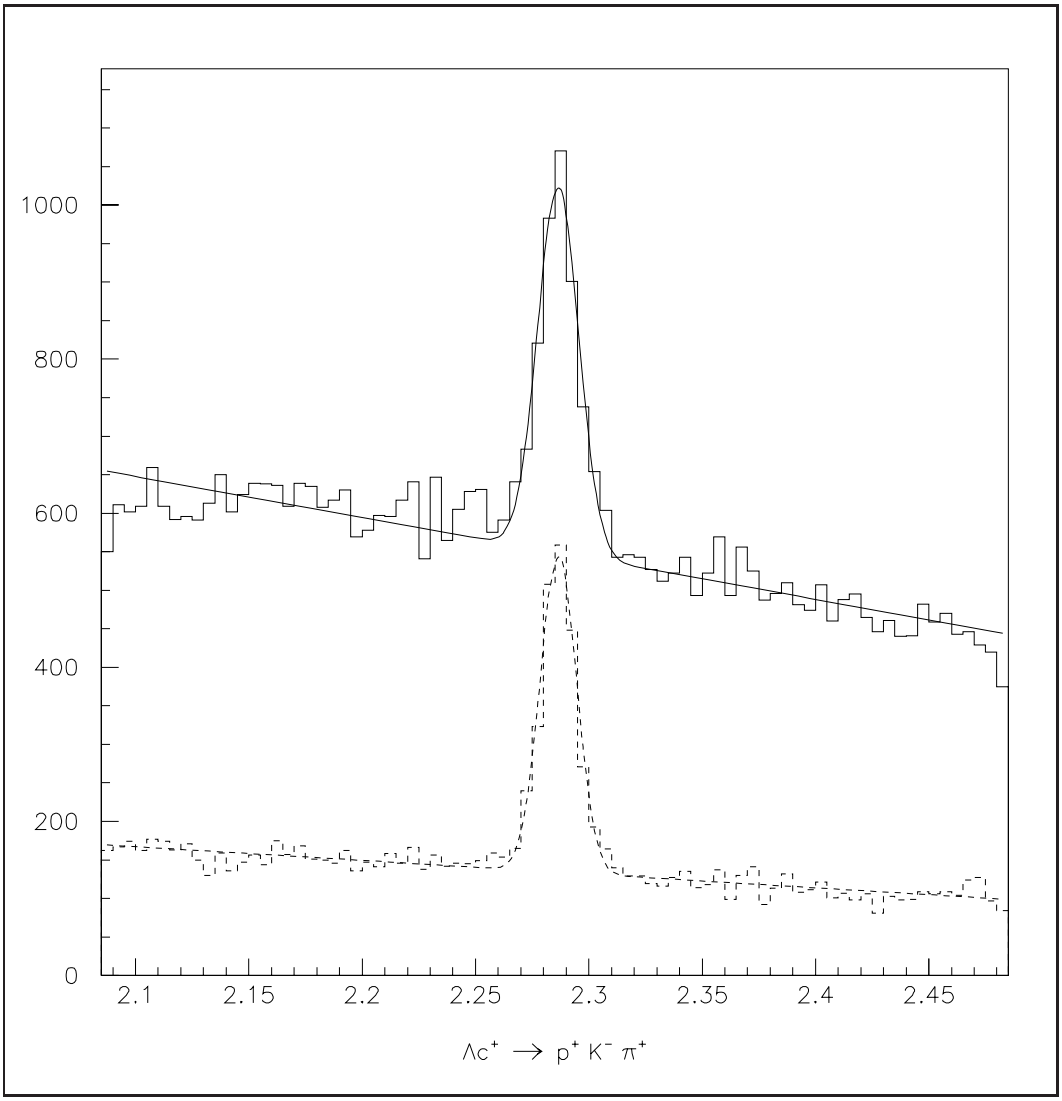

Figure 4.1: $\Lambda_c^+ \to p^+K^-\pi^+$ reconstruction mass plots for real data. Mass is in GeV/c^2. Solid plot is the reconstruction output, dashed plot is the clean sample after cuts are applied.

4.2 Ξ_{cc} candidate sample

The preliminary search sample will be shown to provide a reason for continued analysis. The raw Ξ_{cc} candidates were generated. The minimum bias cuts described in the last chapter are applied. The results are shown in figure 4.2 There are an excess of events below 3.8 GeV. To get a rough count of the events, there are 64 candidates between 3.73 - 3.79 GeV. With 44 candidates in each of the windows 3.64 - 3.70 GeV and 3.82 - 3.88 GeV, we have about 20 signal events.

We also tried $\Lambda_c K\pi\pi$ reconstructions with different charges for the tracks. This will produce our "wrong-sign" sample. If we get enhancements in reconstructions which should not have signal, we will suspect a systematic bias. This also tests if our current signal might be a mass reflection from another state, due to assigning the wrong masses to the $K\pi\pi$ tracks. The background fluctuations in figure 4.3 and figure 4.4 could mask small signals, but there do not appear to be any multiple-bin enhancements for the "wrong-sign" reconstructions. With background, we can expect a statistical variation in the number of events for a particular mass bin. The "wrong-sign" plots show some single bins with large counts. These are assumed to be background, since their fit widths would be much smaller than the detector mass resolution for this reconstruction.

4.3 Embedding

The simulation used the Ξ_{cc} and Λ_c embedded files described in the last chapter. The Ξ_{cc} file will provide the behavior of the particles we are looking for. It will also provide information about background from events with a real candidate, presumably from mistracking, or replacing one of the $K\pi\pi$ embedded tracks with an uncorrelated track from the underlying event. The Λ_c embedded events will simulate background events where we have a real Λ_c that was not made by a doubly charmed baryon, which combined with random real kaon and pion tracks to form the $\Lambda_c K^-\pi + \pi^+$ reconstruction.

The Ξ_{cc} embedded file starts with 100K events. 28740 events are written to file, after the requirements: all tracks with momentum larger than 4 GeV/c, and that the Λ_c proton and kaon reach the M2 spectrometer (figure 4.5).

The same analysis steps (get a clean Λ_c sample, apply minimum bias

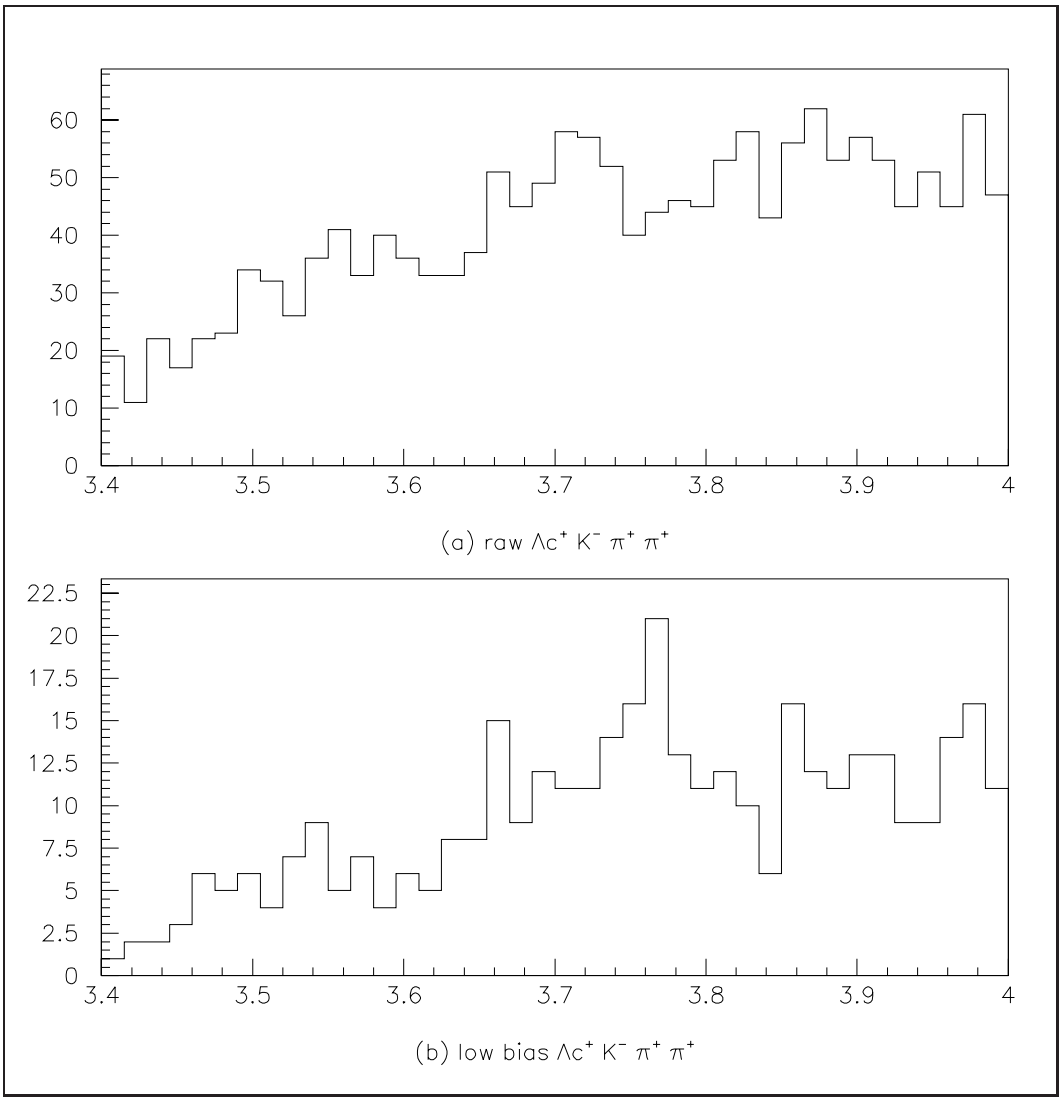

Figure 4.2: Ξ_{cc} candidate mass plots for real data. (a) Normal output (b) After applying minimum bias cuts.

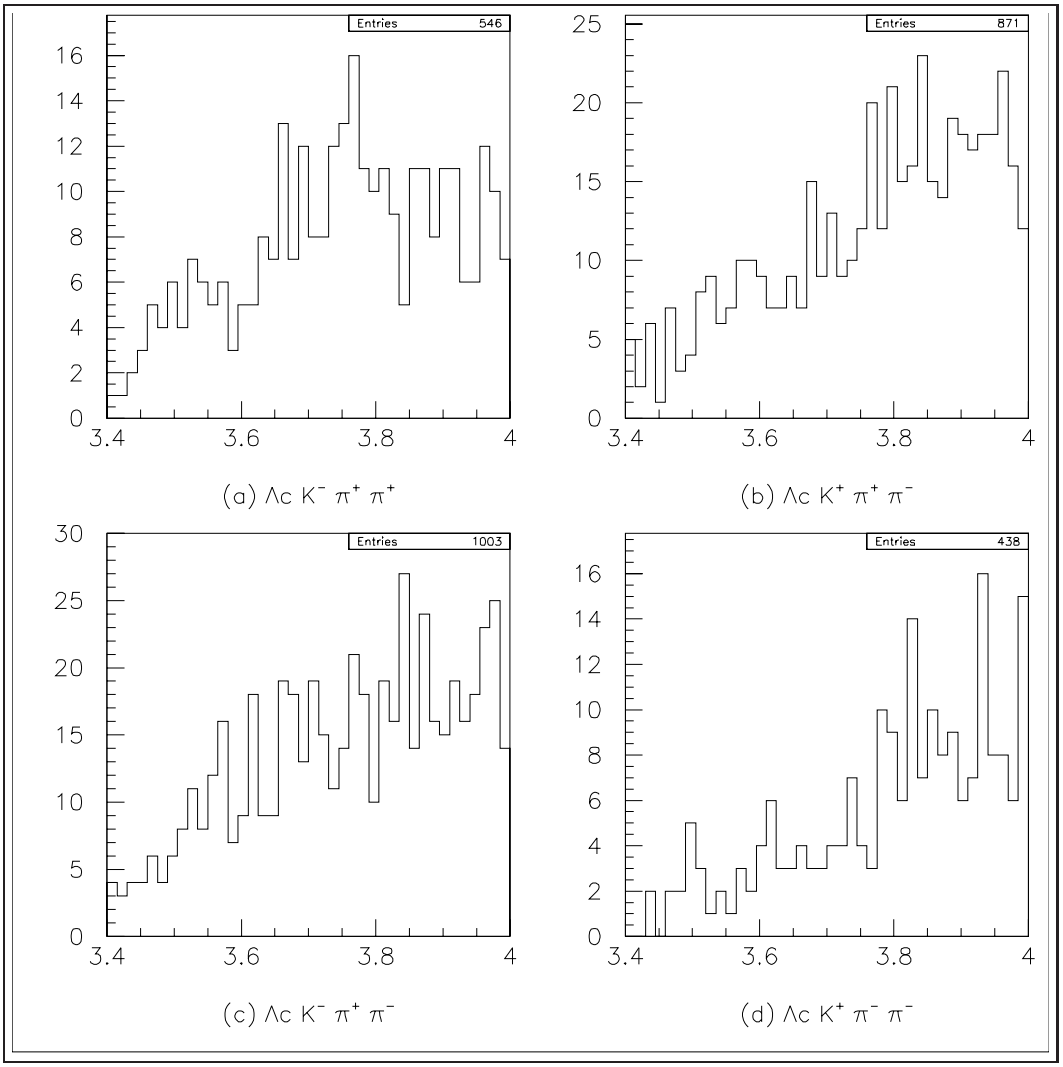

Figure 4.3: Mass plot for real data $\Lambda_c^+ K\pi\pi$ reconstructions, 20 MeV/c^2 bin width. Mass range is from 3.4 to 4.0 GeVc^2. The reconstructions are the same as our Ξ_{cc} candidates, except different charges are used for the $K\pi\pi$ tracks. Minimum bias cuts are applied. (a) $K^-\pi^+\pi^+$ (normal sample), (b) $K^+\pi^+\pi^-$, (c) $K^-\pi^+\pi^-$, (d) $K^+\pi^-\pi^-$. The requirement that the first pion has more momentum than the second pion is only applied when we have identical pions, (a) and (d).

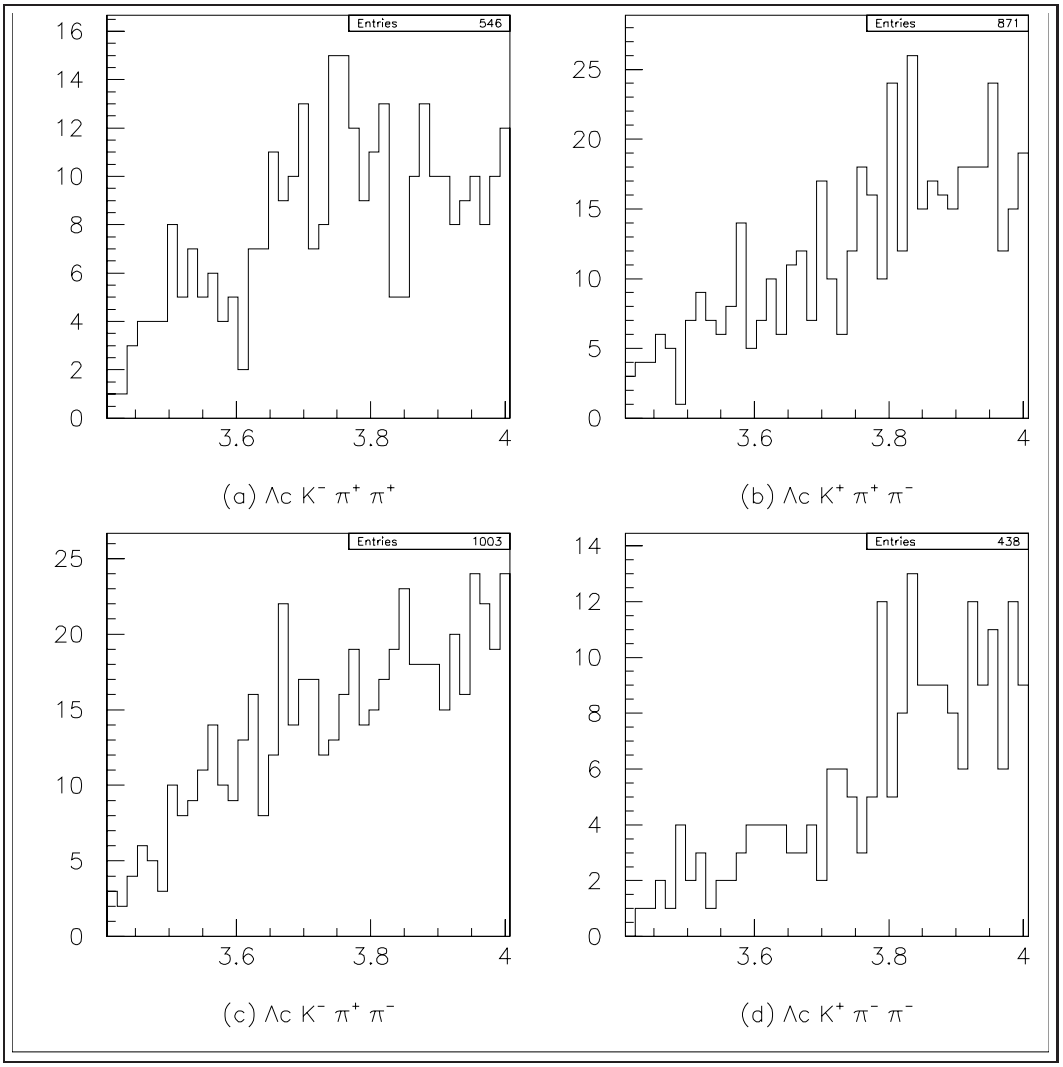

Figure 4.4: Mass plot for real data $\Lambda_c^+ K\pi\pi$ reconstructions, 20 MeV/c^2 bin width. Mass range is from 3.4075 to 4.0075 GeVc^2. The reconstructions are the same as our Ξ_{cc} candidates, except different charges are used for the $K\pi\pi$ tracks. Minimum bias cuts are applied. (a) $K^-\pi^+\pi^+$ (normal sample), (b) $K^+\pi^+\pi^-$, (c) $K^-\pi^+\pi^-$, (d) $K^+\pi^-\pi^-$. The requirement that the first pion has more momentum than the second pion is only applied when we have identical pions, (a) and (d).

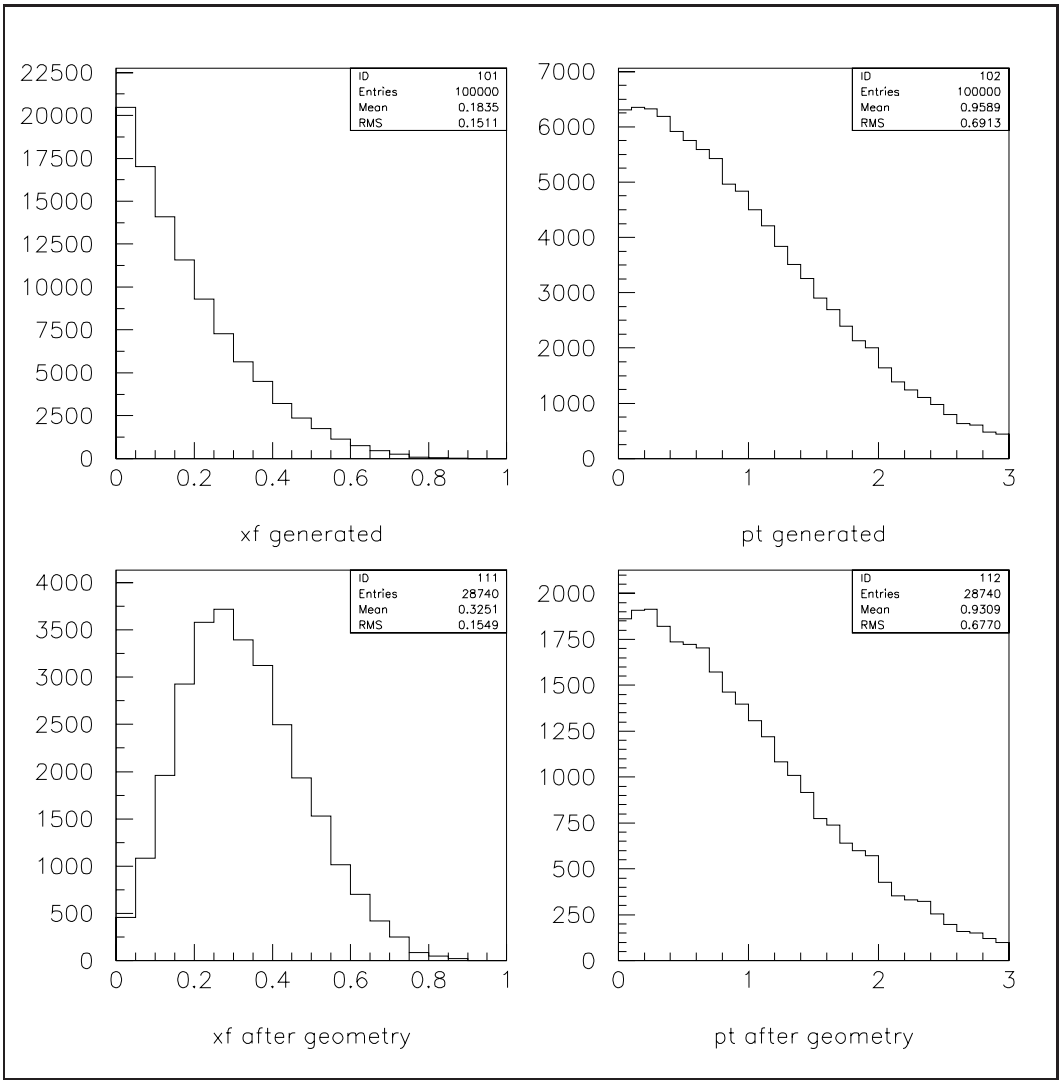

Figure 4.5: x_F and p_T distribution for simulated Ξ_{cc}. (a) x_F and (b) p_T are the generated values. (c) x_F and (d) p_T are after requiring that all tracks have momentum greater than 4 GeV/c, and that the Λ_c proton and kaon reach the M2 spectrometer.

cuts to Ξ_{cc} reconstruction) were applied to the embedded samples. We are starting from a clean Λ_c sample in the real data. Most of the Λ_c events in our data did not come from doubly-charmed baryons. The embedded Λ_c sample should only have Ξ_{cc} candidates by accident. The $K\pi\pi$ vertex is built from random tracks in the underlying event, which are not correlated with the embedded Λ_c. Figure 4.6 and table 4.2 suggests that the minimum bias cuts are doing a good job of reducing this type of background. The embedded Ξ_{cc} sample shows a clear peak in figure 4.7. The mass plot also has background, mostly due to a random track from the underlying event replacing a MC track, in the $K\pi\pi$ vertex. Table 4.3 shows that the cuts are not as efficient for removing this type of background. We also need to keep in mind that the clean Λ_c sample still has background along with the real charm events. How these events contribute background to the $\Lambda_c K\pi\pi$ mass plots is not easily simulated, so we will also need to look at the real data environment.

Number of Events	Normal output	Minimum bias cuts	Efficiency of cuts
Λ_c signal	5310	4630	87 %
Λ_c background	1148	718	63
Λ_c width in MeV	8.9	8.8	
Ξ_{cc} candidates	4042	340	8.4 %

Table 4.2: Yields from Λ_c-only embedded file. The signal count and width are from a gaussian fit. Background is the number of events in the plot, minus the signal count. The Ξ_{cc} count are for all events in the mass plot, which should be background.

The Ξ_{cc} embedded sample was fit again with the mass bins shifted by half a bin (5 MeV) to double check the fit values. The fit signal was the same as before, and the fit widths were 14.2 $\pm$ 0.7 and 14.8 $\pm$ 0.8 MeV for the Ξ_{cc}, for normal output and minimum bias cuts respectively.

The Ξ_{cc} width will be fixed at 15 MeV. Now a gaussian fit was done for the real data, using this fixed width, to get a mass for the peak. The results are shown in figures 4.8 and 4.9, with the results listed in table 4.4. The fits were done for mass bins shifted by a fraction of a bin width to account for any effects caused by binning. For the remainder of the studies, the mass is assumed to be 3.760 GeV, the average value in the table. Although the counts from the gaussian fits were listed in the table, that is just to verify

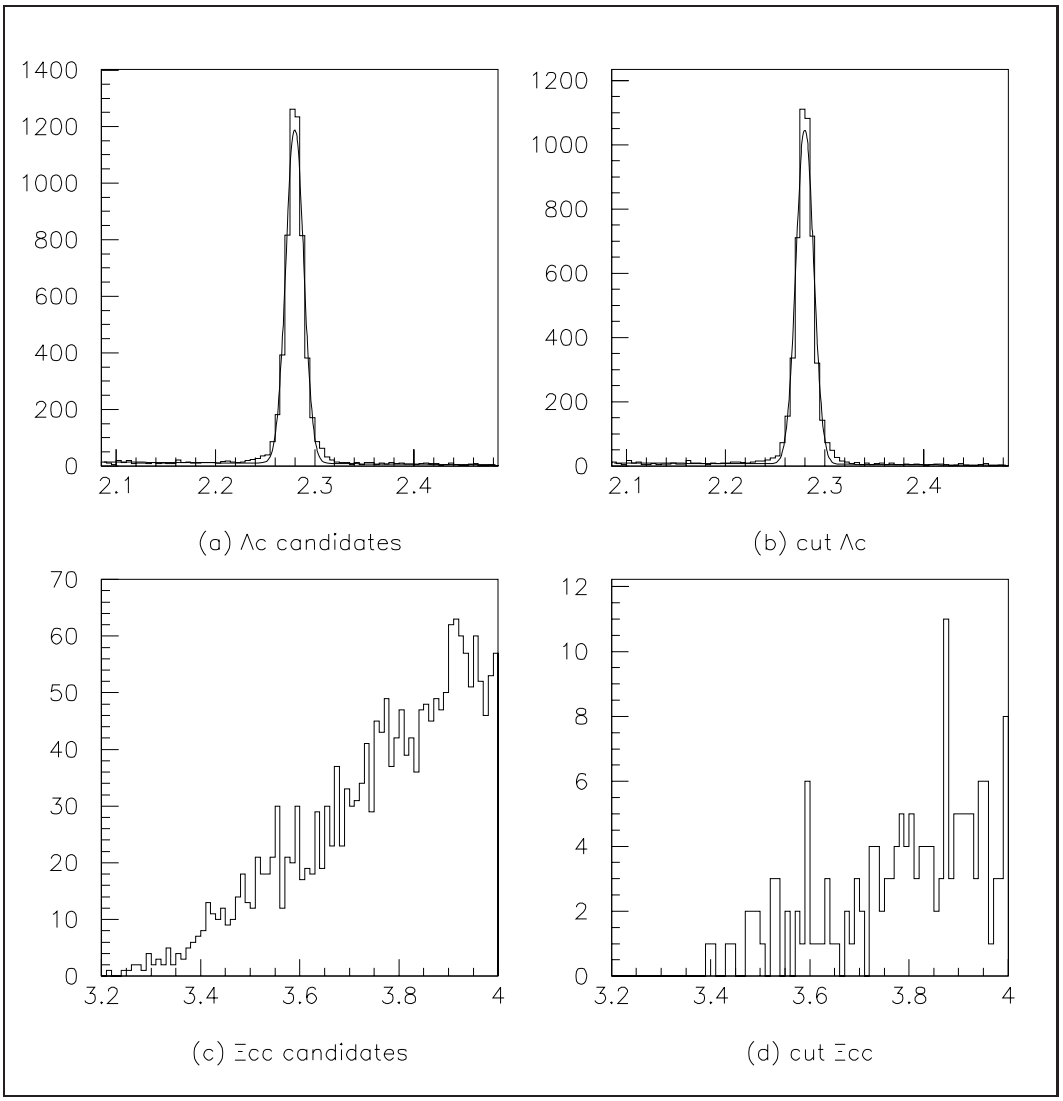

Figure 4.6: Mass plots using embedded Λ_c-only events. Results are based on the same analysis that was used for real data. Masses are in GeV/c^2. (a) Λ_c recon mass, normal output. (b) Λ_c recon mass with minimum bias cuts. (c) Ξ_{cc} recons, normal output. (d) Ξ_{cc} recon mass with minimum bias cuts. Since only the Λ_c was simulated, all entries in (c) and (d) are background.

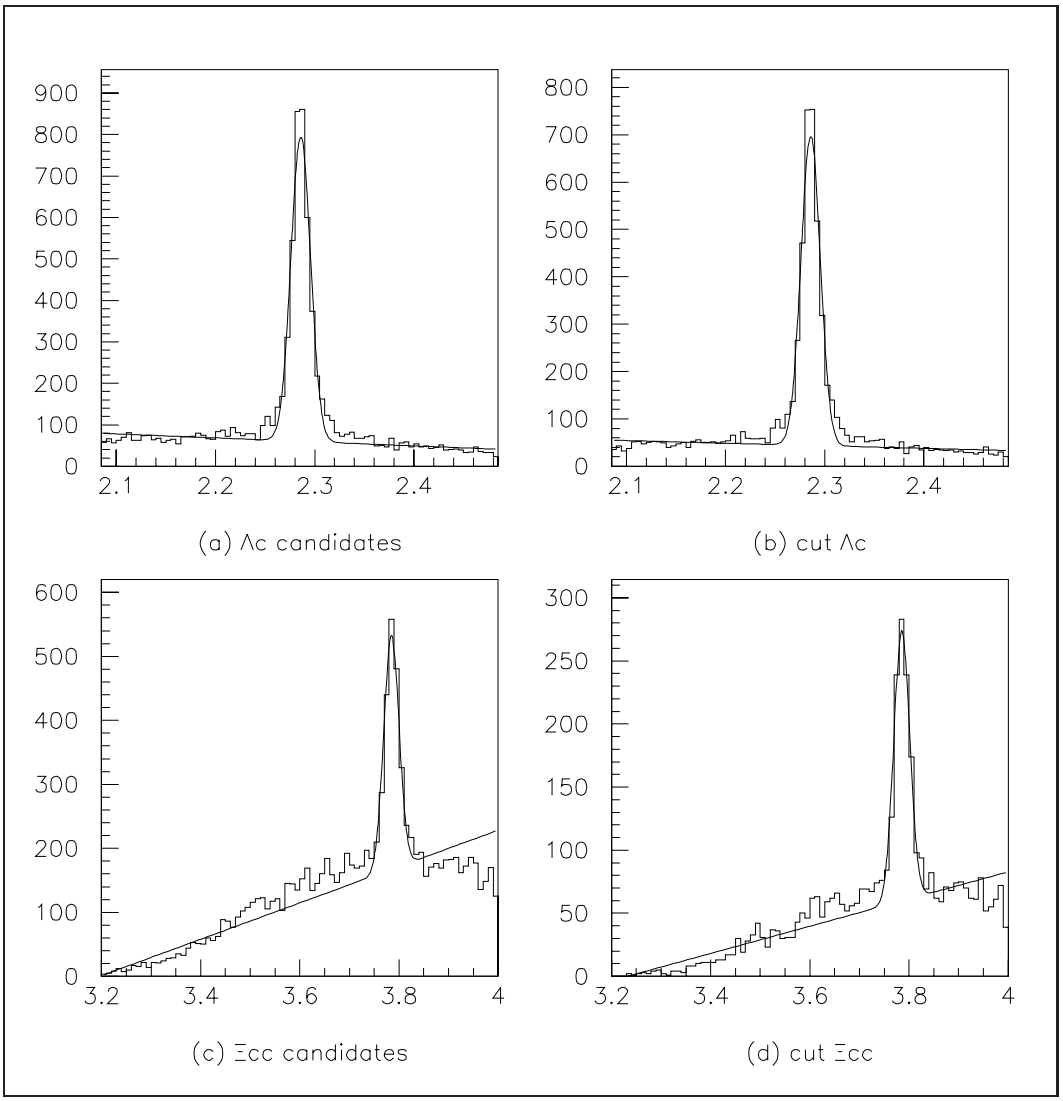

Figure 4.7: Mass plots using embedded Ξ_{cc} events. Results are based on the same analysis that was used for real data. Masses are in GeV/c^2. (a) Λ_c recon mass, normal output. (b) Λ_c recon mass with minimum bias cuts. (c) Ξ_{cc} recon mass, normal output. (c) Ξ recon mass with minimum bias cuts.

Number of Events	Normal output	Minimum bias cuts	Efficiency of cuts
Λ_c signal	3617	3178	88 %
Λ_c background	5867	3807	65 %
Λ_c width in MeV	9.8	9.7	
Ξ_{cc} signal	1297 $\pm$ 60	824 $\pm$ 40	64 %
Ξ_{cc} background	13048	4426	34 %
Ξ_{cc} width in MeV	14.2 $\pm$ 0.7	15.4 $\pm$ 0.9	

Table 4.3: Yields from Ξ_{cc} embedded file. The signal count and width are from a gaussian fit for the signal and a linear fit for the background. Background is the number of events in the plot, minus the signal count. Efficiency is the ratio of events after and before the minimum bias cuts.

that the PAW fit was behaving as expected. For the most part we will be using sideband subtraction, since the background level is uncertain.

Bin size	Bin shift	Mass of peak	Size of fit
15 MeV	0 MeV	3761 $\pm$ 8.4 MeV	19.4 $\pm$ 7.6 MeV
15	+5	3757 $\pm$ 5.6	17.8 $\pm$ 8.6
15	+10	3760 $\pm$ 4.5	18.1 $\pm$ 7.4
20 MeV	0 MeV	3762 $\pm$ 7.7	19.3 $\pm$ 7.5
20	+5	3768 $\pm$ 9.8	17.1 $\pm$ 7.4
20	+10	3755 $\pm$ 8.5	17.2 $\pm$ 7.2
20	+15	3756 $\pm$ 3.7	21.2 $\pm$ 7.9

Table 4.4: Mass peak fits for real data. The +0 mass range is from 3.4 to 4.0 GeV. The other mass ranges are moved by the listed shift, to account for binning effects. The fit is a gaussian plus a linear background. The sizes of the fit signal are listed to verify that fit results are reasonable.

Using the value of 3.760 GeV/c^2 as the central value for the signal, we made some gaussian fits with the width floated (figure 4.10). The fit width and number of events have large uncertainties. The binning and shape of the background changes the fit values, although the differences are within the errors. Unless we find selection cuts that reduce and smooth the background, the best strategy is to continue using the fixed with of 15 MeV/c^2 that we

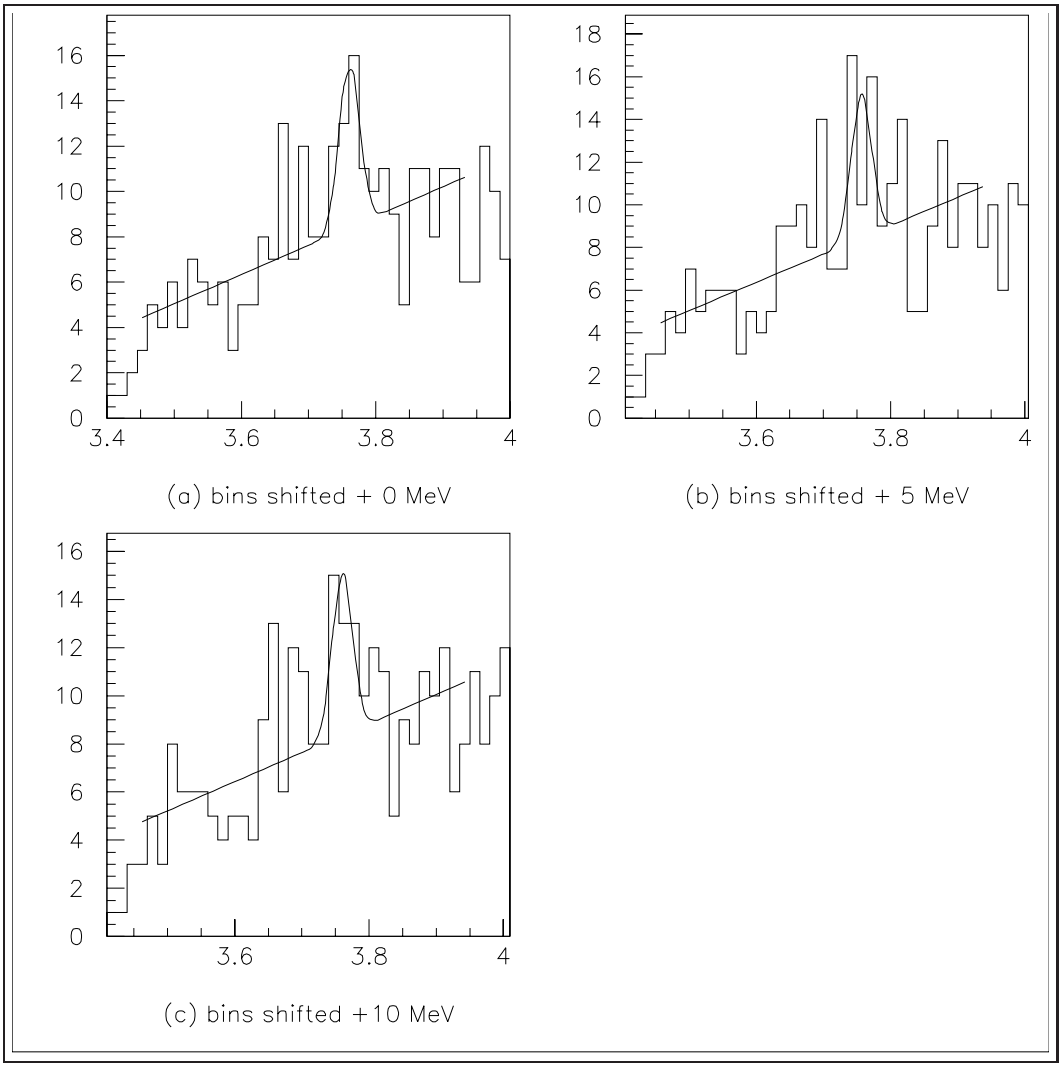

Figure 4.8: Real data $\Lambda_c^+ K^- \pi^+ \pi^+$ mass plot, 15 MeV bin width. Fit is a gaussian of fixed width 15 MeV, plus a linear background.

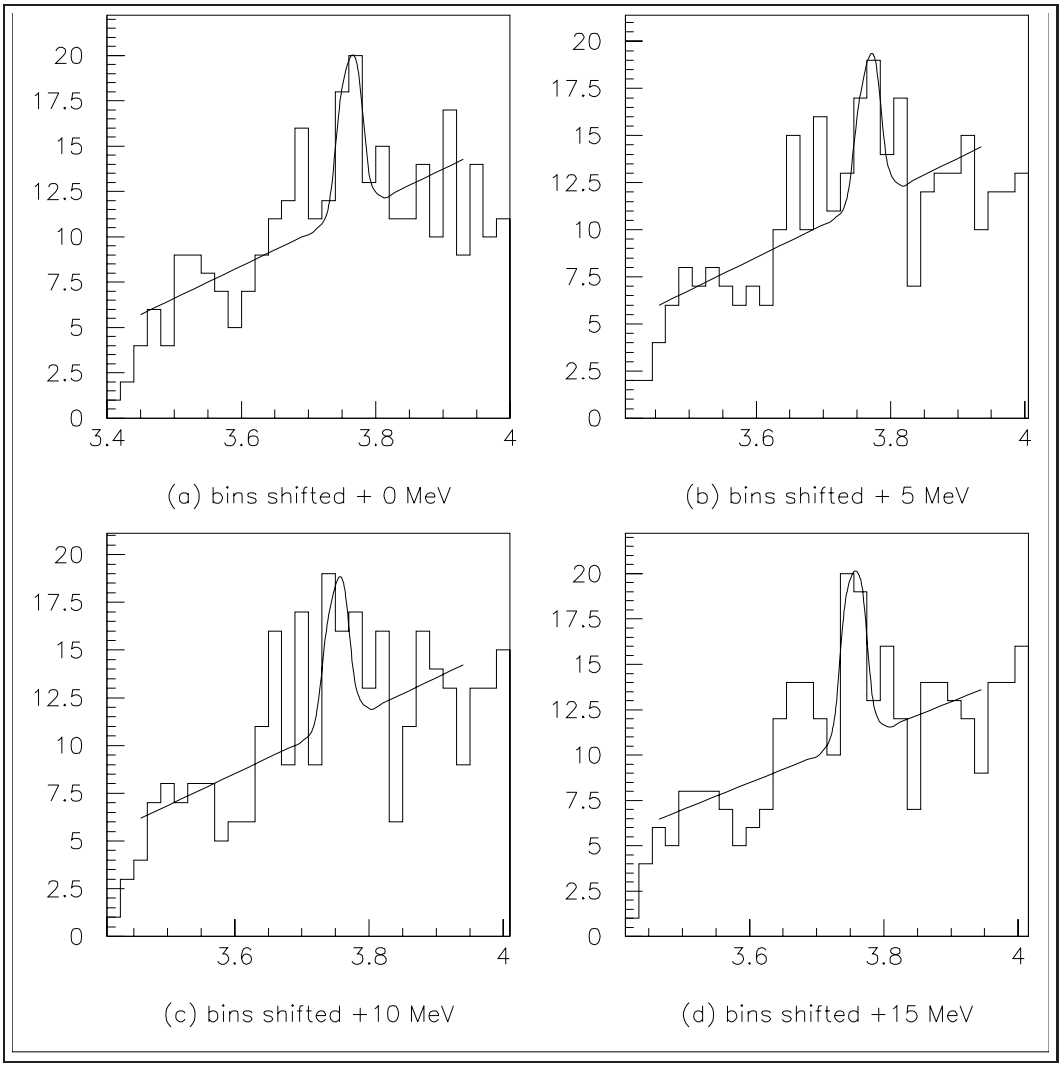

Figure 4.9: Real data $\Lambda_c^+ K^- \pi^+ \pi^+$ mass plot, 20 MeV bin width. Fit is a gaussian of fixed width 15 MeV, plus a linear background.

obtained from embedding simulation.

4.4 Embedded kinematic variables

The current sample uses only basic cuts. The next step is to look for further selection cuts that have reasonable efficiency for signal and high rejection for background. Any applied cuts must show signal efficiency for the embedded Ξ_{cc} sample, and background rejection in either real sideband, Ξ_{cc} embedded sideband, or in the embedded Λ_c sample. There is a real temptation to use real data signal when deciding on cuts, but any results may be a consequence of kinematic enhancement (bias) rather than an improvement in signal/background rejection.

Eighteen variables were checked for the embedded Λ_c sample (Figures C.1 - C.6), the embedded Ξ_{cc} sample (Figures C.7 - C.12), and for the real data sample (Figures C.13 - C.18). Those figures are in Appendix C. There does not appear to appear to be any significant difference between the plots, so any cuts on these quantities will not help our signal. As mentioned before, we are looking at the Λ_c, Ξ_{cc} sidebands, and real sidebands to see the background behavior. The Ξ_{cc} sideband-subtracted signal will simulate the desired events. We might expect to see differences involving the kaon or pion tracks in the $K\pi\pi$ vertex, as we are examining three different groups: "signal" embedded tracks from the Ξ_{cc}, random real tracks uncorrelated with the embedded Λ_c, and tracks from real data. The source of the background might have been concentrated in a different region of phase space than signal. The different samples look very similar, and are presented only to show that they were examined.

4.5 Sideband and signal differences

A general survey of embedded data failed to reveal any further selection that could be done to improve the signal. We can still compare real data sidebands to sideband-subtracted signal. Any variations in the data could provide clues into which processes are involved in creating the candidates. For this search sample, we found differences between signal and sideband, but have not yet been able to come up with an physics explanation.

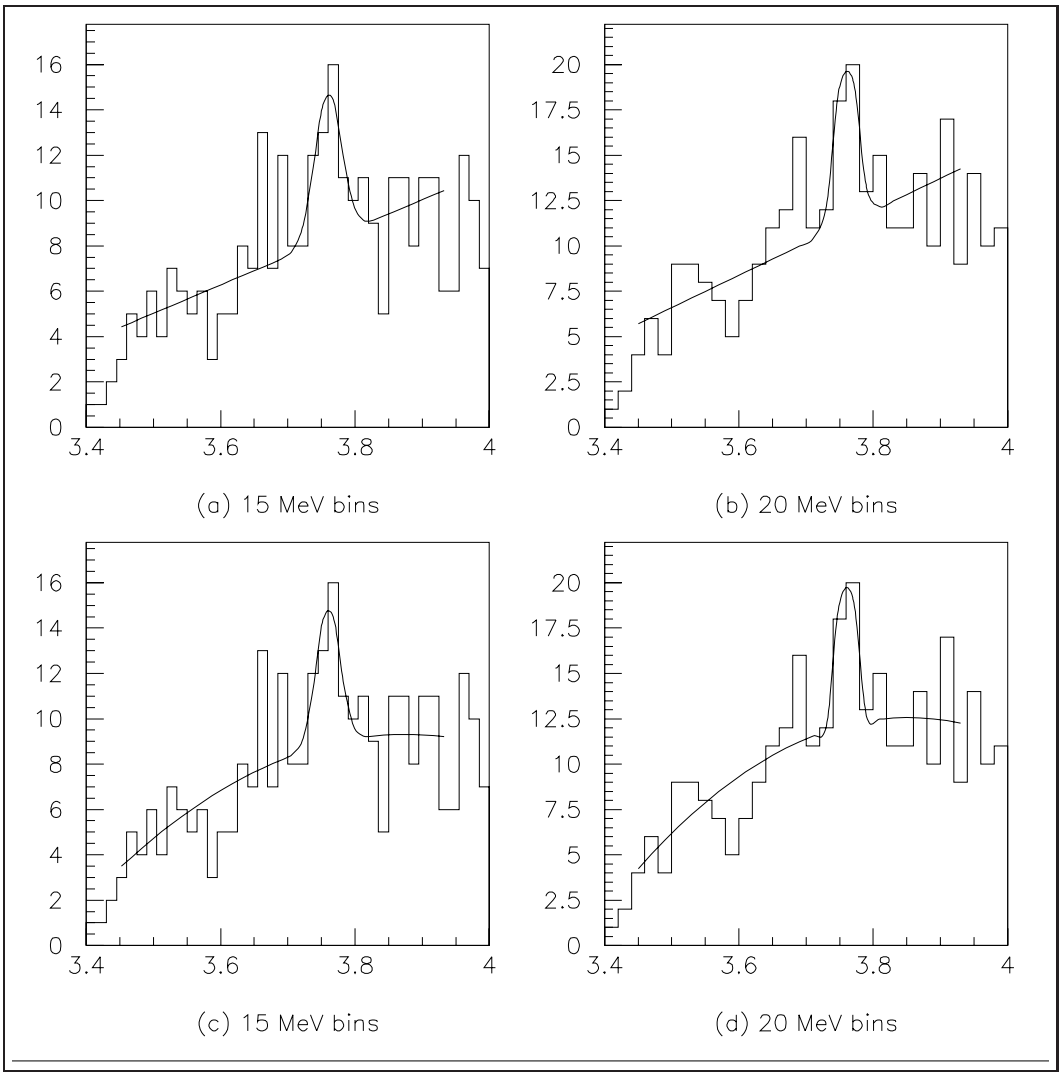

Figure 4.10: Fits for the gaussian width of real data $\Lambda_c^+ K^- \pi^+ \pi^+$ mass plot. The central value was fixed at 3.760 GeV/c^2, the mass range for all plots is from 3.4 - 4.0 GeV/c^2. The fit was a gaussian for the mass peak, and either a linear or quadratic fit for the background. (a) 15 MeV/c^2 bin width, linear background. Signal size 22.4 $\pm$ 9.3 events, width 19.4 $\pm$ 6.5 MeV/c^2. (b) 20 MeV/c^2 bin width, linear background. Signal size 16.7 $\pm$ 8.6 events, width 14.0 $\pm$ 10.4 MeV/c^2. (c) 15 MeV/c^2 bin width, quadratic background. Signal size 19.3 $\pm$ 8.9 events, width 17.5 $\pm$ 8.2 MeV/c^2. (d) 20 MeV/c^2 bin width, quadratic background. Signal size 16.8 $\pm$ 8.7 events, width 14.0 $\pm$ 9.6 MeV/c^2.

4.5.1 Lifetime

Figure 4.11 show lifetime plots for data and the two embedded files. The proper lifetime is based on the distance the particle travels before decaying, the time of flight is then boosted to the rest frame of the Ξ_{cc} candidate. The distance in the lab frame is from the $K\pi\pi$ vertex to the primary vertex, reduced by one σ_z to account for our cuts. The events are not corrected for acceptances or systematics. The fits are very poor; the choice was between having few enough time bins for a good PAW fit, or having more time bins to get an idea of the distribution. The fit results should not be taken literally, only as a guide. The limited statistics for real data signal make it difficult to tell if its lifetime is shorter or longer than background, for real data or the simulated background present in the Λ_c embedded file. The real data clearly has a shorter lifetime than the simulated lifetime of 0.103 psec for the embedded Ξ_{cc}.

4.5.2 Beam particle

We take a look at the beam particle for the events were we see charm. Table 4.5 shows the results for sideband subtracted Λ_c, and table 4.6 has Ξ_{cc} candidates. The production by beam type appears the same for Λ_c and for the Ξ_{cc} candidates. We do not have any sbs Ξ_{cc} candidates produced by pions, but that is not unreasonable given the low statistics.

Beam particle	Signal + sideband	sideband	sbs
positive beam			
pion	21	9	12
proton	396	154	242
unassigned	27	8	19
negative beam			
pion	193	54	139
sigma	1947	815	1132
unassigned	123	34	89

Table 4.5: Beam particle for real data Λ_c, based on BTRD information. The signal window are candidate mass within 20 MeV/c^2 of the Λ_c mass at 2.285 GeV/c^2. The sidebands are candidates between 40 and 60 MeV/c^2 away.

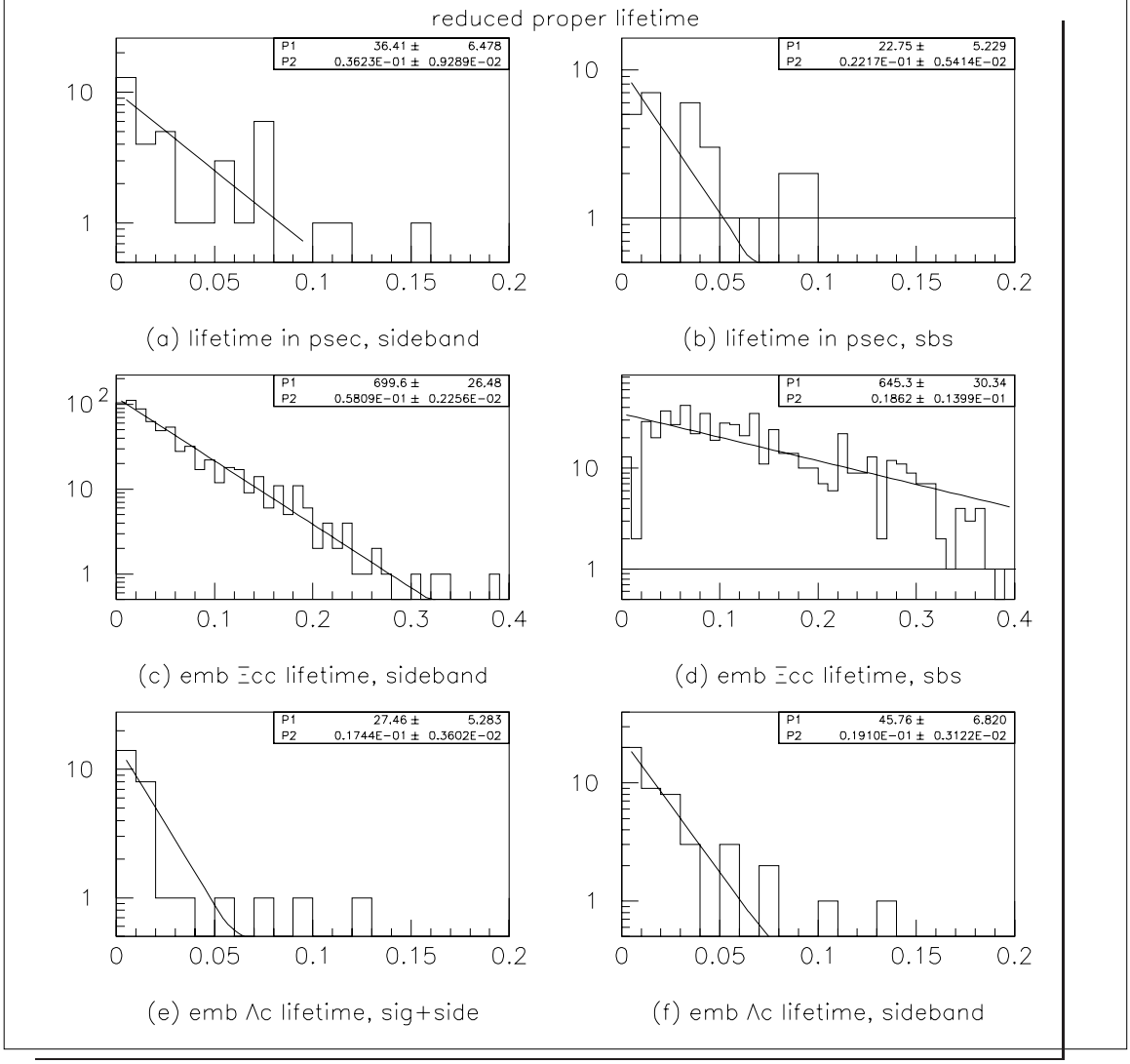

Figure 4.11: Uncorrected reduced proper lifetimes for $\Lambda_c^+ K^- \pi^+ \pi^+$. For all plots, time are in picoseconds, and the vertical axis is the number of events per time bin on a logarithmic scale. The fit is from PAW for the number of events (P1) and the lifetime (slope of the line, P2). (a) Data sidebands. (b) Data sideband subtracted signal. (c) Embedded Ξ_{cc} sidebands. (d) Embedded Ξ_{cc} sbs signal. (c) Embedded Λ_c, signal region of mass plot. (d) Embedded Λ_c, sideband region of mass plot.

Beam particle	Signal + sideband	sideband	sbs
positive beam			
pion	0	0	0
proton	10	5	5
unassigned	1	0	1
negative beam			
pion	2	2	0
sigma	42	29	13
unassigned	0	1	-1

Table 4.6: Beam particle for real data Ξ_{cc} candidates, based on BTRD information. The signal window are candidate mass within 37.5 MeV/c^2 of the mass at 3.760 GeV/c^2. The sidebands are candidates between 52.5 and 90 MeV/c^2 away.

4.5.3 Center of mass reference frame

The momentum vectors for the Λ_c, K, and both πs were boosted to the rest frame for the Ξ_{cc} candidate. The angles formed by the momentum vectors were plotted. In this example, the K was compared to both πs, and the smaller cosine (larger angle) selected. The results for sideband and signal are shown in figure 4.12. The sideband subtracted signal shows a very different distribution than the sidebands. Since we do not understand the kinematics involved for this cut, we cannot apply it to the real data, but we present it as evidence that the signal-region events are of different character than the sideband background events.

We also looked at the difference in magnitude of the momentum of the $K\pi\pi$ vertex pions in the rest frame of the $\Lambda_c K\pi\pi$ reconstruction, $p(\pi 1) - p(\pi 2)$. Since we are ordering the pions such that the first pion has more momentum than the second pion in the lab frame, we might expect the distribution to be shifted towards a positive difference. Figure 4.13d shows the difference of the pion momentums for embedded Ξ_{cc} signal. The plot has a slight shift towards a positive difference. Before requiring the pion ordering, each candidate appeared twice in the plot, as $K\pi 1\pi 2$, and as $K\pi 2\pi 1$. That original embedding distribution was symmetric around zero. The other plots are for real data. The first thing that stands out is for candidates outside the normal signal mass window. There is a spike of candidates just less than

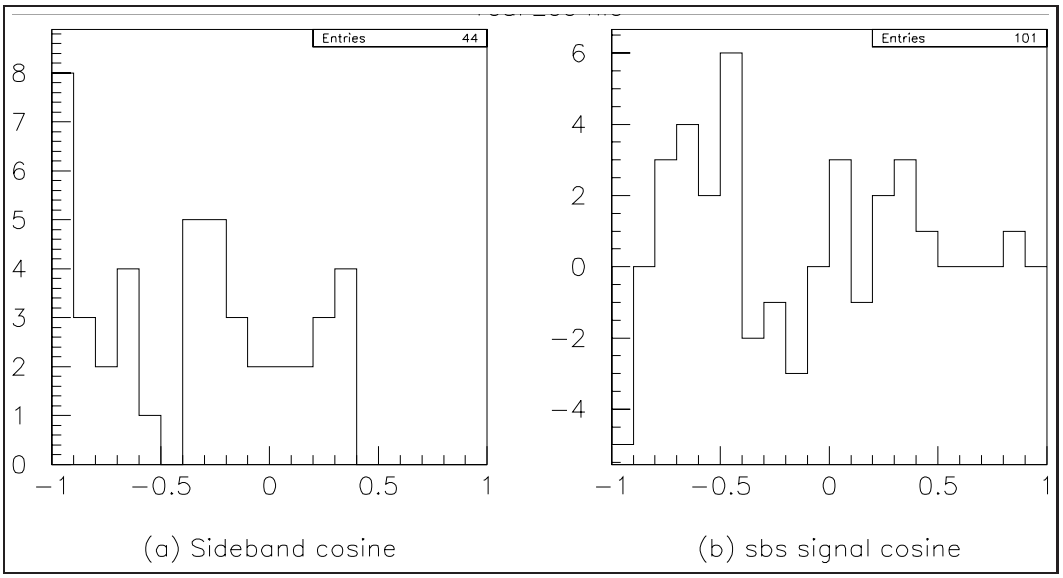

Figure 4.12: Smaller kaon-pion cosine, in the rest frame of the Ξ_{cc} candidate. Both pions are compared to the kaon, and the smaller cosine (larger angle) for the event is plotted. The cosine distributions are for sideband (a) and sideband subtracted signal (b), real data.

+0.2 GeV. The source of this is not known at the present. The second note is that the signal candidate distribution appears different the sidebands or embedding sample. This point is not obvious, given the limited statistics. To confirm this, the events were separated into positive and negative difference for pion momentum. The mass plots are in figure 4.14.

4.5.4 Submass plots

We are examining the Ξ_{cc} decay to four independent tracks (Λ_c, K, and two π). Another possibility is that the decay passes through resonances. A possible example would be $\Xi_{cc}^{++} \rightarrow \Sigma_c^{++} K^{0*}$, with $\Sigma_c^{++} \rightarrow \Lambda_c^+ \pi^+$ and $K^{0*} \rightarrow K^- \pi^+$. First we consider the known I = 1 charm baryons that decay to Λ_c by a single pion emission. We want to verify that these resonances are present in our data. The clean Λ_c^+ sample has a pion added to it, and the mass difference of the new reconstruction is plotted4.15. The narrow peak at Δ m of 167 MeV is the $\Sigma_c(2455)$, while the broad resonance at Δ m of 233 MeV is consistent with the $\Sigma_c(2520)$.

If the Ξ_{cc} prefers to decay through one of the resonances, we should see something in the sideband subtracted mass plots. We search the Ξ_{cc} sample, with minimum bias cuts, by taking the pions from the $K\pi\pi$ vertex and adding them to the Λ_c. The results are in figure 4.16. There is no way of knowing which pion is the "right" one to use for the combination, so both pions are tried. The pions were separated by lab frame momentum, with the higher momentum pion labeled "fast" and the lower momentum "slow". The plots do not show any particular enhancement for either Ξ_{cc} sidebands or signal.

The Ξ_{cc} sample, with minimum bias cuts, was also examined for $K\pi$ combinations from the $K\pi\pi$ vertex. The results are in figure 4.17. Again for convenience, the two pions were distinguished by their lab frame momentum. There appears to be a significant enhancement in the signal for the kaon and the slower pion for the signal region. We can notice the difference between signal and sideband. The resonance K^{0*} has a mass of 896 MeV, and a full width at half maximum of $\Gamma = 50$ MeV.[2] The plot of the $K\pi$ mass versus $\Lambda_c\pi$ mass, shown in figure 4.18, shows evidence consistent with the K^{0*}.

The embedded Ξ_{cc} data was used to make plots for $\Lambda_c\pi$ (figure 4.19) and for $K\pi$ (figure 4.20). The simulated sample does not have spin effects or resonances in the decay chain. Any enhancement in the plots are from phase-space effects or kinematic enhancements from the selection cuts.

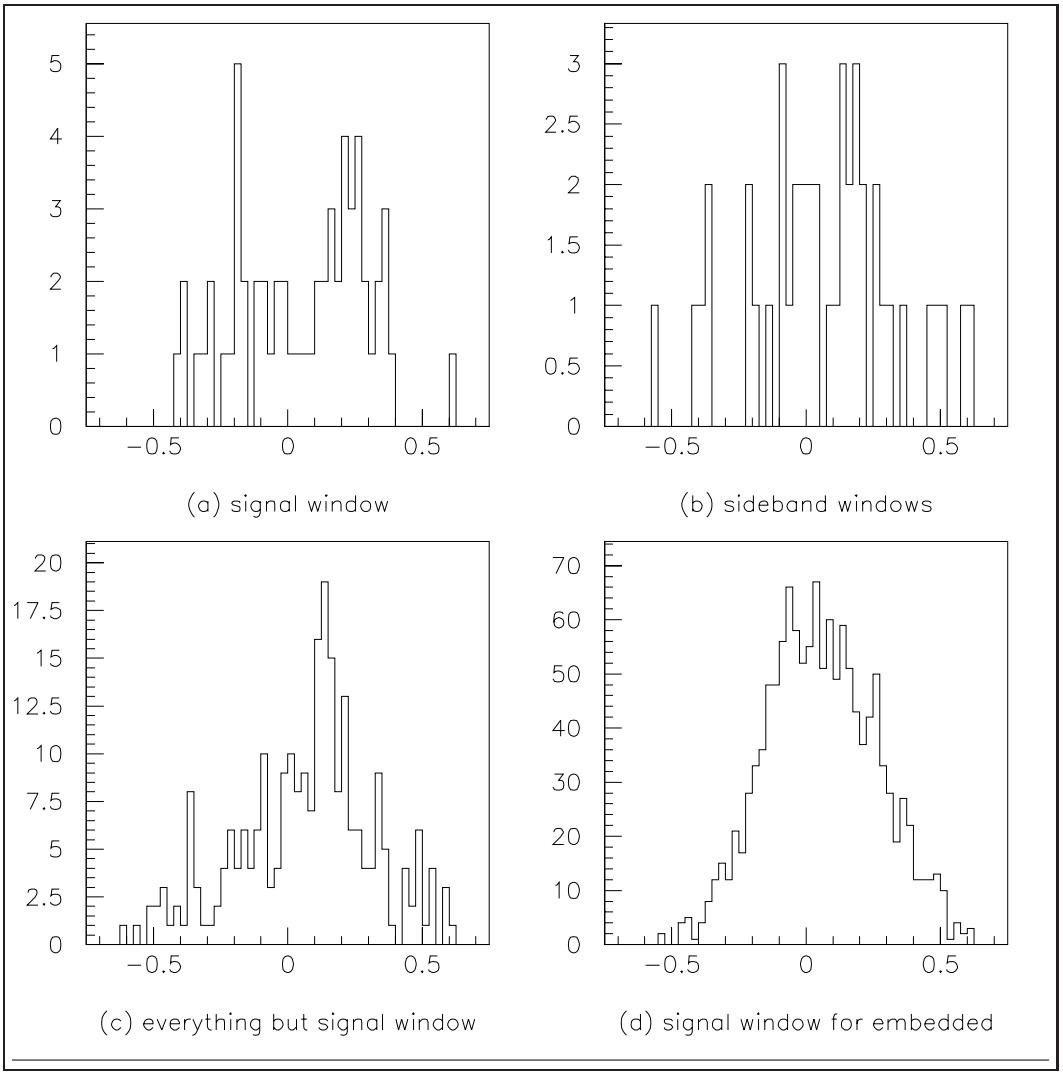

Figure 4.13: Difference in pion momentum in Ξ_{cc} rest frame, $p(\pi 1) - p(\pi 2)$. The pions are from the $K\pi\pi$ vertex. The first pion has more momentum compared to the second pion, in the lab frame of reference. The minimum bias cuts were applied. Horizontal axis is in GeV/c. (a) Candidates in the signal mass window, 3.760 GeV/$c^2\pm$ 37.5 MeV/c^2. (b) Sideband windows above and below the signal. (c) All candidates not in the signal mass window. (d) Embedded Ξ_{cc} signal.

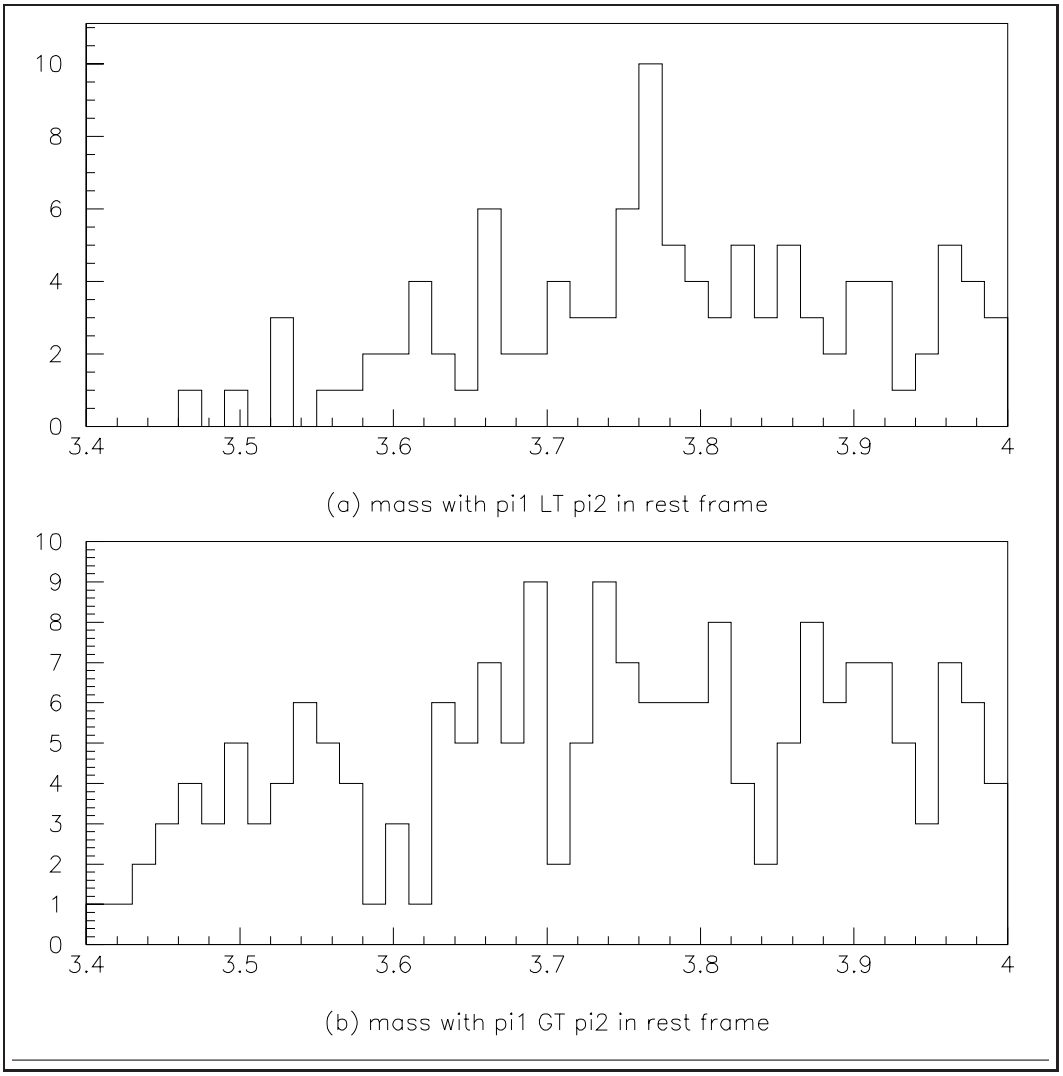

Figure 4.14: Mass plot for Ξ_{cc} candidates, separated by pion momentum in Ξ_{cc} rest frame. The pions are from the $K\pi\pi$ vertex. The first pion has more momentum compared to the second pion, in the lab frame of reference. The minimum bias cuts were applied. (a) Candidates with the second pion having more momentum in the rest frame. (b) Candidates with the first pion having more momentum in the rest frame.

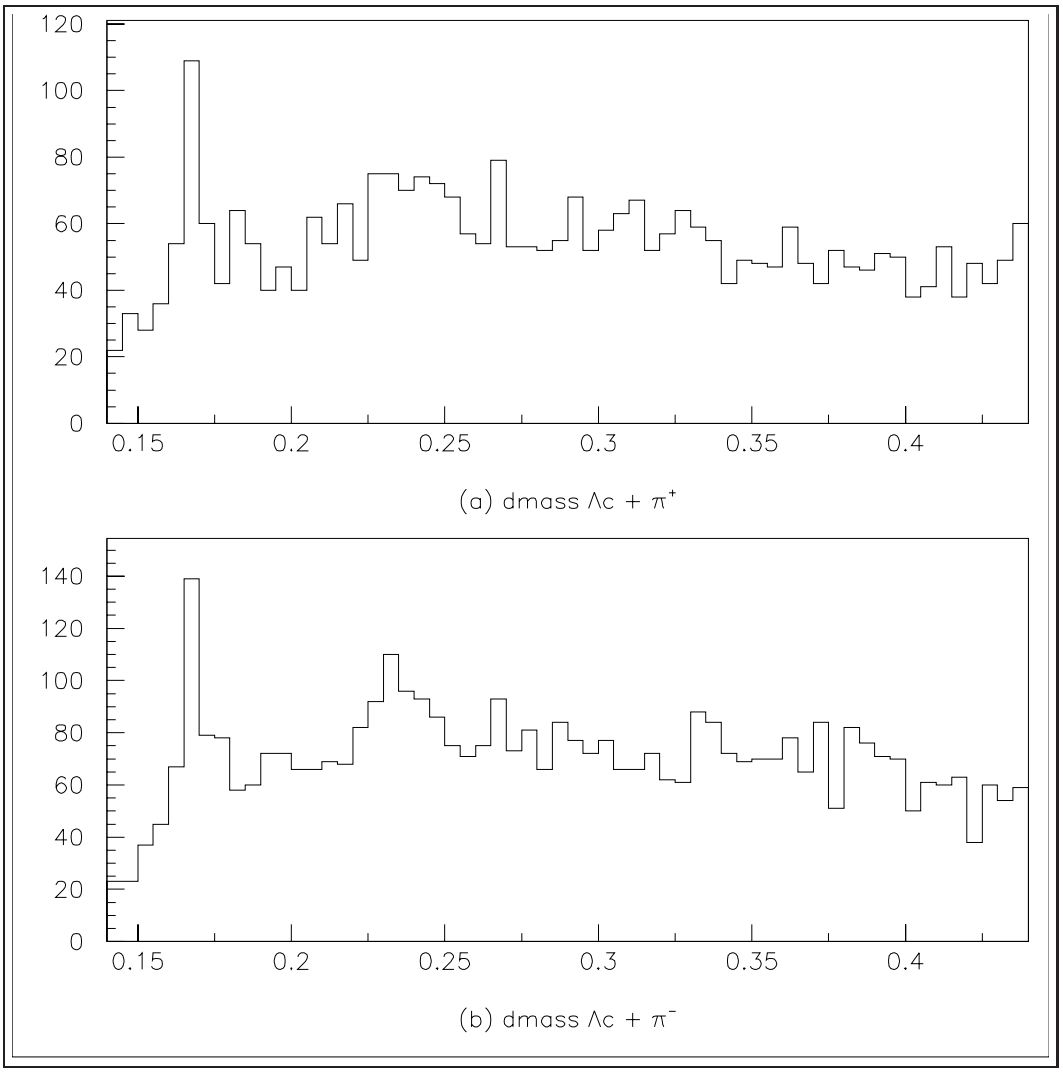

Figure 4.15: $\Lambda_c\pi$ - Λ_c mass difference. The clean Λ_c sample is combined with other pions in the event, to create the reconstruction. The mass difference is in GeV/c^2. (a) is with a π^+, (b) is with a π^- (b).

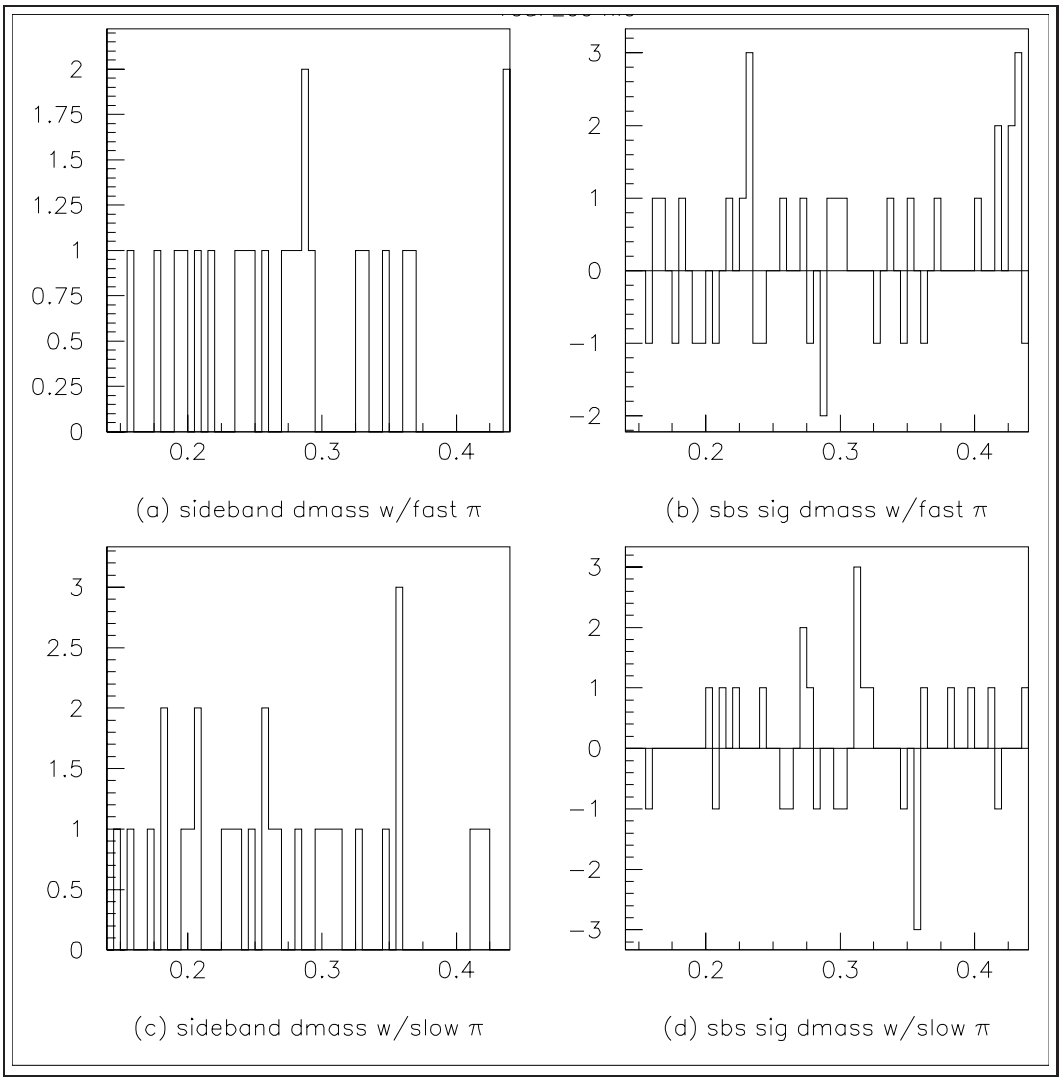

Figure 4.16: Real data $\Lambda_c^+\pi^+$ mass difference plot, 5 MeV/c^2 bin width, sideband and sideband-subtracted signal. Mass scale is in GeV/c^2. Events taken from the Ξ_{cc} candidates with minimum bias cuts applied. The mass difference is with respect to the Λ_c reconstruction. Fast and slow refer to the lab frame momentum of the two pions, compared to each other.

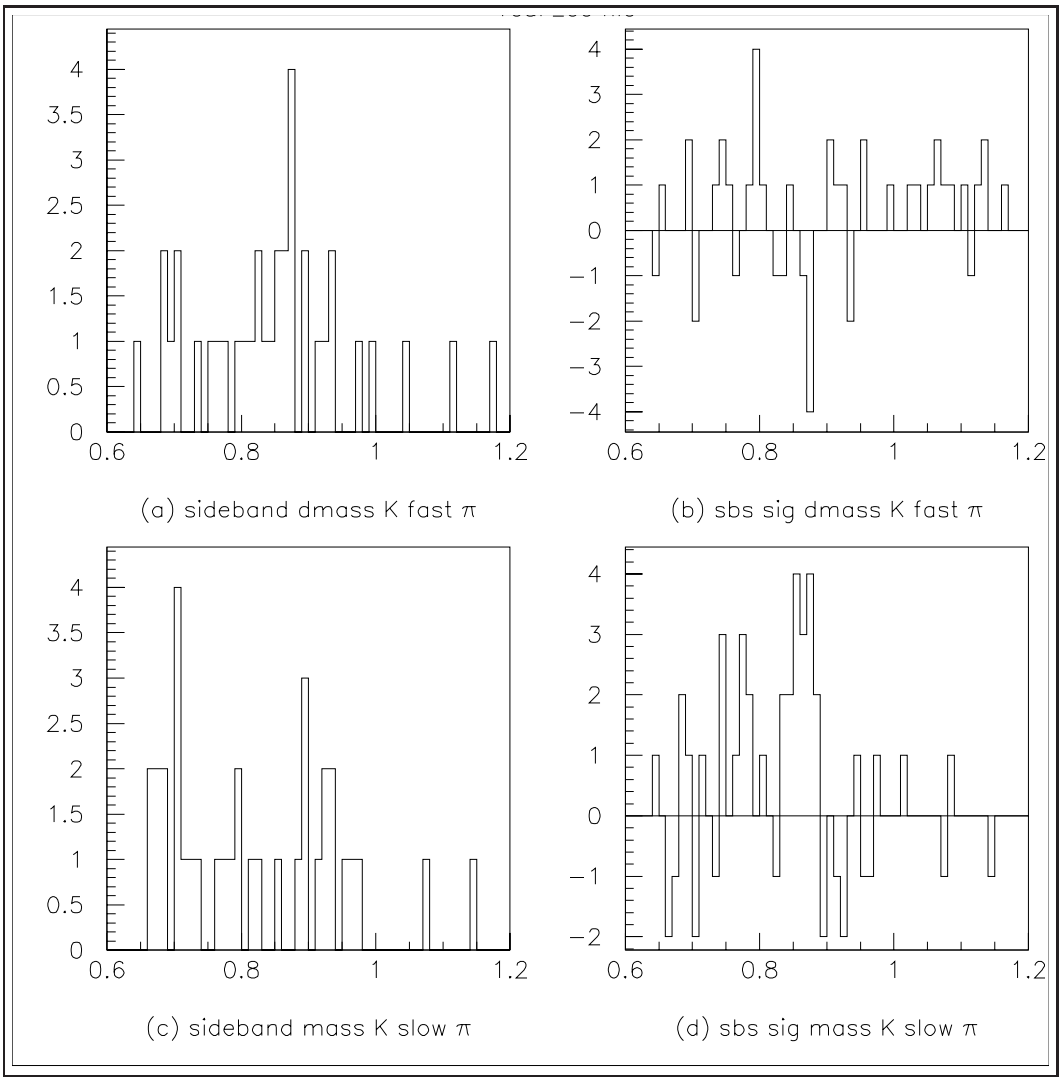

Figure 4.17: Real data $K^-\pi^+$ mass plot, 10 MeV/c^2 bin width, sideband and sideband-subtracted signal. Mass scale is in GeV/c^2. Events taken from the Ξ_{cc} candidates with minimum bias cuts applied. Fast and slow refer to the lab frame momentum of the pions, compared to each other.

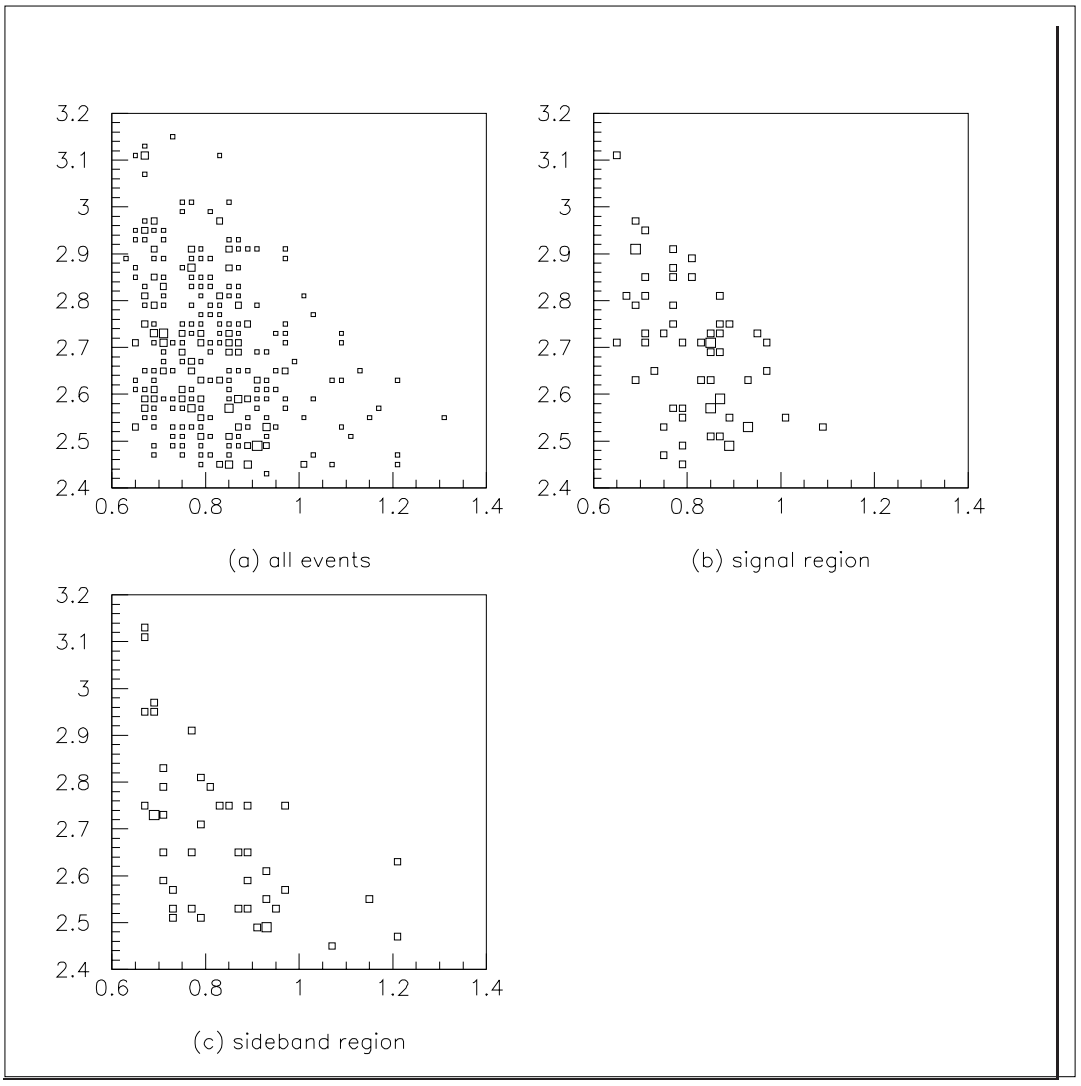

Figure 4.18: Submass plots for real data $\Lambda_c K\pi\pi$ candidates. Mass scales are in GeV/c^2. Vertical axis is the fast π-Λ_c combination, the horizontal axis is slow π-K combination. Fast and slow refer to the lab frame momentum of the pions, compared to each other. (a) All Ξ_{cc} candidates that pass the minimum bias cuts. (b) Signal region, 75 MeV window centered at 3.760 GeV. (c) Sideband windows.

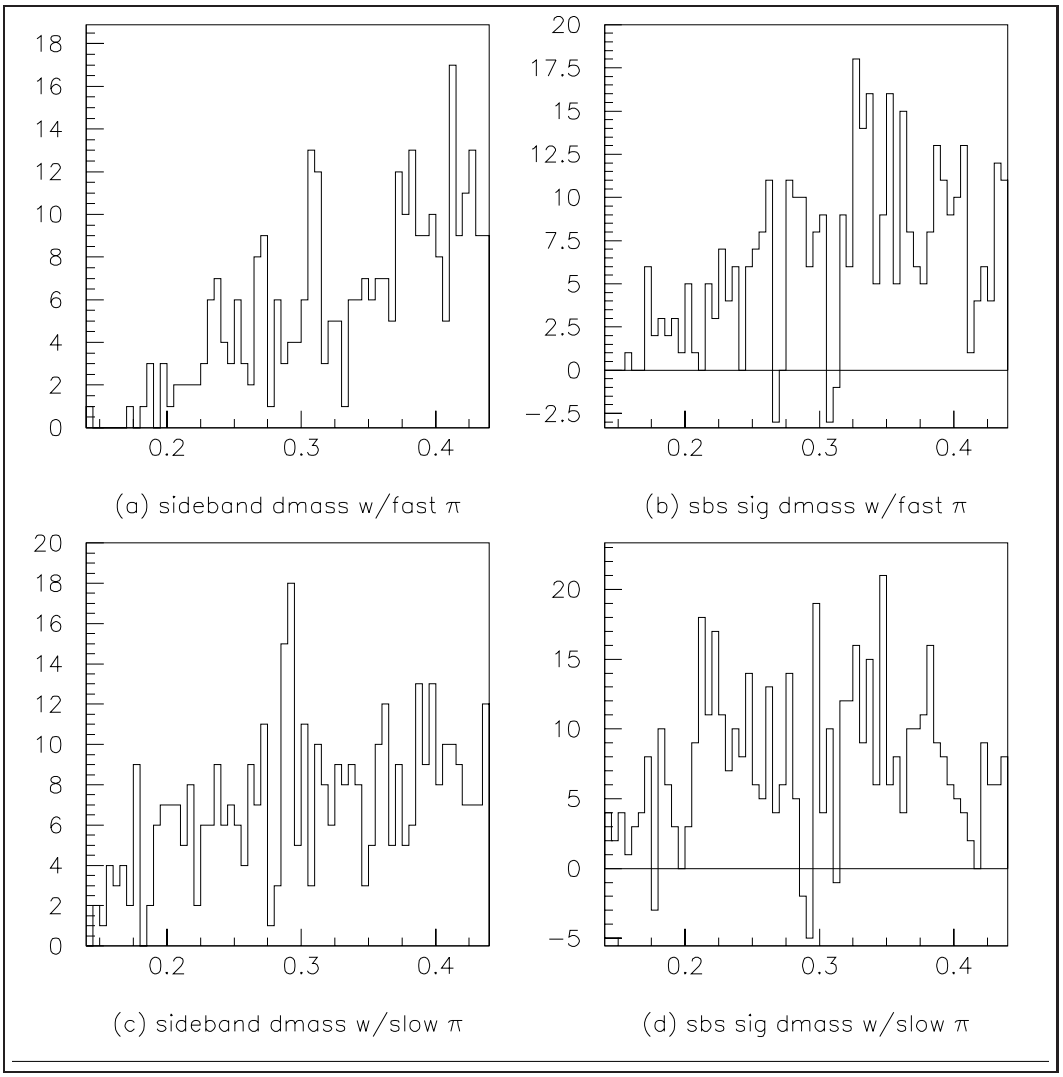

Figure 4.19: Embedded Ξ_{cc} file, $\Lambda_c^+\pi^+$ mass difference plot, 5 MeV/c^2 bin width, sideband and sideband-subtracted signal. Mass scale is in GeV/c^2. Events taken from the Ξ_{cc} reconstruction with minimum bias cuts applied. The mass difference is with respect to the Λ_c reconstruction. Fast and slow refer to the lab frame momentum of the two pions, compared to each other.

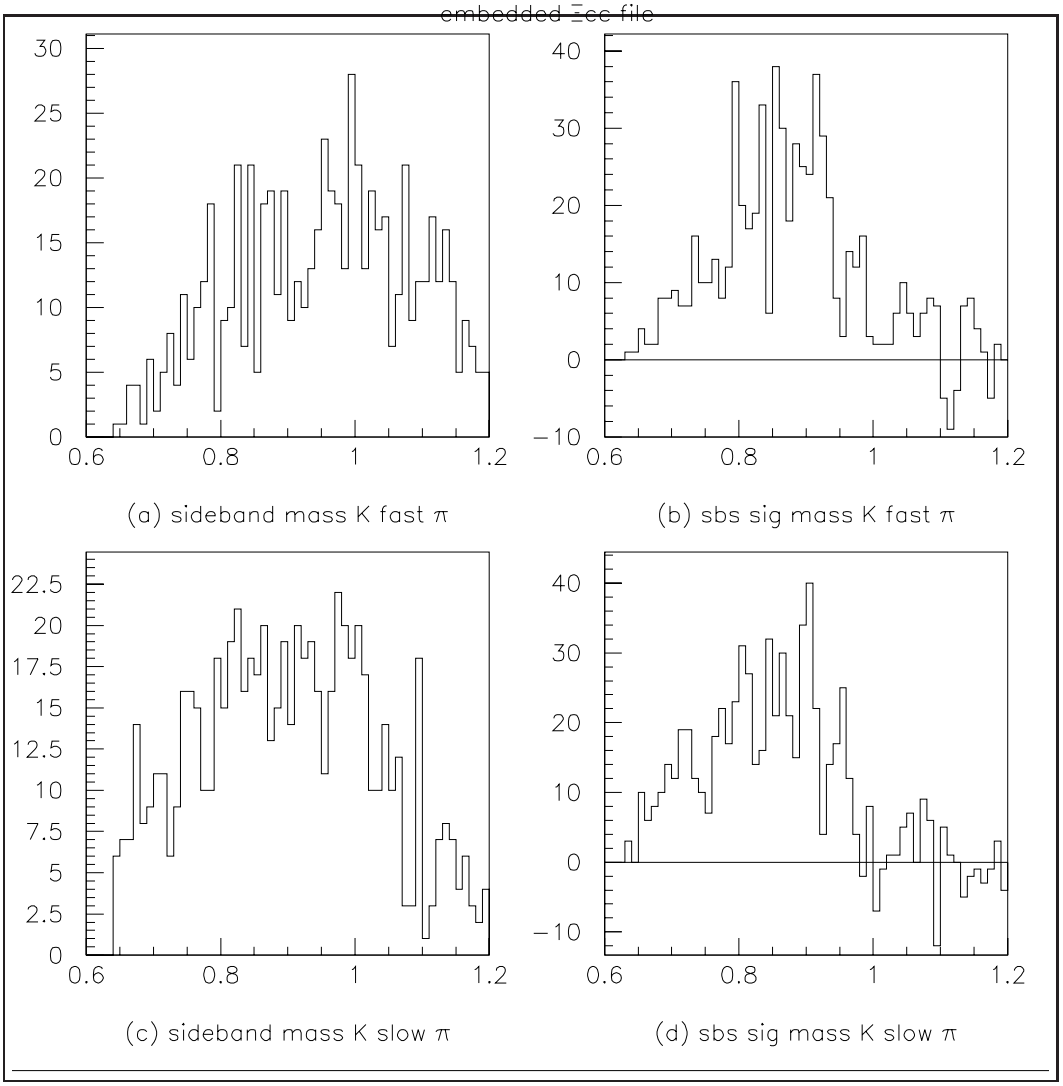

Figure 4.20: Embedded Ξ_{cc} file, $K^-\pi^+$ mass plot, 10 MeV/c^2 bin width, sideband and sideband-subtracted signal. Mass scale is in GeV/c^2. Events taken from the Ξ_{cc} reconstruction with minimum bias cuts applied. Fast and slow refer to the lab frame momentum of the pions, compared to each other.

4.5.5 Multiple candidate events

The SELEX reconstruction code allows the possibility of more than one candidate for a particular event. The ideal situation is to only allow one candidate per event, but without a clear selection criteria it is often difficult to decide what is the "right" candidate for the event. Having multiple candidates is normally not a problem, since the extra background combinations are randomly distributed about the mass plot, and are accounted for by a linear fit for the background.

We do want to check that if multiple candidates of a single event are creating a false signal, by populating a narrow mass region. For this check, we will apply two different selections. The first is to keep only one candidate per event, the candidate with the lowest $K\pi\pi$ vertex fit χ^2. The second is to keep the candidate with the longest L/σ from the $K\pi\pi$ vertex to the primary vertex. All other candidates for that particular event are removed, so each event will contribute only one point to the mass plot.

These two selections will not necessarily pick the "right" candidate. There are background events with small vertex χ^2 and/or long L/σ. However, these cuts are not be biased towards any particular mass range, and should reject some classes of background. The purpose of these selections is only to see if events with more than one candidate are distorting our results. Figure 4.21 shows that the signal persists after the selection cuts.

4.6 Statistical significance of current signal

4.6.1 Minimum bias cuts

We checked the probabilities of the $\Lambda_c^+ K^- \pi^+ \pi^+$ candidates using Poisson statistics for the mass bins, as described in the last chapter. A signal window centered at 3.760 GeV/c^2 is selected. The background is fit, using the mass bins except the signal window and the two outside bins (near 3.4 and 4.0 GeV/c^2). Assuming Poisson statistics for the background fluctuation, the probability that the number of signal events is due to a background is computed. The results for figures 4.22 through 4.25 are shown in table 4.7.

Background fits were done for both linear and quadratic, because it is not obvious which fit is correct. By eye, the quadratic curve seems to follow the high mass events better, and it has a lower χ^2. On the other hand, the

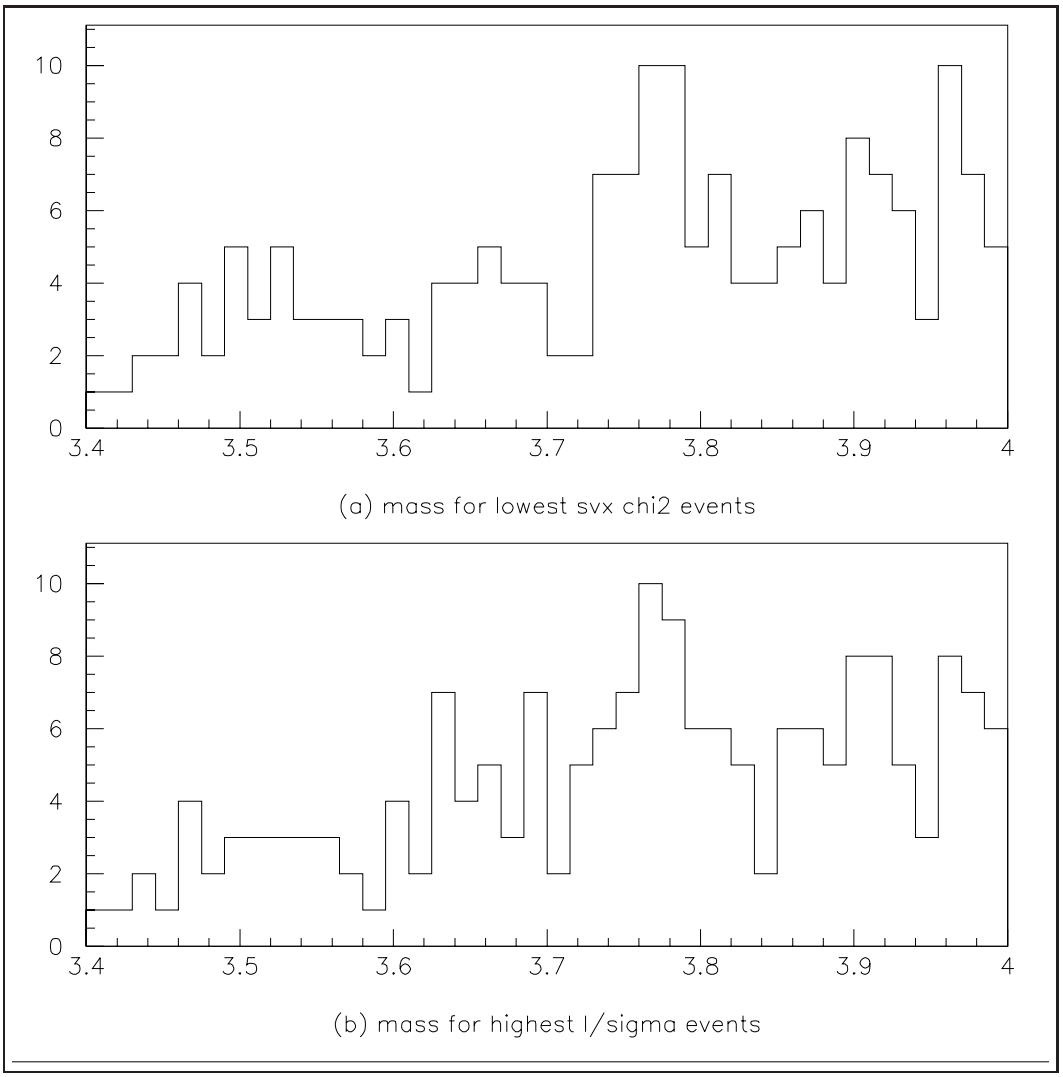

Figure 4.21: Mass plot in GeV/c^2 for real events, with only one candidate per event. (a) Lowest $K\pi\pi$ vertex fit χ^2. (b) Longest L/σ from the $K\pi\pi$ vertex to the primary vertex.

linear fit seems to follow the middle-low mass events better. The simulated background from the embedded Λ_c-only file is clearly linear in shape.

We can see that the signal probability is low, but there are other regions that are also unlikely. The background shape makes a substantial difference in the statistics. We decided to look at a signal window of 60 MeV (figures 4.24 and 4.25). This will be a cross check for binning effects, since the mass bins need to be shifted by half a bin if we want to center the signal window at 3.760 GeV. Also, in the 5 σ mass plots (figures 4.22 and 4.23), the outside bins for the signal window were almost at the same level as the background fit, which suggests that we may have gone too far into the tails of the distribution. The mass bins covering the tails of a gaussian signal will contribute very little to the signal size, but will increase the background count. We want a window large enough so we are not susceptible to normal statistical background fluctuation, but only large enough to contain the signal events.

The signal window is very unlikely to be a fluctuation of the background, and all sideband regions are much more probable. The signal persists with changes in the mass binning, while background did not.

Figure	4.22	4.23	4.24	4.25
Window Size	75 MeV	75 MeV	60 MeV	60 MeV
Background Fit	linear	quadratic	linear	quadratic
Events in Window	59	59	52	52
Background in Window	39.4	44.6	31.3	35.1
Signal in Window	19.6	14.4	20.7	16.9
Poisson Probability	0.23%	3.6%	0.05%	0.6%
χ^2 for background fit, all bins	7.9	6.2	7.9	6.3
χ^2 for background fit, w/o signal window	5.3	4.8	5.5	4.8

Table 4.7: Signal fit and poisson probability for real data Ξ_{cc} candidates. The background fit was done for the mass plot except the outermost mass bins. The signal count is the difference between the number of events in the signal window, and the integrated background fit for that window. The χ^2 per degree of freedom are for the background fit, with and without the signal window included in the fit.

Another way to visually confirm the significance of our signal is to vary the center of that fit. A gaussian distribution is used to estimate the number of events above background. The fit width is kept constant, and the fit mean mass chosen to lie at a particular value. The fit center is moved a bin at a time, until we have scanned across the mass plot. The number of events in the fit should peak near our value of 3.760 GeV/c^2, and be close to zero for sideband regions. We expect the fit count to go positive and negative, through normal statistical fluctuation of the background. Ideally the signal region should be much higher than the fluctuations. Figure 4.26 shows the results for different fit widths and backgrounds. Since the histogram is cut off after the two outermost mass bins in the plot, the fit for those bins should be ignored.

4.6.2 Pointback cut

We would like to use the pointback cut, to require that the Λ_c be consistent with coming from the $K\pi\pi$ vertex. The problem is that the $K\pi\pi$ vertex has much larger errors than the primary vertex, so the cut will have little discrimination. The lifetime check shows that our signal candidates have a short lifetime. The $K\pi\pi$ vertex should be near the primary vertex. We might also suspect that the $K\pi\pi$ tracks were assigned to the primary vertex formed for the original Λ_c reconstruction. The Λ_c momentum vector should point to near its primary vertex.

We have information about the Λ_c vertex and the primary vertex formed during that reconstruction (before the $\Lambda_c K\pi\pi$ reconstruction). We apply a pointback < 4, a measure of how well the Λ_c points back to that primary vertex. This cut was applied for the $\Xi_c \to pK\pi$ analysis [46], so it should be reasonable.

The Poisson probabilities were redone, including the pointback cut along with the minimum bias cuts. The signal windows are 75 MeV/c^2 signal window (figures 4.27 and 4.28) and 60 MeV/c^2 (figures 4.29 and 4.30). The signal window is centered at 3.760 GeV/c^2. Both linear and quadratic background fits are used. The results are listed in table 4.8

We repeated the variation in the fit center, using the pointback cut along with the minimum bias events. Figure 4.31 shows the results for different fit widths and backgrounds. Since the histogram is cut off in after the two outermost mass bins in the plot, the fit for those bins should be ignored.

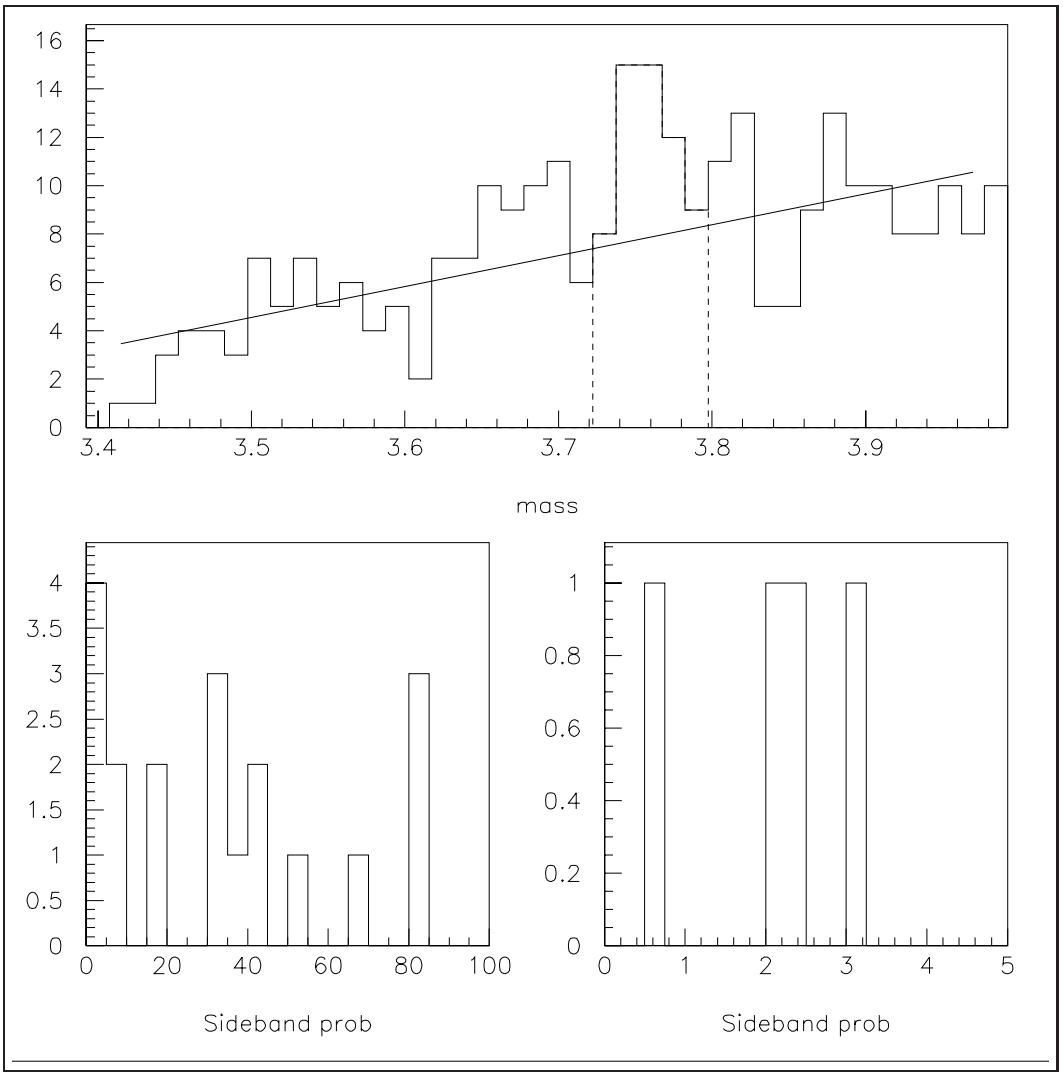

Figure 4.22: Poisson fit for real data Ξ_{cc} candidates, 5 σ signal window, 15 MeV/c^2 bin width. Mass scale is in GeV/c^2. Top plot shows the mass distribution, dashed line for the signal window, and the line fit for the background. The bottom plots are the Poisson probabilities in percent for sideband windows. Each entry represents a different sideband window. The bottom right is the same sideband results, zoomed in on the smallest probabilities.

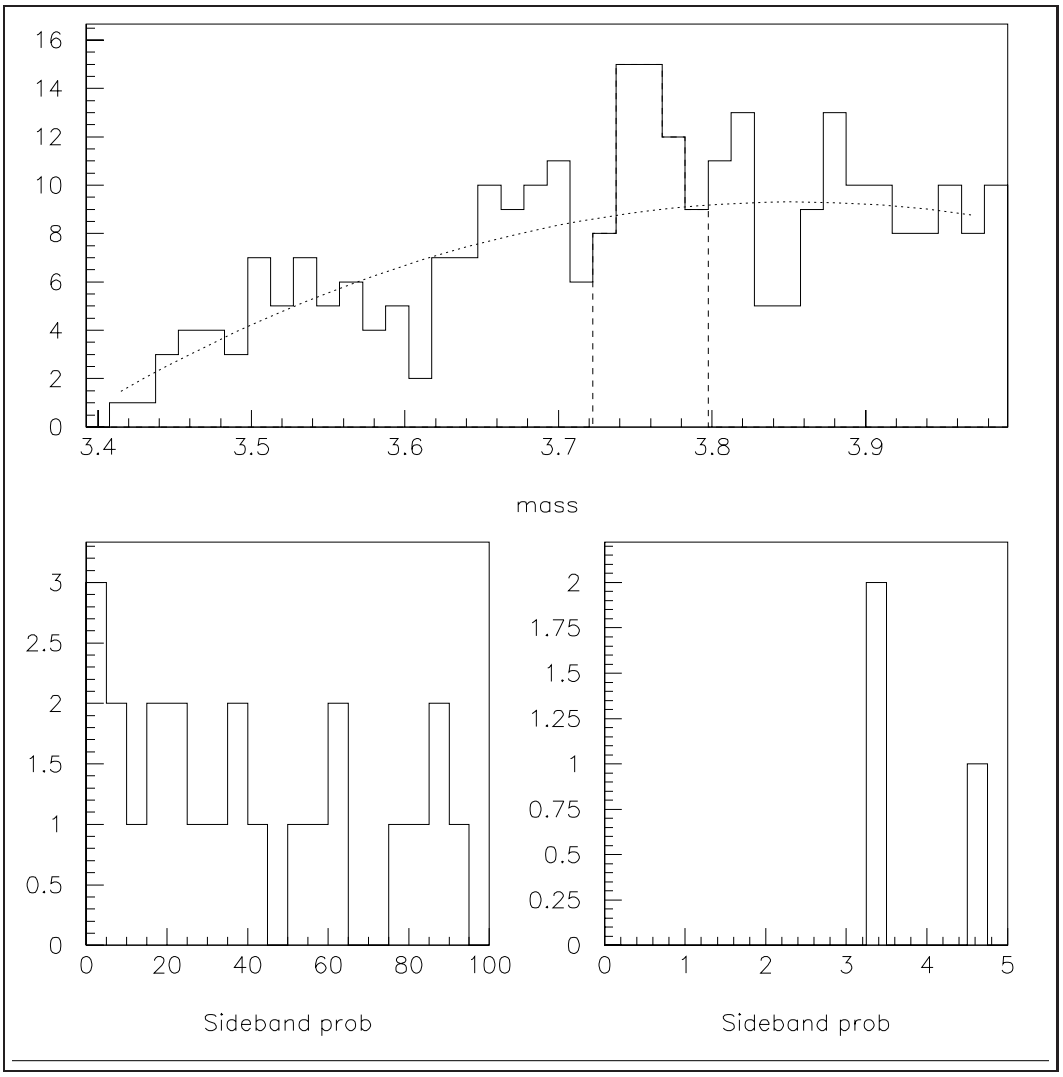

Figure 4.23: Poisson fit for real data Ξ_{cc} candidates, 5 σ signal window, 15 MeV/c^2 bin width. Mass scale is in GeV/c^2. Top plot shows the mass distribution, dashed line for the signal window, and the quadratic fit for the background. The bottom plots are the Poisson probabilities in percent for sideband windows. Each entry represents a different sideband window. The bottom right is the same sideband results, zoomed in on the smallest probabilities.

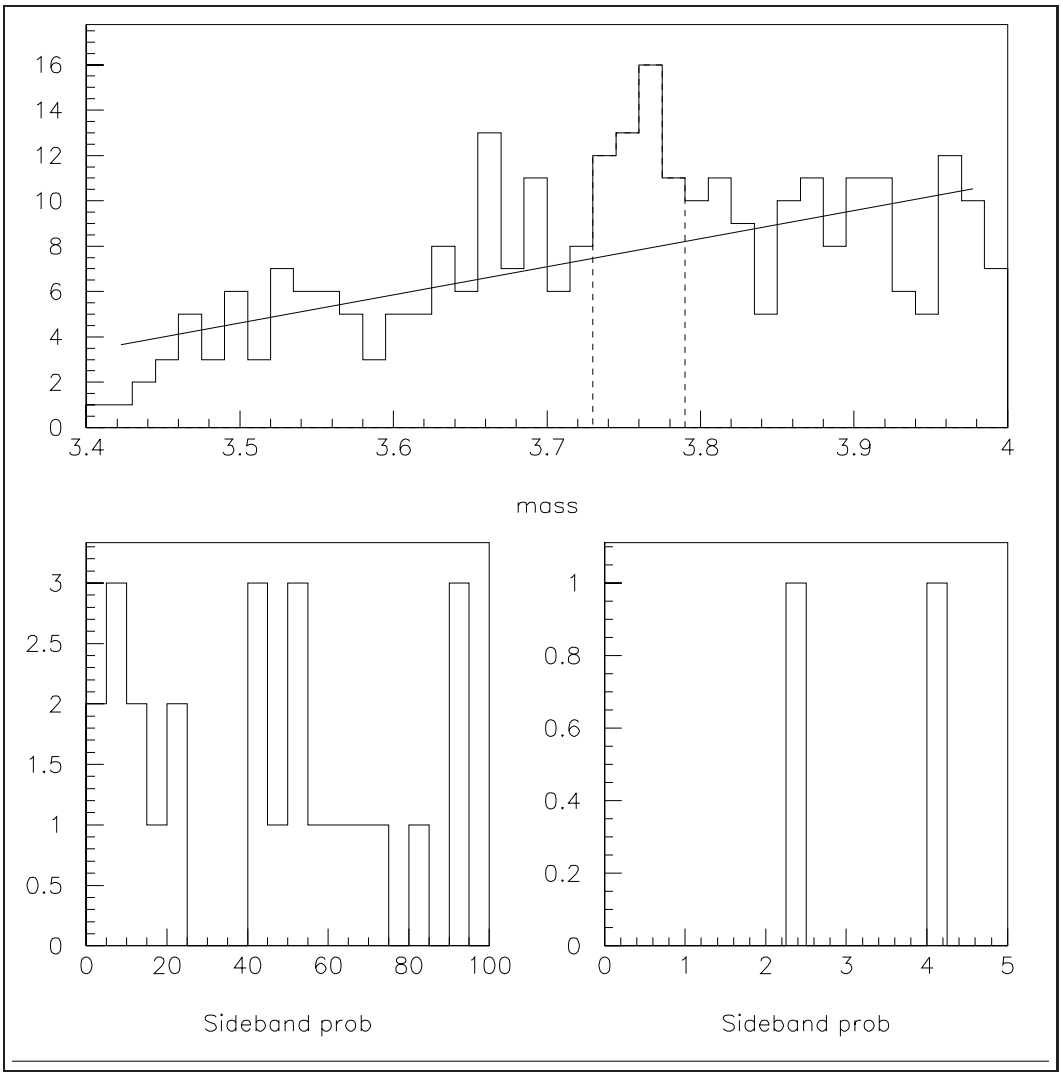

Figure 4.24: Mass plot with a 4 σ signal window, 15 MeV bin width. Top plot shows the mass distribution, dashed line for the signal window, and the line fit for the background. The bottom plots are the Poisson probabilities in percent for sideband windows. Each entry represents a different sideband window. The bottom right is the same sideband results, zoomed in on the smallest probabilities.

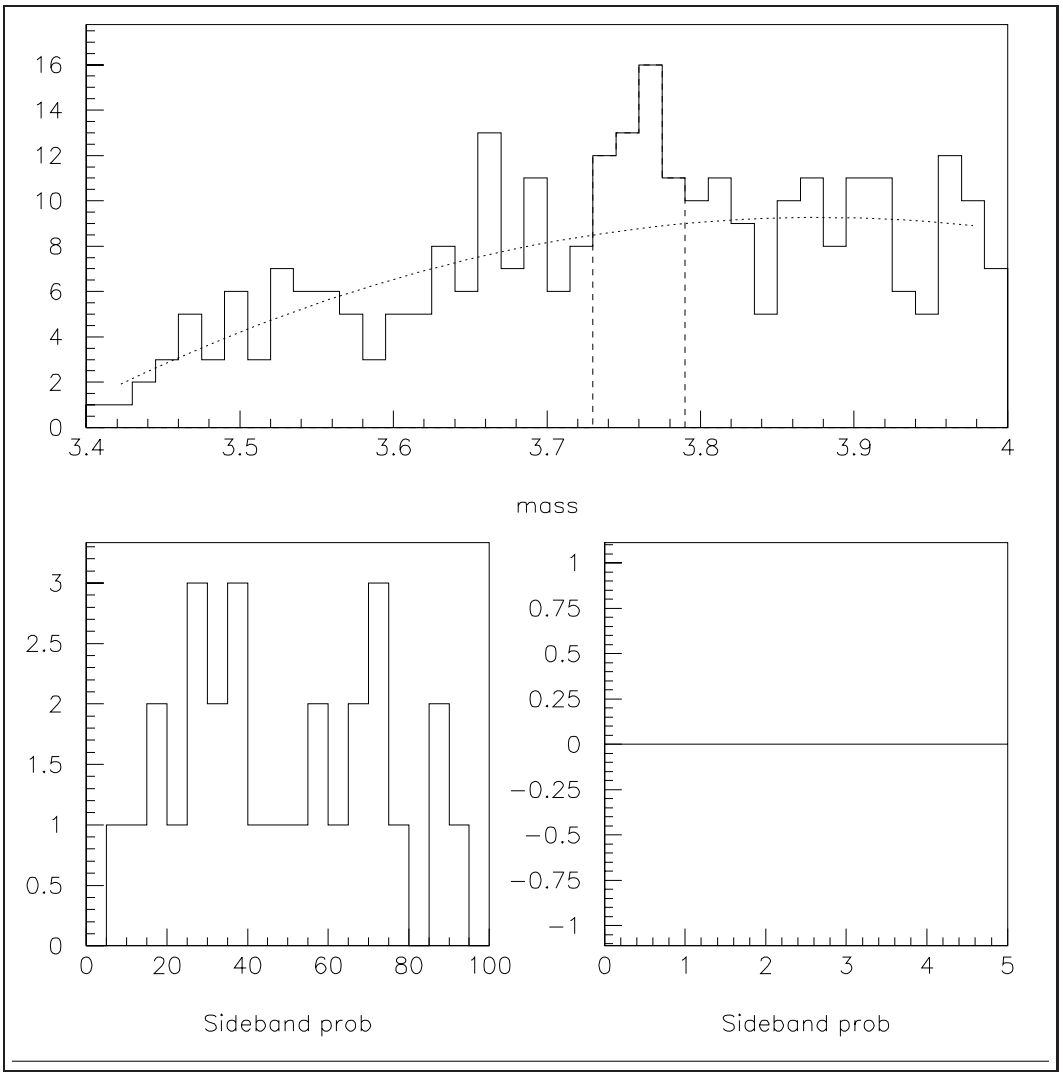

Figure 4.25: Mass plot with a 4 σ signal window, 15 MeV bin width. Top plot shows the mass distribution, dashed line for the signal window, and the quadratic fit for the background. The bottom plots are the Poisson probabilities in percent for sideband windows. Each entry represents a different sideband window. The bottom right is the same sideband results, zoomed in on the smallest probabilities.

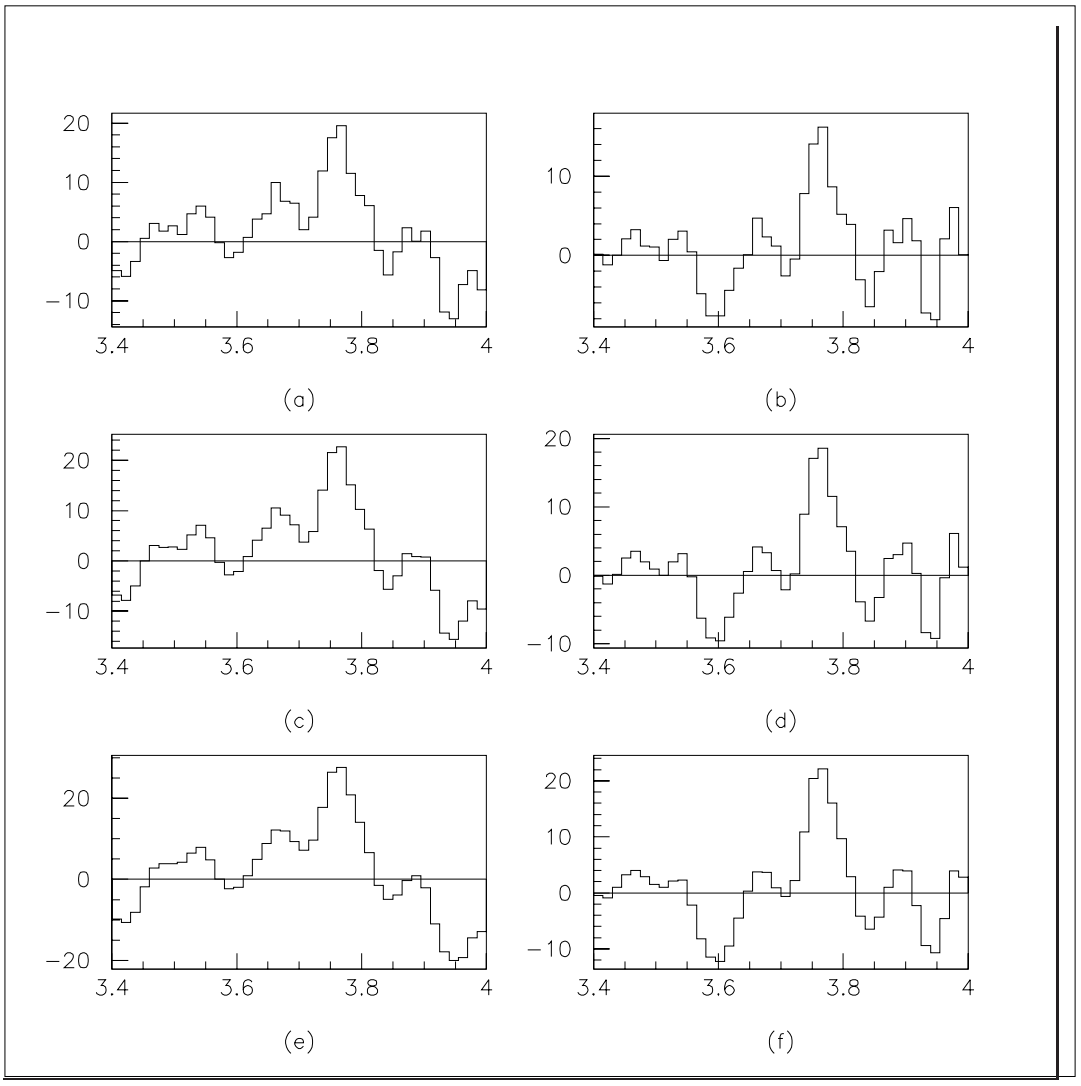

Figure 4.26: Varying mass hypothesis for real data Ξ_{cc} candidates. Minimum bias cuts are applied. The vertical axis is the number of events from a gaussian distribution fit. The fit width is kept constant. The horizontal axis is the assigned fit mean mass. The left side plots (a,c,e) are using linear background fit, the right side (b,d,f) are using a quadratic background fit. Plots (a,b) have a fit width of 12 MeV/c^2, (c,d) has a fit width of 15 MeV/c^2, and (e,f) has a fit width of 20 MeV/c^2.

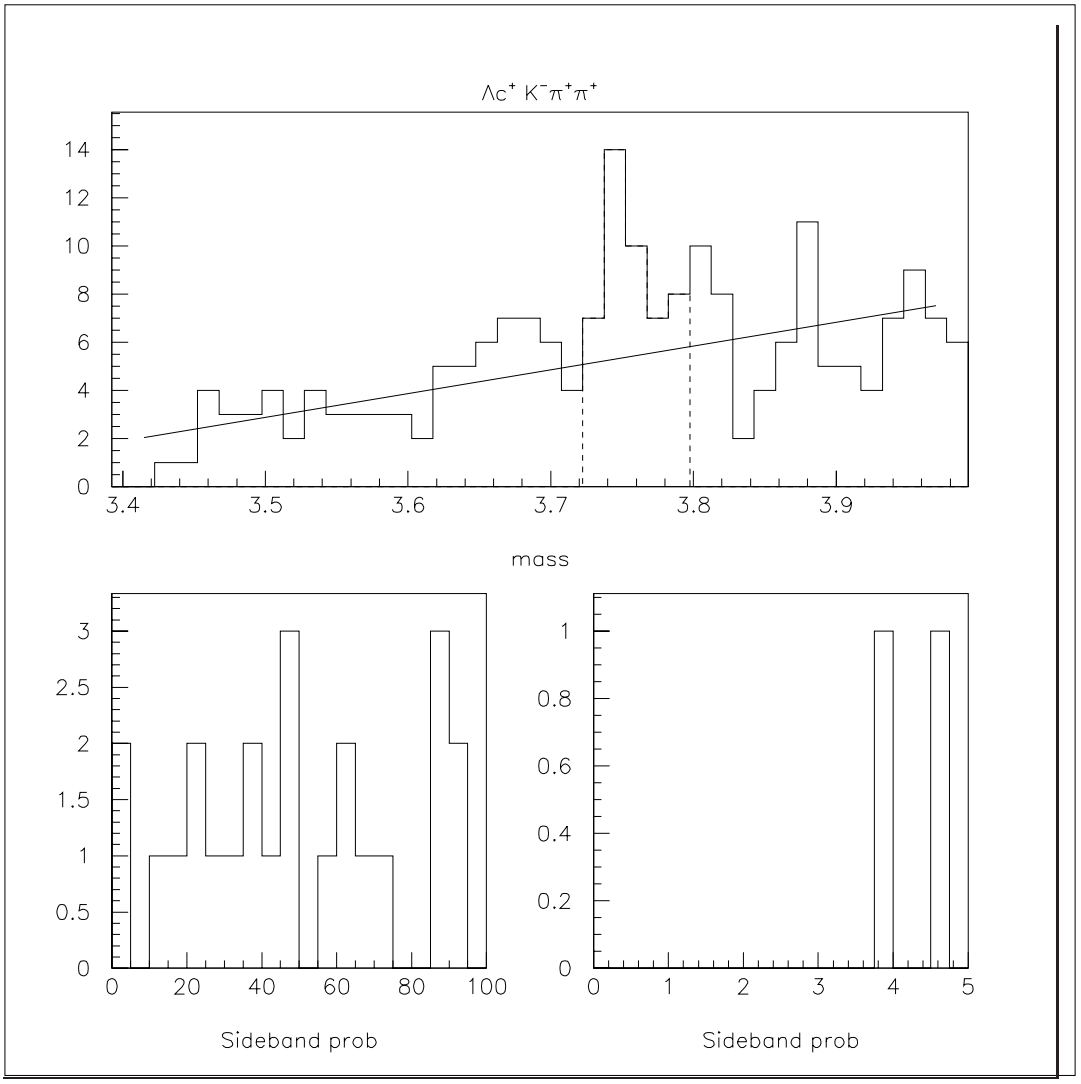

Figure 4.27: Poisson fit for real data Ξ_{cc} candidates, 5 σ signal window, 15 MeV/c^2 bin width. Real data with minimum bias and Λ_c pointback < 4 are applied. Mass scale is in GeV/c^2. Top plot shows the mass distribution, dashed line for the signal window, and the line fit for the background. The bottom plots are the Poisson probabilities in percent for sideband windows. Each entry represents a different sideband window. The bottom right is the same sideband results, zoomed in on the smallest probabilities.

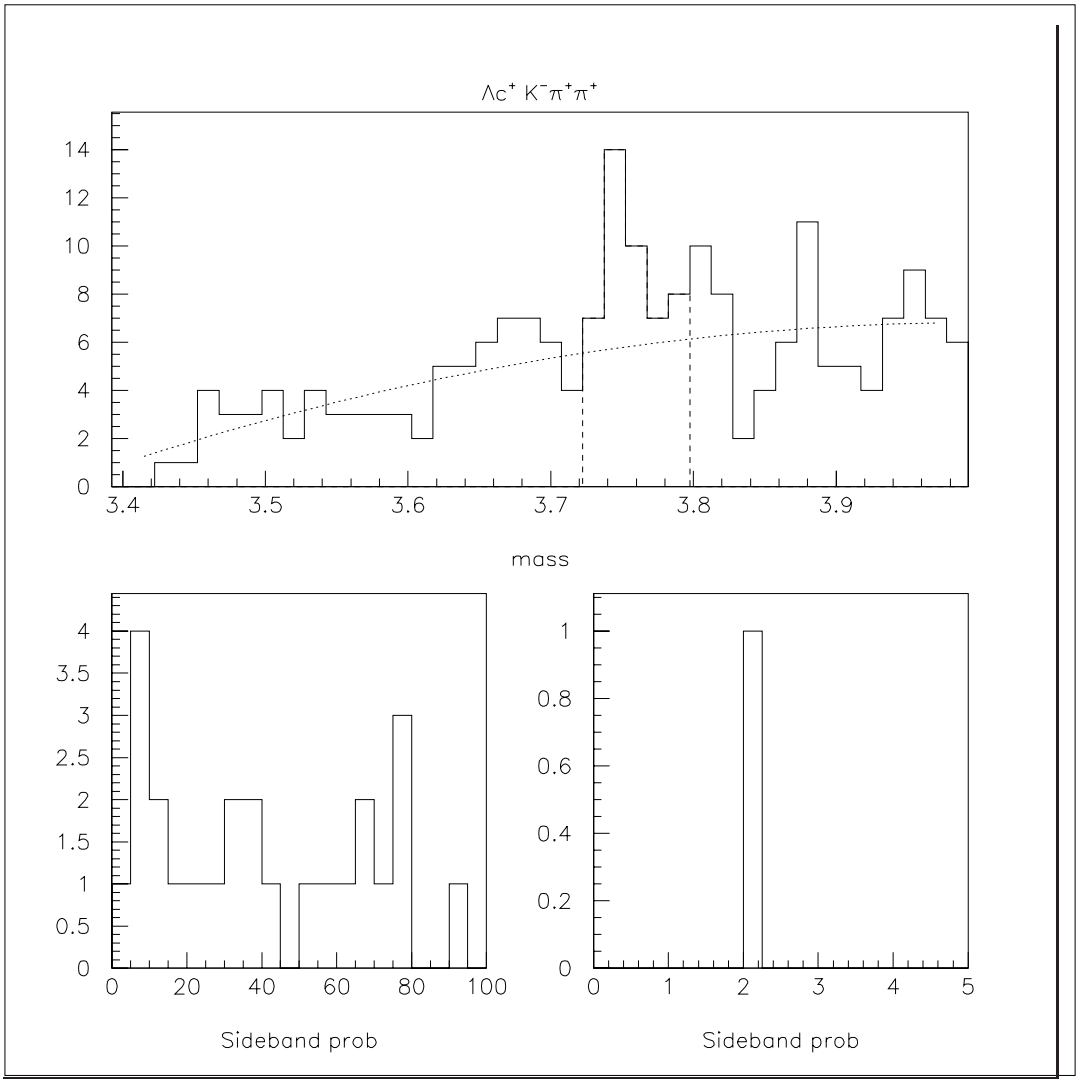

Figure 4.28: Poisson fit for real data Ξ_{cc} candidates, 5 σ signal window, 15 MeV/c^2 bin width. Real data with minimum bias and Λ_c pointback < 4 are applied. Mass scale is in GeV/c^2. Top plot shows the mass distribution, dashed line for the signal window, and the quadratic fit for the background. The bottom plots are the Poisson probabilities in percent for sideband windows. Each entry represents a different sideband window. The bottom right is the same sideband results, zoomed in on the smallest probabilities.

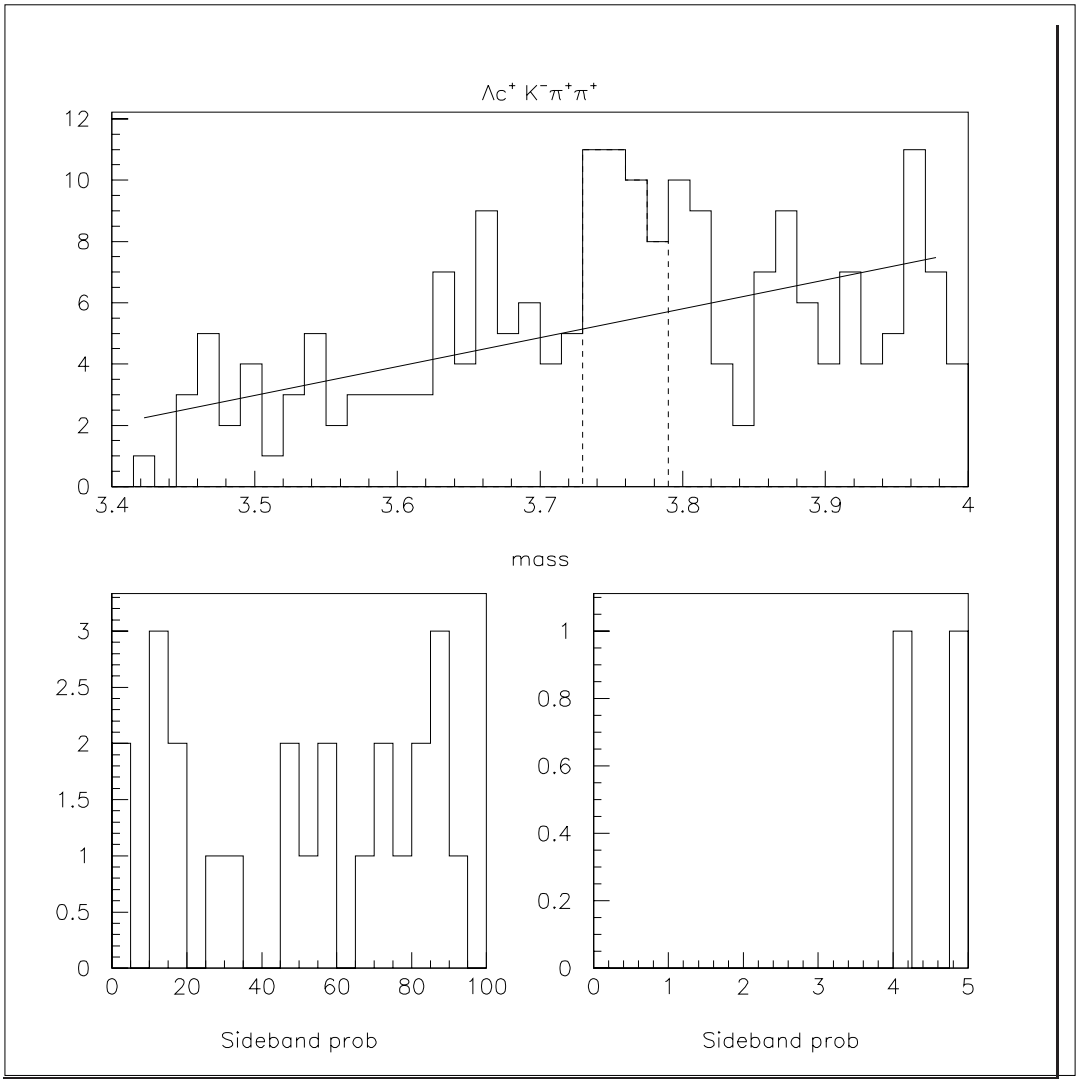

Figure 4.29: Mass plot with a 4 σ signal window, 15 MeV bin width. Real data with minimum bias and Λ_c pointback < 4 are applied. Top plot shows the mass distribution, dashed line for the signal window, and the line fit for the background. The bottom plots are the Poisson probabilities in percent for sideband windows. Each entry represents a different sideband window. The bottom right is the same sideband results, zoomed in on the smallest probabilities.

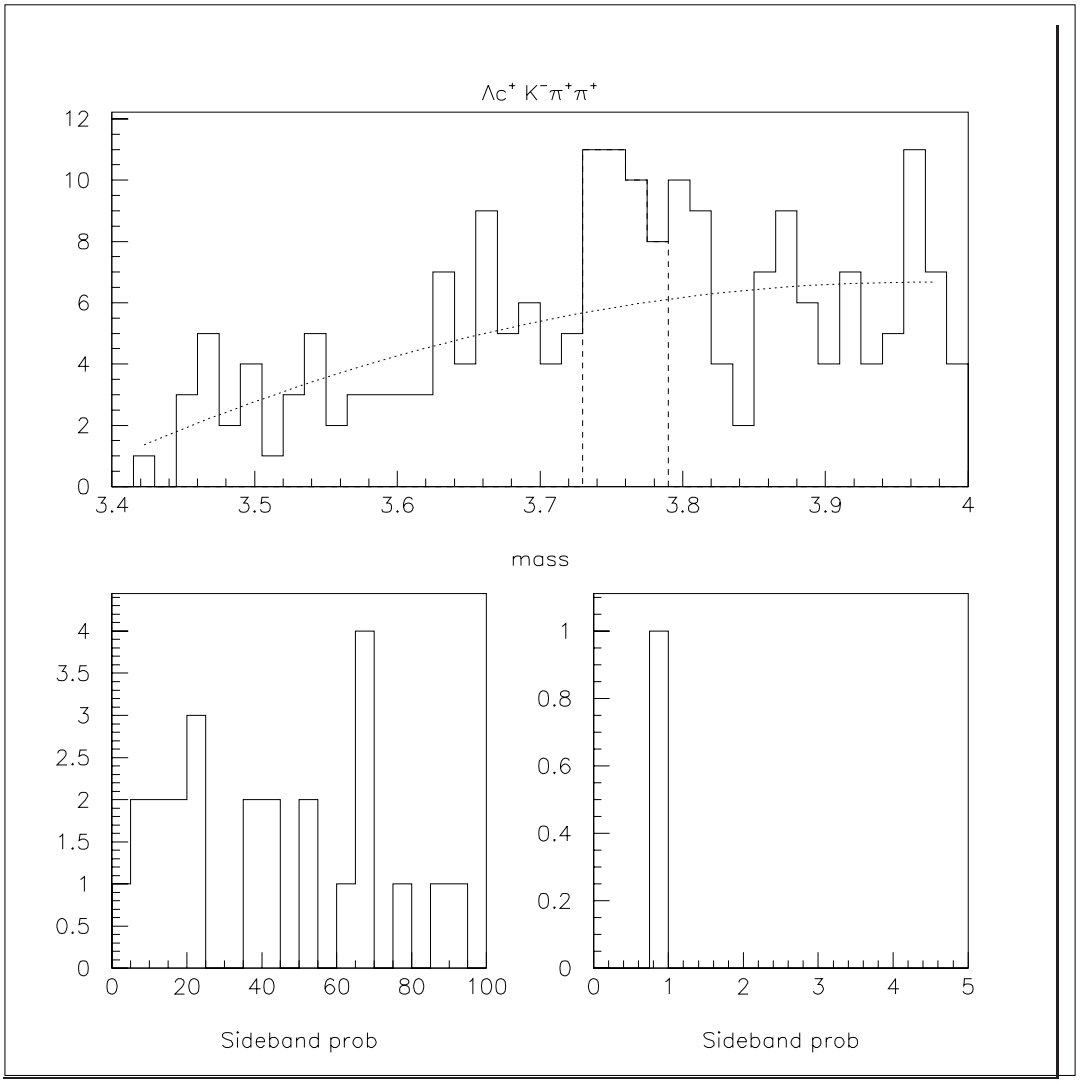

Figure 4.30: Mass plot with a 4 σ signal window, 15 MeV bin width. Real data with minimum bias and Λ_c pointback < 4 are applied. Top plot shows the mass distribution, dashed line for the signal window, and the quadratic fit for the background. The bottom plots are the Poisson probabilities in percent for sideband windows. Each entry represents a different sideband window. The bottom right is the same sideband results, zoomed in on the smallest probabilities.

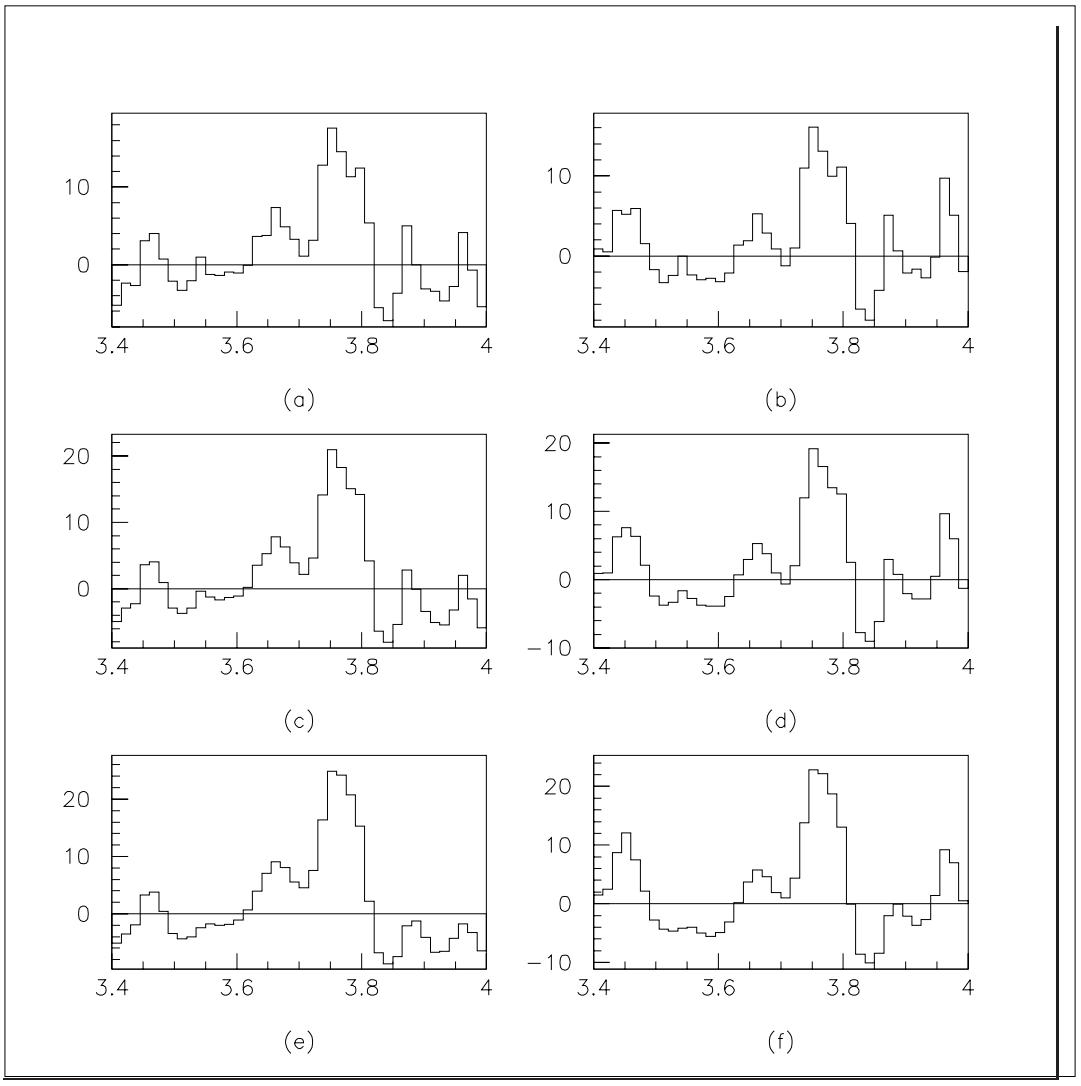

Figure 4.31: Varying mass hypothesis for real data Ξ_{cc} candidates. Minimum bias cuts and the Λ_c pointback < 4 are applied. The vertical axis is the number of events from a gaussian distribution fit. The fit width is kept constant. The horizontal axis is the assigned fit mean mass. The left side plots (a,c,e) are using linear background fit, the right side (b,d,f) are using a quadratic background fit. Plots (a,b) have a fit width of 12 MeV/c^2, (c,d) has a fit width of 15 MeV/c^2, and (e,f) has a fit width of 20 MeV/c^2.

Figure	4.27	4.28	4.29	4.29
Window Size	75 MeV	75 MeV	60 MeV	60 MeV
Background Fit	linear	quadratic	linear	quadratic
Events in Window	46	46	40	40
Background in Window	27.2	29.2	21.7	23.6
Signal in Window	18.8	16.8	18.3	16.4
Poisson Probability	0.06%	0.3%	0.03%	0.14%
χ^2 for background fit, all bins	6.0	5.2	6.4	5.8
χ^2 for background fit, w/o signal window	3.8	3.6	4.7	4.6

Table 4.8: Signal fit and poisson probability for real data Ξ_{cc} candidates, with the pointback cut applied. The background fit was done for the mass plot except the outermost mass bins. The signal count is the difference between the number of events in the signal window, and the integrated background fit for that window. The χ^2 per degree of freedom are for the background fit, with and without the signal window included in the fit.

Chapter 5

Conclusion

There are three explanations for the excess of events in the $\Lambda_c^+ K^- \pi + \pi +$ mass plot. The first is that we have a statistical fluctuation. The probability that the peak comes from background variation is very small. Combined with some peculiar differences between signal and sideband background, this makes a statistical explanation extremely unlikely. The second is that we have introduced a kinematic enhancement from our choice of cuts, a systematic bias. This is also unlikely. The types of cuts were used in other SELEX charm analyzes, and the values of the cuts were done independently of the signal. There is no evidence that these cuts would artificially produce a mass peak.

The last choice is real physics. If it turns out to be the Ξ_{cc}^{++}, this has serious consequences for current theory. Our mass of 3.76 GeV, even with an uncertainty of the order of 20 MeV, is higher than theoretical predictions for the ground state Ξ_{cc} mass. It may be that the signal is not the ground state Ξ_{cc}^{++}, which would raise the question of where is the ground state. If it is not a doubly charmed baryon, then we would have to explore new physics. The mass peak is more than 1 GeV/c^2 higher than the Ω_c^0, and too low for the bottom quark. For production of Ξ_{cc}, the guess is that the Ξ_{cc}^{++} is suppressed by a factor of a thousand compared to Λ_c. If the embedded Ξ_{cc} data is accurate, from table 4.3 we should expect to see (3178/865 =) 3.7 reconstructed Λ_c for every Ξ_{cc} in our signal. With 20 signal events, that would mean 74 Λ_c produced by Ξ_{cc}, compared to our total sample of 1656. This would give a production ratio of $\sigma(cc)/\sigma(c) \approx 74$ / 1656 = 4.5 %. Our real data signal has a shorter lifetime than the embedded Ξ_{cc} files, which implies that our efficiency for finding the Ξ_{cc} candidate is even lower, so the

ratio is even larger.

Other experiments can cross check our results. For example, FOCUS and CLEO have large charm samples. However, if an enhancement in the double charm production depends on a hadronic beam particle, they may not see anything, due to production differences. FOCUS uses a photon beam on a fixed target, and CLEO has e^+e^- collisions. With future experiments expected to have several orders more charm baryons produced, doubly charmed baryons are bound to be observed.

There is room for further study with the SELEX experiment. This data is still under investigation. Recently, a second (and final) analysis pass was done over the charm data set. Additional Λ_c decay modes involving downstream strange decays, such as $\Lambda_c^+ \to \Lambda\pi^+\pi^+\pi^-$, have yet to be explored. If we use the same Λ_c^+ reconstruction that was used in this search, we will have 2200 Λ_c candidates with tight cuts, compared to the 1650 in the first analysis pass sample that is used here.

Figure 5.1 shows the current state of our $\Lambda_c^+ K^-\pi^+\pi^+$ signal. This particular fit yields 20.7 events in excess of a fitted background of 31.3 events, with a 0.05 % Poisson probability that the events in the signal window are from background fluctuation.

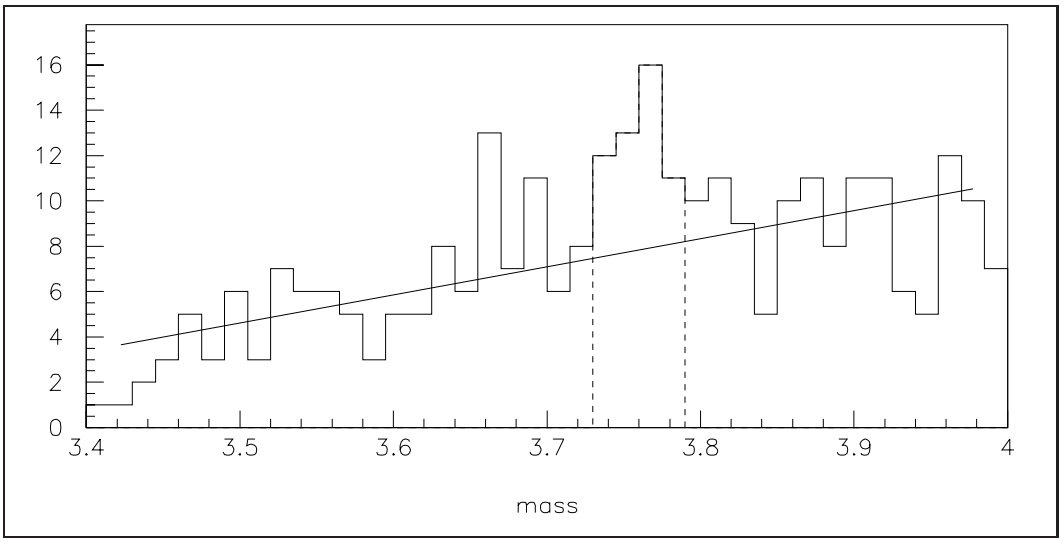

Figure 5.1: Current Ξ_{cc}^{++} candidate mass plot with a 4 σ signal window, 15 MeV bin width. The dashed line shows the signal peak, and the line is the background fit.

Appendix A

Theoretical track fitting for SELEX

A.1 Introduction

This chapter details the theory for how the detector hits are used to obtain the track position and momentum. Most examples of track fitting use an idealized, simplified model as an example. Working out a more complete solution will detail the assumptions and approximations used to get the physics results.

A.2 Variance and Covariance

Part of the fitting process is knowing how to weight the detector hits. A silicon detector with a 20 micron strip pitch is expected to have more information about a particle's position than a wire chamber with a 2 millimeter wire spacing, so the silicon hits should be given greater priority in the calculations. The weights used will depend on the variance (spread of possible values) and the covariance (how a hit in one detector relates to hits in other detectors).

To model the detector, we will assign it a variable X, which gives the probability $p(x)$ that the particle passed through the detector at location x.

The expectation (or mean) value is given by

$$\bar{x} = \int xp(x)dx$$

The variance (or standard deviation) is given by

$$\sigma_X^2 = \int (x - \bar{x})^2 p(x) dx$$

If there is a second detector modeled by variable Y, we will want to know how hits in the two detectors are correlated. The covariance of the two variables is given by

$$\sigma_{X,Y} = \int\int (x - \bar{x})(y - \bar{y}) p(x, y) dy dx$$

Note that $\sigma_{X,X} = \sigma_X^2$.

To simplify the math work done later, some useful properties for variance and covariance will be given here. For variables X,Y, and constants a,b,c,d :

$$\begin{aligned}
Var[aX + b] &= a^2\ Var[X] \\
Cov[aX + b, cY + d] &= ac\ Cov[X, Y] \\
Var[X + Y] &= Var[X] + Var[Y] + Cov[X, Y] \\
Cov[\sum_{i=1}^{n} X_i, \sum_{j=1}^{m} Y_j] &= \sum_{i=1}^{n}\sum_{j=1}^{m} Cov[X_i, Y_j]
\end{aligned}$$

A.3 Generic fitting

Before starting the mathematical work, it is helpful to list the variables used and what they mean. The indices i and j are being reused; the range of values depends on the number of detector planes and fit parameters being used.

- x_i - detector hit position in the i-th plane coordinate system
- z_i - position of the i-th plane in the z (beam) direction
- p_i - track parameters in global coordinates
- $\tilde{x_i}$ - track position in the i-th plane coordinates
- θ_i^2 - variance in track angle (compared to it's production angle)

- σ_{ij} - covariance for the i-th and j-th detector planes
- $\tilde{\sigma}_{ij}$ - covariance for the track parameters
- **h** - matrix mapping track parameters to a plane coordinate system ($h_{ij}p_j = \tilde{x_i}$)

The relationship between the two covariant error matrices are given by

$$\sigma_{x_i x_j} = \sum_{km} (\partial x_i/\partial p_k)\, \tilde{\sigma}_{p_k p_m}\, (\partial x_j/\partial p_m)$$

In practice, it is easier to make a model to compute the covariant error matrix $\boldsymbol{\sigma}$, which can then be used to get the more useful errors on the fit parameters. The inverses of the matrices are used to get

$$\begin{aligned} \tilde{\sigma}^{-1}_{p_k p_m} &= \sum_{ij} (\partial x_i/\partial p_k)\, \sigma^{-1}_{x_i x_j}\, (\partial x_j/\partial p_m) \\ &= \sum_{ij} h_{ik}\, \sigma^{-1}_{x_i x_j}\, h_{jm} \end{aligned}$$

The usual method get fit parameters is to start with the maximum likelihood, where

$$L \propto e^{-\chi^2}$$

and

$$\chi^2 = \sum_{ij} (x_i - \tilde{x_i})(x_j - \tilde{x_j})(\sigma^{-1})_{ij}$$

The best fit parameters will maximize the likelihood, which is done by minimizing the square of the distance of the detector hits from the predicted track position. The inverse of the covariant errors σ^{-1} sets the scale for the distance; detector planes with poorer resolution will be weighted less than more precise detectors.

The likelihood will be maximized when

$$\begin{aligned} \partial L/\partial p_i &= 0 \\ \Rightarrow \partial \chi^2/\partial p_i &= 0 \\ \Rightarrow \sum_{jk} (\sigma^{-1})_{jk} (x_j - \tilde{x_j})(\partial \tilde{x_k}/\partial p_i) &= 0 \end{aligned}$$

for all parameters.

The last equation can be used to solve for the fit parameters.

$$\begin{aligned}
\sum_{jk}(\sigma^{-1})_{jk}\tilde{x_j}(\partial\tilde{x_k}/\partial p_i) &= \sum_{jk}(\sigma^{-1})_{jk}x_j(\partial\tilde{x_k}/\partial p_i) \\
\sum_{jkm}(\sigma^{-1})_{jk}h_{jm}p_m h_{ki} &= \sum_{jk}(\sigma^{-1})_{jk}x_j h_{ki} \\
\sum_{m}(\tilde{\sigma}^{-1})_{mi}p_m &= \sum_{jk}(\sigma^{-1})_{jk}x_j h_{ki} \\
\Rightarrow p_m &= \sum_{ijk}\tilde{\sigma}_{im}(\sigma^{-1})_{jk}h_{ki}x_j
\end{aligned}$$

A.4 Multiple Coulomb Scattering

A charged particle passing through a medium will experience repeated small angle deflections, mostly due to elastic Coulomb scatterings from the nuclei. The angular distribution from multiple Coulomb scattering was first worked out by Moliere [47]. That work was expanded and clarified by Bethe [48] and others. The description used for this study is based on the paper by Lynch and Dahl. [49] They do an excellent job of pointing out which calculations have been verified by data, and which are incorrect.

The distribution has two main features. The central portion is almost Gaussian in shape, and is due to many small angle scatters. A single scatter is described by the Rutherford formula, and has a distribution like $1/sin^4(\theta/2)$. The tails of the distribution are much wider, and are expected from single, large angle scatters. The effect of the tails is that the RMS width of the scattering distribution is infinite.

The usual approach is to make a fit to the central portion of the distribution, ignoring the very large angle tails. An empirical formula to get the Gaussian width was presented by Highland, and improved by Lynch and Dahl:

$$\theta_{mcs} = \frac{13.6MeV}{\beta cp}z\sqrt{x/X_0}[1 + 0.038\log(x/X_0)]$$

where p, βc, and z are the momentum, velocity and charge number of the incident particle, and x/X_0 is the thickness of the scattering medium in radiation lengths. Although the real distribution is only roughly Gaussian,

but this equation is accurate to 11% or better for the central 98% of the distribution.

Since this form ignores the long tails, Lynch and Dahl wrote a warning concerning complex scatters. If a particle crosses more than one media, adding the Gaussian widths of each media in quadrature will result in an answer smaller and more inaccurate as the number of scatterers increases. A better approach is to get the sum of the radiation lengths of all the media, then to make the width calculation for all the material.

A.5 Model For Calculating Covariant Error Matrix

For the following example, we will use variables to describe the position of our ideal charged particle, if it's path could be known precisely. The track starts at a position of (X_0, z_0), traveling at an angle of Θ_0 in the xz plane, compared to the z axis. At plane i, the track has coordinates (X_i, z_i) and an angle of Θ_i after passing through the plane. To simplify the situation, this example will ignore the y position and angle.

The z positions of the detector are assumed to have negligible error. The distance between planes will be defined as

$$\Delta z_i = (z_i - z_{i-1})$$

The position of the particle at each plane can be given by

$$X_i = X_{i-1} + \Theta_{i-1}\Delta z_i$$

assuming the particle's parameters are unchanged as it passes between planes. This will reduce the problem to the initial x position, the initial angle, and the angle at each plane.

After passing through a target or a silicon strip detector, we account for multiple scattering. The change in angle should be random and symmetric, so the mean value of the angle should be the same before and after the plane. The variance of the angle will be computed from the MCS formulas worked above. The position (and variance of the position) will also change as the particle passes through the material, but can be ignored since the material is thin.

For a wire chamber, we assume that the particle is passing through the gases in the chamber, so the scattering is negligible. The track angles will be the same before and after the plane.

The covariant error matrix will be a n by n, where n is the number of detector planes that have a hit assigned to the track being investigated. All other material, including detectors that do not register a hit, will still potentially affect the particle's path. Thus, we will have to compute the variance and covariance for all planes, which will then be used to get the covariant error matrix for the planes used in the fit.

So for a given plane i (and $i < j$),

$$Var[\Theta_i] = \theta_i^2$$

$$\begin{aligned} Cov[\Theta_i, \Theta_j] &= Cov[\Theta_i, \Theta_i] + Cov[\Theta_i, (\Theta_j - \Theta_i)] \\ &= Var[\Theta_i] + 0 \\ &= \theta_i^2 \end{aligned}$$

As stated before, we expect no correlation between an angle at a plane, and the angle difference (scattering) as a particle passes through the plane.

Before proceeding, it is useful to calculate

$$\begin{aligned} Cov[X_i, \Theta_j \Delta z_{j+1}] &= Cov[X_{i-1}, \Theta_j \Delta z_{j+1}] + Cov[\Theta_{i-1} \Delta z_i, \Theta_j \Delta z_{j+1}] \\ &= Cov[X_{i-1}, \Theta_j \Delta z_{j+1}] + \Delta z_i \, \Delta z_{j+1} \theta_{i-1)^2} \\ &= Cov[X_1, \Theta_j \Delta z_{j+1}] + \sum_{k=1}^{i-1} \Delta z_{k+1} \, \Delta z_{j+1} \theta_k^2 \\ &= \sum_{k=1}^{i-1} \Delta z_{k+1} \, \Delta z_{j+1} \theta_k^2 \end{aligned}$$

Since X_1 depends only on the initial parameters, which have no uncertainty, that term disappears.

Now there is enough information to fill the covariance matrix

$$\begin{aligned} Var[X_1] &= 0 \\ Var[X_2] &= (\Delta z_2)^2 \theta_1^2 \\ Cov[X_1, X_2] &= 0 \end{aligned}$$

$$\begin{aligned} Var[X_i] &= Var[X_{i-1}] + Var[X_i - X_{i-1}] + 2Cov[X_{i-1}, (X_i - X_{i-1})] \\ &= Var[X_{i-1}] + (\Delta z_i)^2 \, Var[\Theta_{i-1}] + 2Cov[X_{i-1}, \Delta z_i \Theta_{i-1}] \\ Var[X_i] &= Var[X_{i-1}] + (\Delta z_i)^2 \theta_{i-1}^2 + 2 \sum_{j=1}^{i-2} \Delta z_{j+1} \, \Delta z_i \theta_j^2 \end{aligned}$$

$$
\begin{aligned}
Cov[X_i, X_j] &= Cov[X_i, X_i] + \sum_{k=i+1}^{j} Cov[X_i, (X_k - X_{k-1})] \\
&= Var[X_i] + \sum_{k=i+1}^{j} \Delta z_k Cov[X_i, \Theta_{k-1}] \\
Cov[X_i, X_j] &= Var[X_i] + \sum_{k=i+1}^{j} \sum_{m=1}^{i-1} \Delta z_k \Delta z_{m+1} \theta_m^2
\end{aligned}
$$

This is enough information to calculate the terms needed. The necessary information are the z positions from alignment, the calculated MCS at each plane, and the assumption that the initial parameters have zero uncertainty. Using a computer and induction, any particular term can then be calculated.

Tracking was done primarily with two types of detectors, silicon microstrips and proportional wire chambers. A charged particle passing through a detector will deposit a charge along its path due to ionization. In our ideal model, the charge will move to the nearest wire (silicon strip) and be collected there. So when a detector has a hit wire (strip), we assume that the particle has a uniform probability of being anywhere up to half a wire spacing away from the wire (half a strip pitch from the center of the microstrip). In the detector coordinate system, the y direction is along the length of a wire, and the x direction is perpendicular to that. A hit will only give information of the x position, except that the particle did not pass outside the detector in the y direction.

The best value for the hit position will be the wire position (strip center). The variance of the actual track position to the best guess is the wire spacing (strip pitch) squared, divided by 12. The variance due to the finite size of the detector elements is independent to the track scattering, and there should be no correlation between detectors. The covariance error matrix for the detector hits are given by

$$
\begin{aligned}
Var[x_i] &= Var[X_i] + (wirespacing)^2 \div 12 \\
Cov[x_i, x_j] &= Cov[x_i, x_i]
\end{aligned}
$$

If we are willing to accept the underestimate of errors, we can assume that the MCS errors can be added in quadrature. This will simplify the calculations. For $(i < j)$,

$$Cov[X_i, X_j] \;=\; \sum_{k=1}^{k<i} \theta^2_{mcs} \times (z_i - z_k)(z_j - z_k)$$

We also need to account for planes that are rotated with respect to each other. The covariance term will be modified to be $Cov[x_i, x_j] \times cos(\phi_i - \phi_j)$.

A.6 Motion through a magnetic field

Consider a charged particle with momentum p and charge q passing through a uniform magnetic field B. The force on the particle is given by

$$\vec{F_B} = q(\vec{v} \times \vec{B}),$$

where v is the velocity. Since the force is always at a right angle to the direction of motion, the path of the particle, at that moment, is a circle with radius of curvature

$$R = \frac{pc}{qB}.$$

Now take a X-Z coordinate system with the magnetic field perpendicular to this plane (in the Y direction). The particle is traveling at an angle θ_0 to the horizontal axis. After moving a horizontal distance δz, it will have it's momentum rotated by an amount $\delta\theta$. Since the motion is circular with radius R,

$$\delta z = Rsin(\theta_0 + \delta\theta) - Rsin\theta_0.$$

Now consider the case where the magnetic field is not uniform. The instantaneous motion is still as described above, so

$$\begin{aligned} dz/R(z) &= \sin(\theta(z) + d\theta) - \sin\theta(z) \\ dz\,\rho qB(z)/c &= \sin\theta(z)\,\cos d\theta + \sin d\theta\,\cos\theta(z) - \sin\theta(z) \\ \rho(q/c)\,B(z)dz &= \cos\theta(z)\,d\theta \end{aligned}$$

since for an infinitesimal rotation, $\cos(d\theta) \to 1$, and $\sin(d\theta) \to d\theta$. The new variable ρ introduced is curvature, the inverse of the momentum perpendicular to the magnetic field. The total momentum would be $p = \sqrt{p_y^2 + (1/\rho)^2}$. Both the magnetic field and the momentum angle depend on the particles z

position, with the assumption that $\theta(z)$ is small (primarily traveling in the z direction).

Integrating the equation gives,

$$\begin{aligned}\int_{\theta_0}^{\theta(z)} \cos\theta\, d\theta &= \rho(q/c)\int_{z_0}^{z} B(z')\, dz' \\ \sin\theta(z) - \sin\theta_0 &= \rho(q/c)\int_{z_0}^{z} B(z')\, dz'\end{aligned}$$

For the vertical displacement caused by the magnetic field, start with $\theta(z)$, which is the particle's direction with respect to the z-axis. For an infinitesimal distance traveled,

$$dx = \tan\theta(z)\, dz.$$

Now we make two assumptions. First, the magnetic field is a function of z position only. Second, that the angle at any particular z position does not change much from the initial angle θ_0. Since $\tan\theta = \sin\theta/\sqrt{1-\sin^2\theta}$, making a Taylor expansion around $\sin\theta_0$ yields

$$\tan\theta(z) = \tan\theta_0 + (1-\sin^2\theta_0)^{-3/2}(\sin\theta(z) - \sin\theta_0).$$

Integration yields,

$$\begin{aligned}\int_{x_0}^{x(z)} dx\prime &= \int_{z_0}^{z} dz\prime \left(\tan\theta_0 + (1-\sin^2\theta_0)^{-3/2}(\sin\theta(z\prime) - \sin\theta_0)\right) \\ x(z) - x_0 &= (z-z_0)\tan\theta_0 + (1-\sin^2\theta_0)^{-3/2}\rho(q/c)\int_{z_0}^{z}(\sin\theta(z\prime) - \sin\theta_0)\, dz\prime \\ x(z) - x_0 &= (z-z_0)\tan\theta_0 + (1-\sin^2\theta_0)^{-3/2}\rho(q/c)\int_{z_0}^{z}(\int_{z_0}^{z\prime} B(z\prime\prime)dz\prime\prime)dz\prime\end{aligned}$$

The spectrometer magnets were designed to be nearly constant over a finite z distance, and then to drop to zero outside of that volume. With knowledge of a particle's parameters before it reaches the magnet, and measurements of the magnetic field, the particle's position and direction of travel are known at any z position.

A.6.1 Parabolic motion approximation

If we assume that $(1 - \sin^2(\theta_0)) \rightarrow 1$, then the tangent angle and position change no longer depend on its initial angle, only linearly with the particle's charge and curvature. This model is the official SELEX trajectory used for the analysis pass.

There are two obvious reasons to use this calculation instead of the original. The first is speed. A great deal of the calculation and integration can be done beforehand and stored in a look up table. This also simplifies the fitting procedure, which would otherwise require non-linear solutions.

The other reason is the difficulty of getting a more accurate result. Any particle that requires a correction due to the value of the initial angle will likely have a small momentum. That will result in a large angle change from the magnet, and the Taylor expansion made will be increasingly inaccurate.

There are other corrections of about this magnitude which would also need to be done. After painstaking work, the alignment group determined that the magnet field had a few milliradian rotation compared to the y axis, well within the errors of the measuring instruments. That still fails to account for fringe fields, variation in the field as the particle travels farther away (in x and y) from the z-axis, variations in current to the magnets, and so on.

A.6.2 Momentum kick approximation

Next we can make the approximation that the magnetic field is a constant value B_y at any z inside the magnet, and zero outside. The angle and position formulas become

$$\begin{aligned} \sin\theta(z) - \sin\theta_0 &= \rho(q/c)B_y(z - z_0) \\ x(z) - x_0 &= (z - z_0)tan\theta_0 + \rho(q/c)B_y(z - z_0)^2 \end{aligned}$$

This was done early in the run, before a more accurate mapping of the magnetic fields was known. Although the results are too crude for mass reconstruction, it is still used in tracking, where it makes a quick tool to search for hits by projecting tracks through the magnets.

A.7 SELEX model

The MCS errors are vital for accurate tracking. As an example, the early embedding Monte Carlo used a gaussian distribution to simulate scattering

through the vertex silicon. The reconstructed mass resolution was smaller than real data for modes like K_s and the D mesons. By changing to a Moliere distribution, embedding more accurately simulates the actual mass resolution.

The vertex silicon hits are used to fit the track near the targets. Based on where we are trying to use track segment, MCS from the charm targets are included in calculating the errors. We also do a five parameter fit for the momentum and the x,y slopes and intercepts at the global coordinate origin. All hits for all track segments belonging to a track are used. The full covariant matrix is used for the vertex silicon, and the variances (based on finite wire spacing) are used for the wire chambers. The downstream LASD planes are treated as wire chambers, so the errors are inflated by a constant factor to account for MCS effects. In practice, the track direction and intercepts from the full fit are not as accurate as the vertex silicon fit alone, so the latter is used to minimize mass resolution.

There are two ways the experiment could be more accurate. The first is to do a refit of vertex segment for each target. The current model is to do a fit once for a point downstream of the targets, and calculate the errors for points within the charm target stack. This works in the model that MCS errors can be added in quadrature, but not if we use the more accurate MCS estimate. We assume that the corrections from the more accurate model are small, and the computing effort would be much greater.

The next change in the fits is to do the five parameter fit for a point downstream of the vertex silicon. Since the vertex track segment is used for position and direction, the five parameter fit only determines momentum, so this is the important quantity. In the current model, downstream pwc planes are measuring the track after MCS in the vertex silicon, not the track at the global origin. We would need to make a covariant matrix for every hit in the detector, even though we assume negligible MCS in the wire chambers. This would consume a lot of resources, due to the need to invert the larger covariant matrix. If the fit point is moved downstream of the vertex silicon, the problem goes away. Without any (significant) scattering material between the wire chambers and the fit point, we do not need to use a covariant matrix for those hits. The vertex silicon hits are on the other side of the fit point, and can be treated normally.

The problem with switching to this model is that a lot of effort was spent to make the analysis work for the existing fit model. The alignment of the planes and the magnetic field were adjusted to give the best results for track

fitting and reconstruction masses. Switching to another fitting model, even if it is more accurate in theory, would require optimizing the global alignment again, which is a non-trivial task.

Appendix B

Online filter

The online filter was designed to increase the amount of signal per event written to tape. The code is based on the complete offline analysis code. The trigger has the advantage of being very fast, but the trade off is only limited information is available to decide whether to keep or reject events. The filter runs the analysis code on triggered events, to allow more complex criteria. To reduce the processing time, only the systems necessary for the filter choices are turned on. Without the filter, it would have been necessary to scale back on the number of interactions, increase the trigger rejection (which would not discriminate between charm and non-charm events), or spend a lot of money to increase data storage and tape writing hardware.

Since SELEX was a complex and flexible detector, there were other triggers running beside the charm trigger. They will not be discussed in any great detail, other than the filter was also used for those triggers as well (figure B.1). Only the charm selection criteria will be mentioned, as it applies for this specific thesis.

B.1 Design philosophy

The charm trigger was designed to accept events that pass the following criteria:

- Single (beam) particle detected up through the beam spectrometer (scintillation and veto counters)

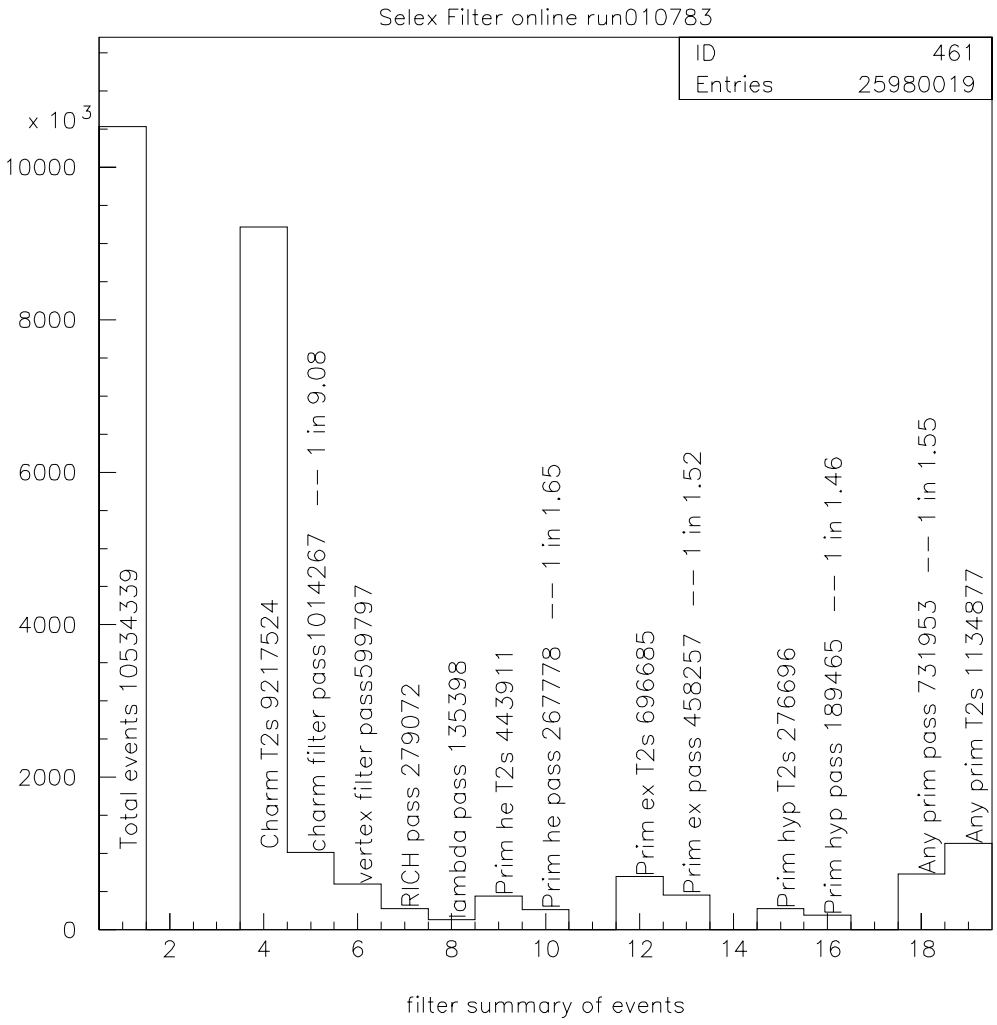

Figure B.1: Passed events from multiple filters.

- Three or more charged particles after the target stack (interaction counters)

- At least three high momentum particles (M2 hodoscopes)

- At least two positively charged high momentum particle (M2 hodoscopes)

The M2 hodoscopes should select for high x_F events. Since a charm quark has positive charge, requiring a particle in the positive half of the M2 hodoscope should provide some selection for charm. However, interactions that produce strange quarks will be a problem. For example, if an event has two neutral kaons that decay before the M2 magnets into a pair of π^+ and a pair of π^-, this will satisfy the hodoscope requirements. (In this example, the kaons will not fulfill the interaction counter requirement, but enough other particles are produced at the primary interaction that will hit the IC.)

The filter selection is based on the charm lifetime. The distance that the charmed hadron travels before decaying is on the order of a few millimeters to a few centimeters, depending on the relativistic speed and the particular charm lifetime. Particles produced from the charm decay will point to the secondary decay vertex, rather than the primary interaction vertex at the target. Peter Cooper estimated that these particles will miss the primary vertex by a transverse distance of $S \approx (\pi/2)c\tau$. The filter looks for a particle that reaches the M2 spectrometer that misses the primary vertex, with a transverse miss distance on the order of tens of microns. This will greatly suppress interactions that produce only stable light hadrons, which will have all tracks pointing to the primary vertex. A prompt decay by a strange hadron will satisfy the requirement, and the experiment easily sees K_s^0 and Λ_s^0. However, since their lifetimes are very long compared to charm, most of them will decay far enough downstream that they will not be noticed by the filter.

The next consideration is how much processing time is required to make the filter selection. The initial design was for 120K T2 (triggered) events during a 60 second spill. The SGI Challenge computer had 11 dedicated processors for the filter. (That number was later increased to 18.) The filter should be done in 55 seconds, to allow for any fluctuations in beam intensity (number of T2s) and maintainance needed for the computer. This allowed 5 milliseconds per event.

The last consideration was how many events should pass the filter. Passed events were kept on local disk, and copied to tape. The limitation was based on how quickly data could be written to tape. The filter rejection level was set to match (roughly) the tape writing speed, and was on the order of one event in seven.

The filter turned out to have a correlation between processing time and rejection level, so passing more events increases time. The constraints also changed during the run. At the start of the data run, while the hardware performance was still being optimized, SELEX ran with 80K T2 events per spill and 11 processors. By the end of the run, there were 120K T2s and 17 processors.

B.2 Filter design

The filter was designed to be fast enough to run during a spill cycle, and to reject events that are not likely to have charm. The code does a full reconstruction for high momentum tracks in the event. The filter checks the event as various stages of the online analysis, and will stop if a criteria is not met (figure B.2). The tests, in order, are listed next.

- Too many hits in the detector. If the number of hits in the beam silicon, vertex silicon, or M2 PWC are above an adjustable threshold, the event is rejected. This is done for two reasons. A study by Kushnirenko has shown that the processing time for the M2 chamber is proportional to the number of hits raised to a power. [17] This is observationally true for the beam and vertex chambers as well. Events with too many hits consume too much time. The second reason is tracking confusion. Events with this many hits are more likely to fail the filter at a later stage, as the tracking algorithms start to make mistakes in assigning hits.

- Beam track selection. To do accurate primary vertex finding and vertex silicon tracking, we need one and only one interacting beam track. Since the beam silicon integrates charge, out-of-time beam track information is often present. If more than one beam track is present, the filter tries to chose which one should be used for the triggered event.

The HST silicon does have a short gate, so if a beam silicon track extrapolates to hits in the HST system, that track is chosen. If that fails, the code attempts to extrapolate the beam track into the vertex silicon. Non-interacting beam particles should show up as a straight line through both detectors. If that also fails to find a unique choice, we count the hits in the vertex silicon in a cone, based on the beam track position. An interaction should send out a spray of particles starting at the end of the beam track, which will mean more hits in the cone.

- M2 tracking. To speed up tracking, the filter should only consider high momentum tracks. This will help to select high x_F events, and the search algorithms are simplified. Tracking starts with trying to find M2 segments. This is also a cross check of the trigger, that the M2 hodoscope hits came from reconstructible tracks.

- Vertex silicon tracking. The M2 tracks are extrapolated into the vertex silicon, and the code tries to find a vertex segment that will match the M2 segment. The vertex silicon environment is very complex, so only considering tracks that reach M2 simplifies the situation. Also, high momentum tracks will have less multiple coulomb scattering, which should make it easier to fit.

- Miss distance at the primary vertex. Assuming that the event passed the tracking requirements for the M2 and VX spectrometers, those tracks and the beam tracks are used to find the primary interaction vertex at one of the charm targets. If all tracks are consistent with the primary vertex, the event fails. Early in the run, the test was based on the transverse (x, y) miss distance of the tracks from the primary vertex, with a large miss distance for a track making the event pass the filter. Later, that was changed to an error weighted selection that was done in the primary vertex fitting code. If the primary vertex fitter rejected a track, the event passed (figure B.3).

As the experiment progressed, other selections were added. If the event survived passed tracking, the particle identification code was run. Events

could pass the filter if the code found protons or kaon tracks, consistent with charm decay.

B.3 Problems encountered

This section is a list of the major problems encountered during the creation of the SELEX filter. The first was string comparisons in the code. To control the program flow (without having to recompile the source code), SOAP reads a text file with a list of commands and cuts. The code loaded the command file into memory, and would loop over the commands for each event analyzed. The first version of the code kept the lines in character string form, which meant the computer spent a lot of time doing string comparisons. The string comparisons were moved to the initialization stage, when the command file was read in, and integers assigned for each command. SOAP would then loop over the list of integers to control the program flow, with integer comparisons running much quicker than character strings. This was the most obvious code change that improved timing without any other effect on the analysis.

The number of hits in the M2 chamber were a lot more than anticipated from early Monte Carlo studies. To keep the processing time under control, the maximum hit cut was applied. The cut was adjusted to accept as many events as possible in the allowed time. This cut was loosened by improvements in the M2 tracking code, and when the computing division increased the number of computer processors from 11 to 18.

The M2 cut was a concern, as those events might have a different abundance of charm. After a certain level, too many hits prevent accurate tracking even in the offline environment. For events just above the multiplicity cut, the Kushnirenko study showed that those events had the same amount of charm (and not more) than the rest of the events that passed the filter. This was based on the unfiltered events being processed offline for the basic charm states (D mesons and the Λ_c baryon).

The SELEX computing style was to keep the code in separated modules. This allowed different groups to modify their code with minimum interference with other code changes. This was not possible for the filter. The first version ran the entire analysis package before making a decision, which meant wasted time for events that fail early in the decision chain. The filter was integrated in the unpacking, tracking, and vertexing packages, to allow the code to stop as soon as the filter decides to reject an event.

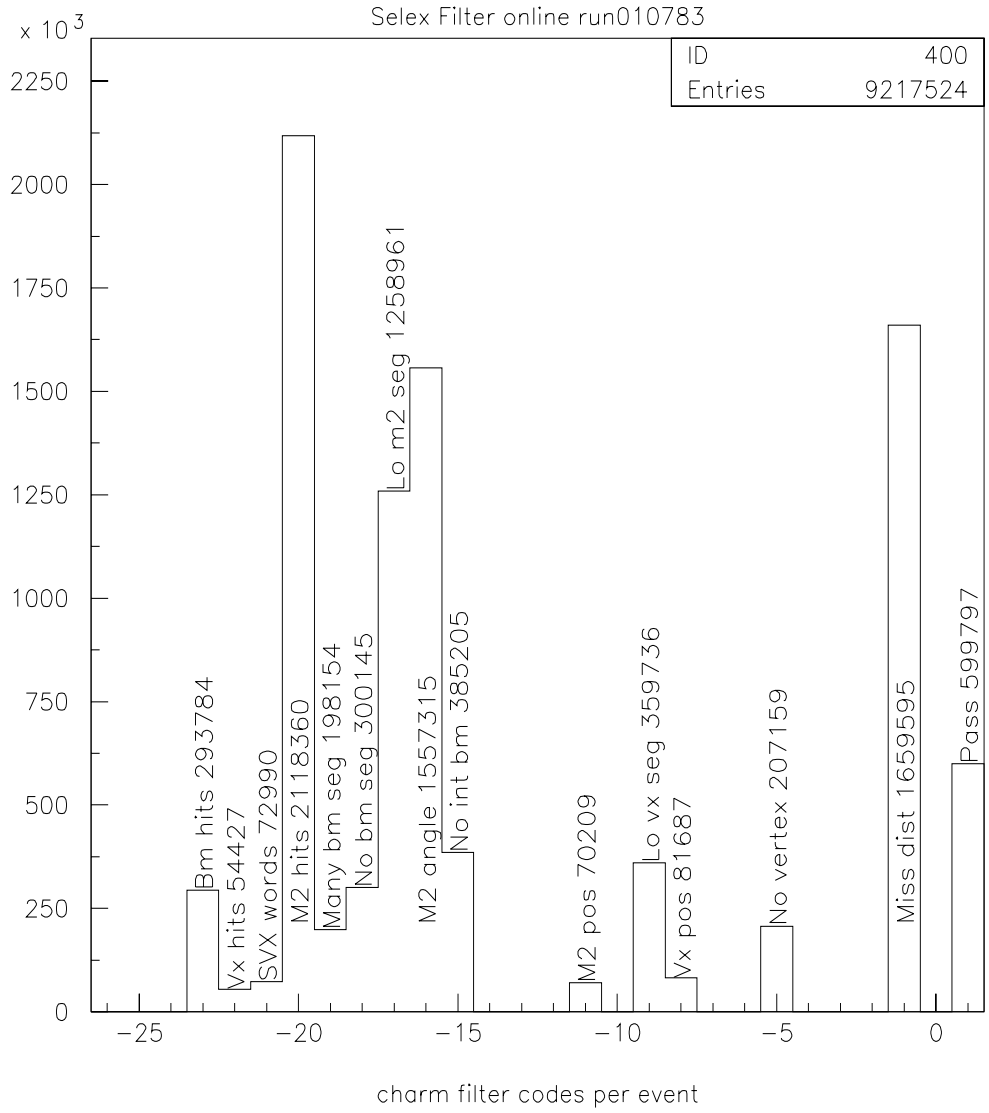

Figure B.2: Charm filter fail codes.

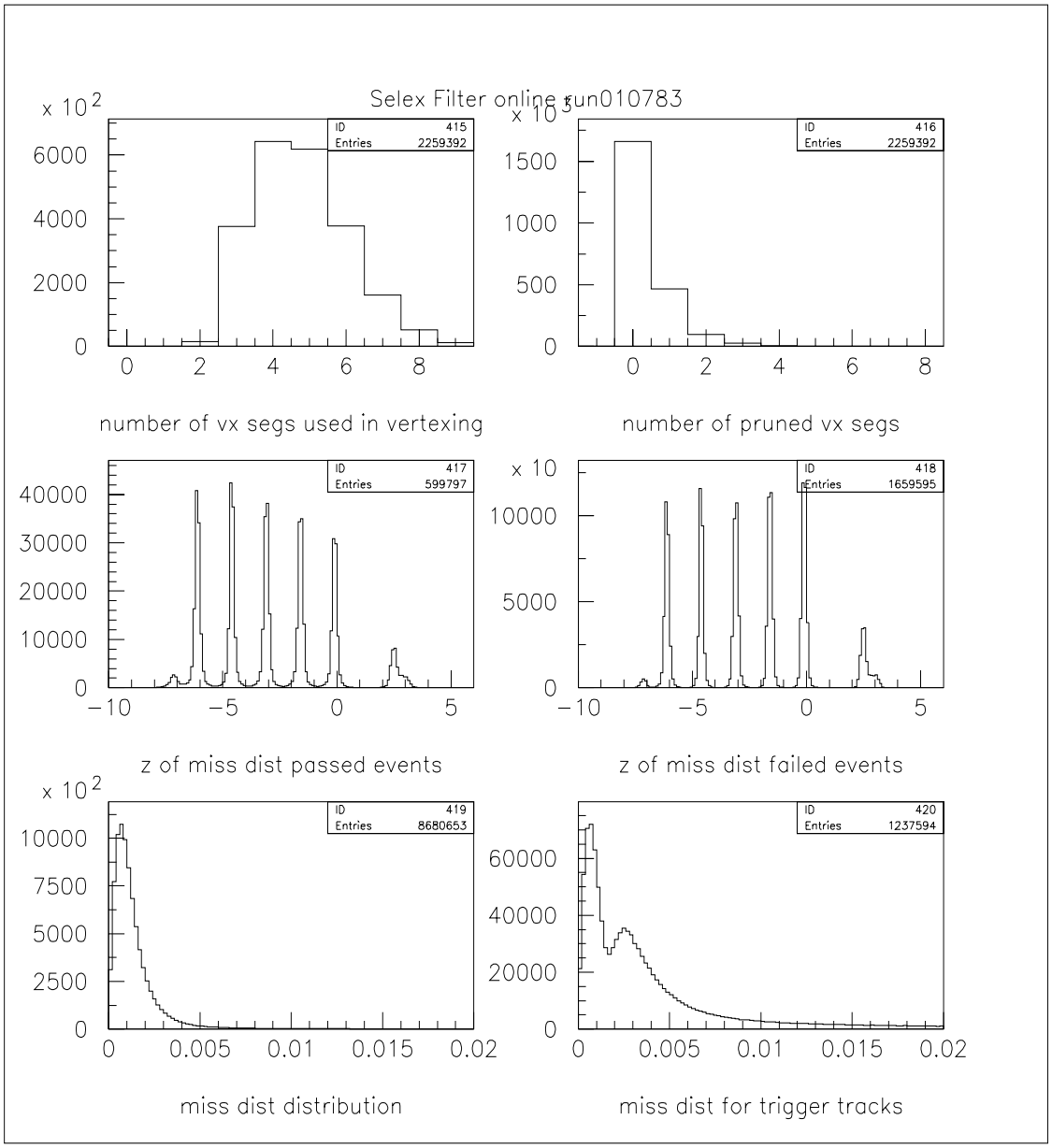

Figure B.3: Filter vertex performance.

The filter was built from the full offline package, so that code improvements would be automatically included in the online version. This also allowed us to model timing and performance offline. This caused a problem as the code grew larger. The parts of the filter executable were being swapped into and out of processor memory, which caused an incredible time delay. The solution was to excise SOAP routines that were not being used, as compile time. The filter versions that were used online are still available, but since the Monte Carlo sections were removed, we could not use embedding to check the filter performance. The offline and online code comes from the same source, so we can try to build an offline version that models the online code. The problem is that the code has changed enough that it is difficult to make a SOAP version today that is the same as the filter version from years ago.

Since the miss distance depends on accurate tracking, the filter needed to be given reasonable alignment tables for the detectors. In practice, the alignment was stable enough that the tables only needed to be updated about once a week. There was almost no change in performance on the scale of a day, and reduced performance if the same tables were used for a month.

B.4 Notes about filter performance

Offline studies showed that the online filter program was approximately equivalent to the cut $L/\sigma_L > 3$.

The filter proved to be a valuable monitor of detector performance, since it was doing analysis code at runtime. Inaccurate thresholds in the silicon, for example, might not show up in the monitoring plots of the detector hits. It will show up in the filter, when the rejection rate goes up. Figure B.4 shows that the filter was remarkable stable over the course of the entire data taking, despite changes in constants, cuts, and code.

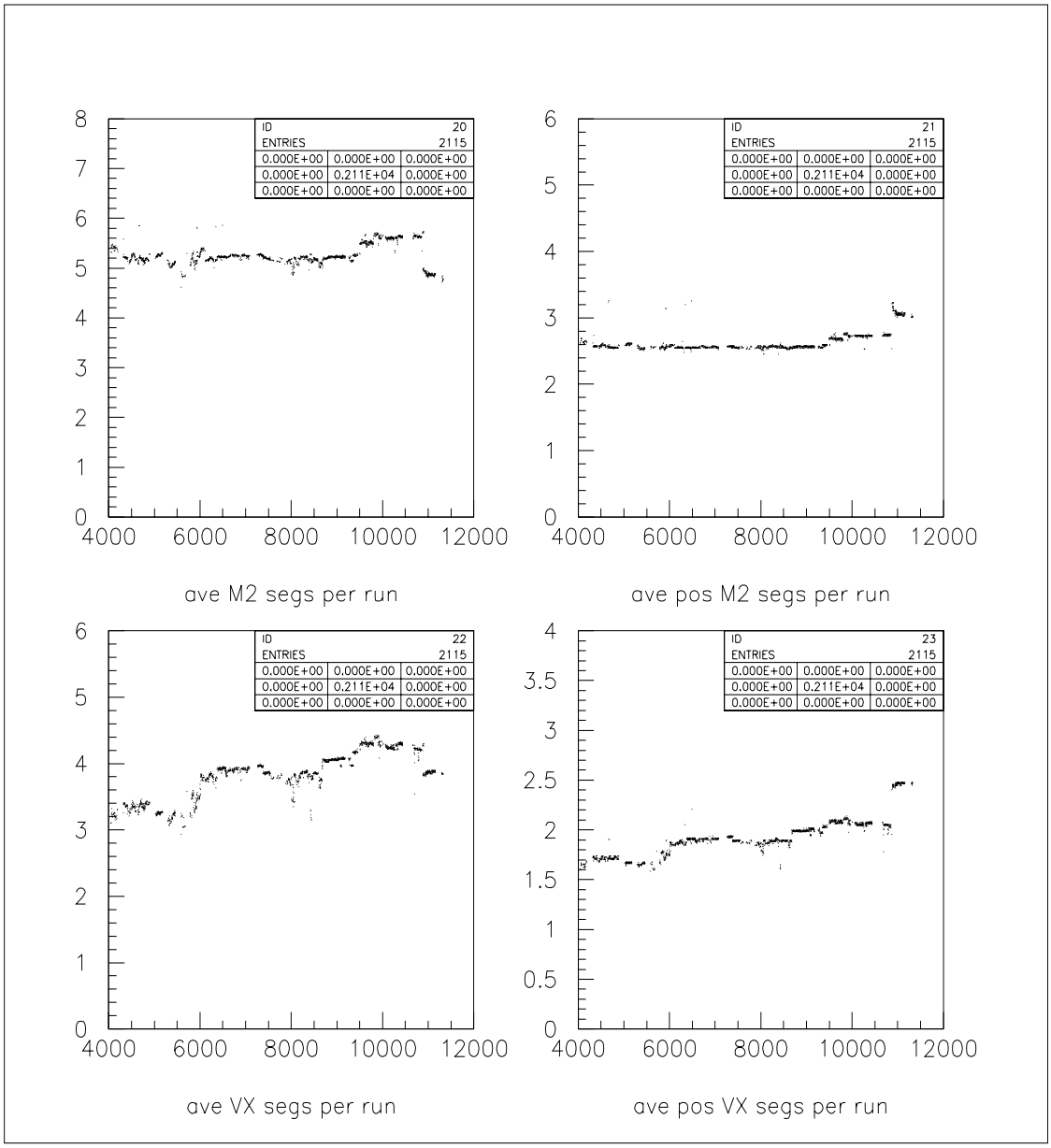

Figure B.4: Filter stability over time. These show the average number of track segments per event per run found by the filter. This is the number found before the filter applies the tracking requirements; the average number of segments in events written to tape is higher. The graphs are flat, except for when the M2 hit cut was changed from 150 to 200, and the positive beam data at the end of the run.

Appendix C

Kinematic variables for embedding and real data

Eighteen variables were checked for the embedded Λ_c sample (Figures C.1 - C.6), the embedded Ξ_{cc} sample (Figures C.7 - C.12), and for the real data sample (Figures C.13 - C.18). We are looking at the Λ_c, Ξ_{cc} sidebands, and real sidebands to see the background behavior. The Ξ_{cc} sideband-subtracted signal will simulate the desired events. We might expect to see differences involving the kaon or pion tracks in the $K\pi\pi$ vertex, as we are examining three different groups: "signal" embedded tracks from the Ξ_{cc}, random real tracks uncorrelated with the embedded Λ_c, and tracks from real data. The source of the background might have been concentrated in a different region of phase space than signal. The different samples look very similar, and are presented for the "experts".

During the survey, we also need to keep in mind the limitations of embedding. The x_F distribution will definitely be wrong for Λ_c sample, since the event will have more energy (the event, plus the embedded tracks) than the initial beam particle. Also, guesses were made for the x_F and p_t distributions. Variations between signal and background need to be checked if the effects are real, or arising from having the wrong embedded distribution.

All the reconstructions have the minimum bias cuts applied. The signal and sidebands are based on the mass of the $\Lambda_c K^-\pi^+\pi^+$ reconstruction candidates. For the embedded Λ_c file, the left is for the sideband region, the right side is the signal region. For the embedded Ξ_{cc} file, the left is sideband, the right is sideband-subtracted signal. The real data is also set up this way. The signal region is a mass window 75 MeV wide, centered at the expected

mass of 3.760 GeV/c^2. The sidebands are two mass windows covering events with a mass 52.5 to 90 MeV away from the expected mass. For the embedded files, the expected mass is then generated value of 3.785 GeV.

Below we list the definitions of the observed quantities. The kaon and pions refer to the $K\pi\pi$ vertex, and not the kaon and pion used for the Λ_c reconstruction.

- Top page 1 - Kaon track χ^2, based on the comparing the hits used from the tracking fit parameters.

- Middle page 1 - Pion 1 track χ^2, based on the comparing the hits used from the tracking fit parameters.

- Bottom page 1 - Pion 2 track χ^2, based on the comparing the hits used from the tracking fit parameters.

- Top page 2 - Kaon momentum in the z direction.

- Middle page 2 - Pion 1 momentum in the z direction.

- Bottom page 2 - Pion 2 momentum in the z direction.

- Top page 3 - Largest scut value, for the kaon and two pion tracks.

- Middle page 3 - Middle scut value, for the kaon and two pion tracks.

- Bottom page 3 - Smallest scut value, for the kaon and two pion tracks.

- Top page 4 - Ξ_{cc} candidate z momentum divided by beam z momentum (x_F).

- Middle page 4 - p_t of Ξ_{cc} compared to beam track.

- Bottom page 4 - Pointback of Ξ_{cc} to primary vertex.

- Top page 5 - Λ_c z momentum divided by Ξ_{cc} candidate z momentum.
- Middle page 5 - Pointback of Λ_c to Ξ_{cc}.
- Bottom page 5 - Vertex χ^2 for $K\pi\pi$.
- Top page 6 - L/σ for $K\pi\pi$ to primary.
- Middle page 6 - L/σ for Λ_c to $K\pi\pi$.
- Bottom page 6 - L/σ for Λ to its primary. This is the primary vertex from the original Λ_c candidate, which may or may not include tracks from the $K\pi\pi$ vertex.

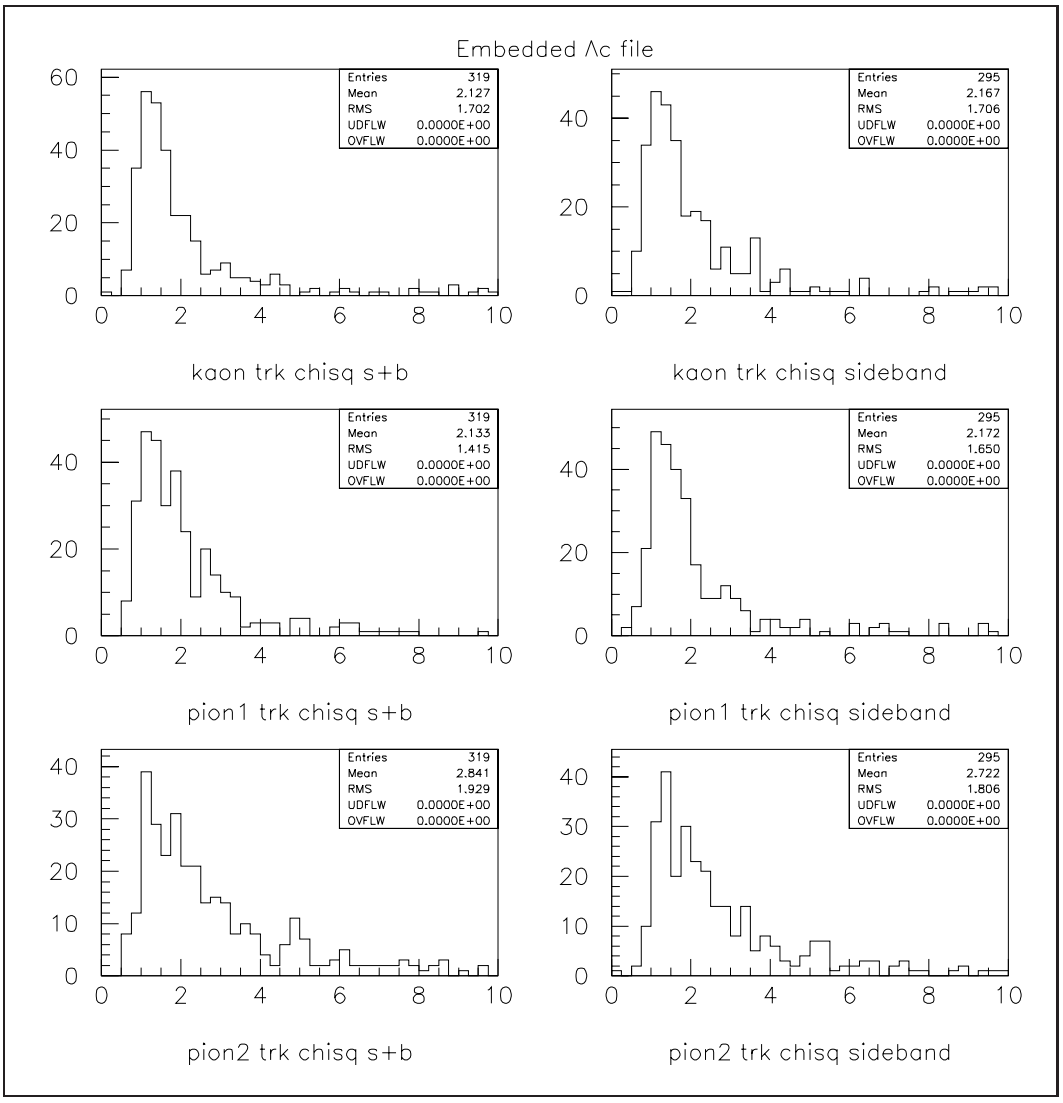

Figure C.1: Track χ^2 for embedded Λ_c. page 1 of variable list.

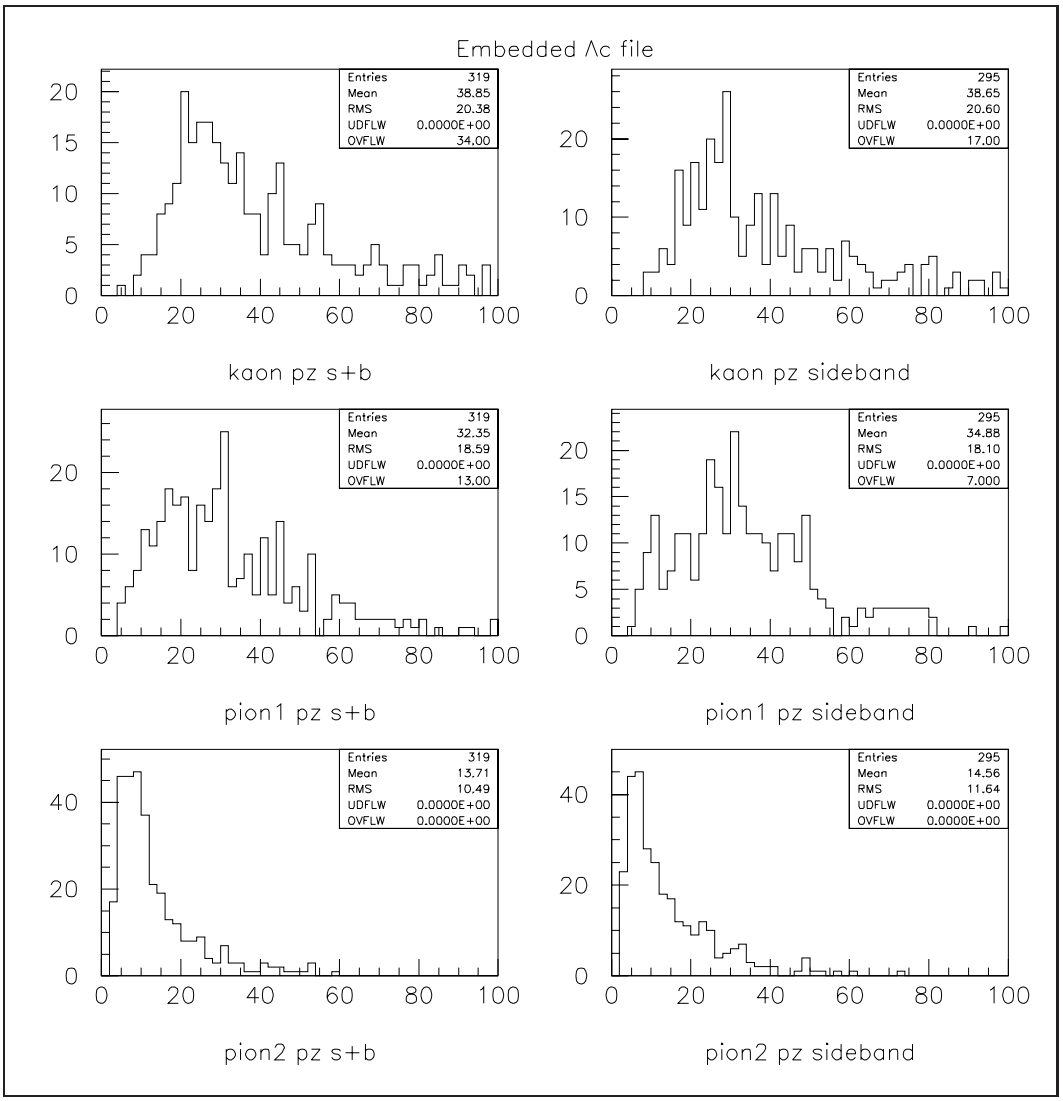

Figure C.2: Track z momentum for embedded Λ_c. Page 2 of variable list.

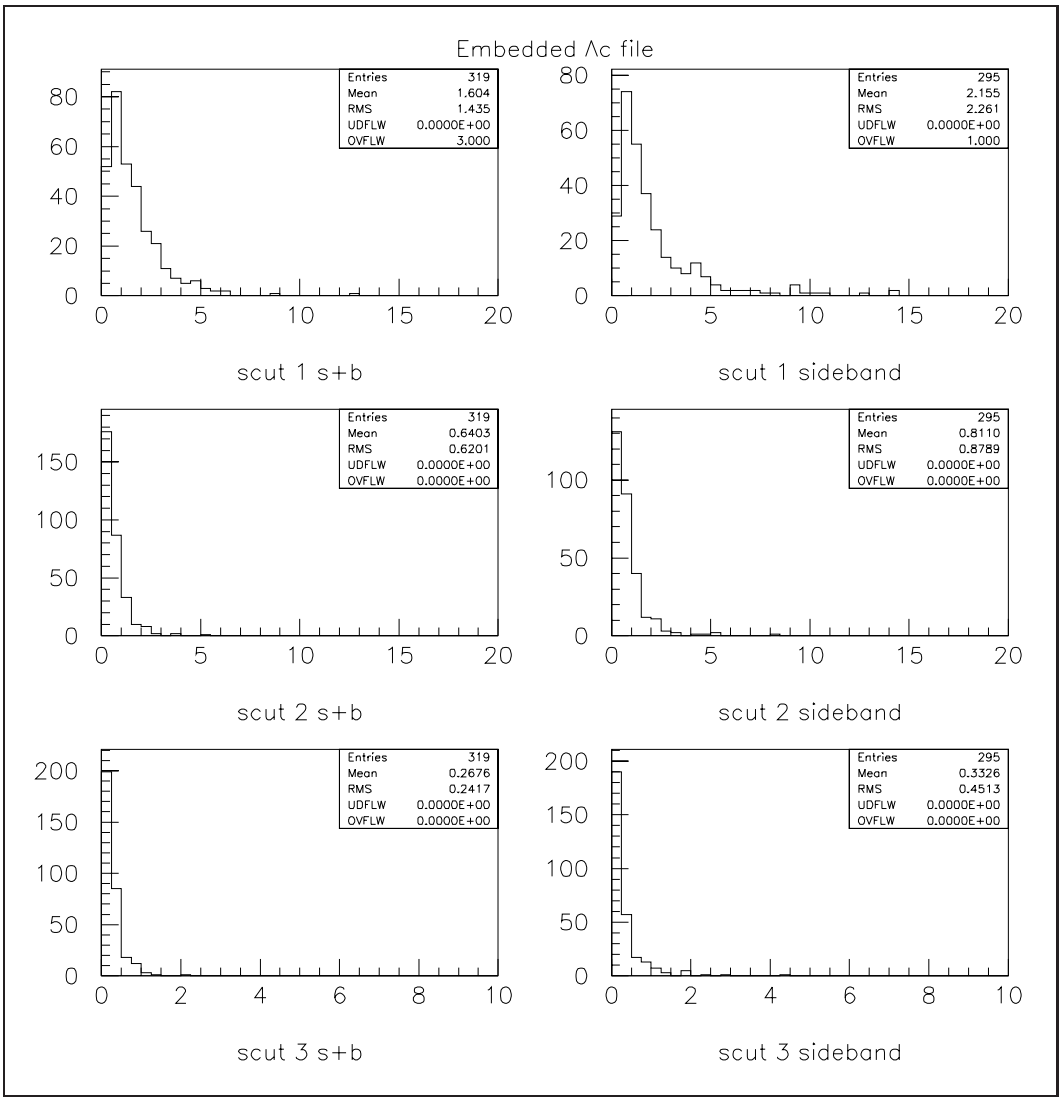

Figure C.3: Value of scut for embedded Λ_c. Page 3 of variable list.

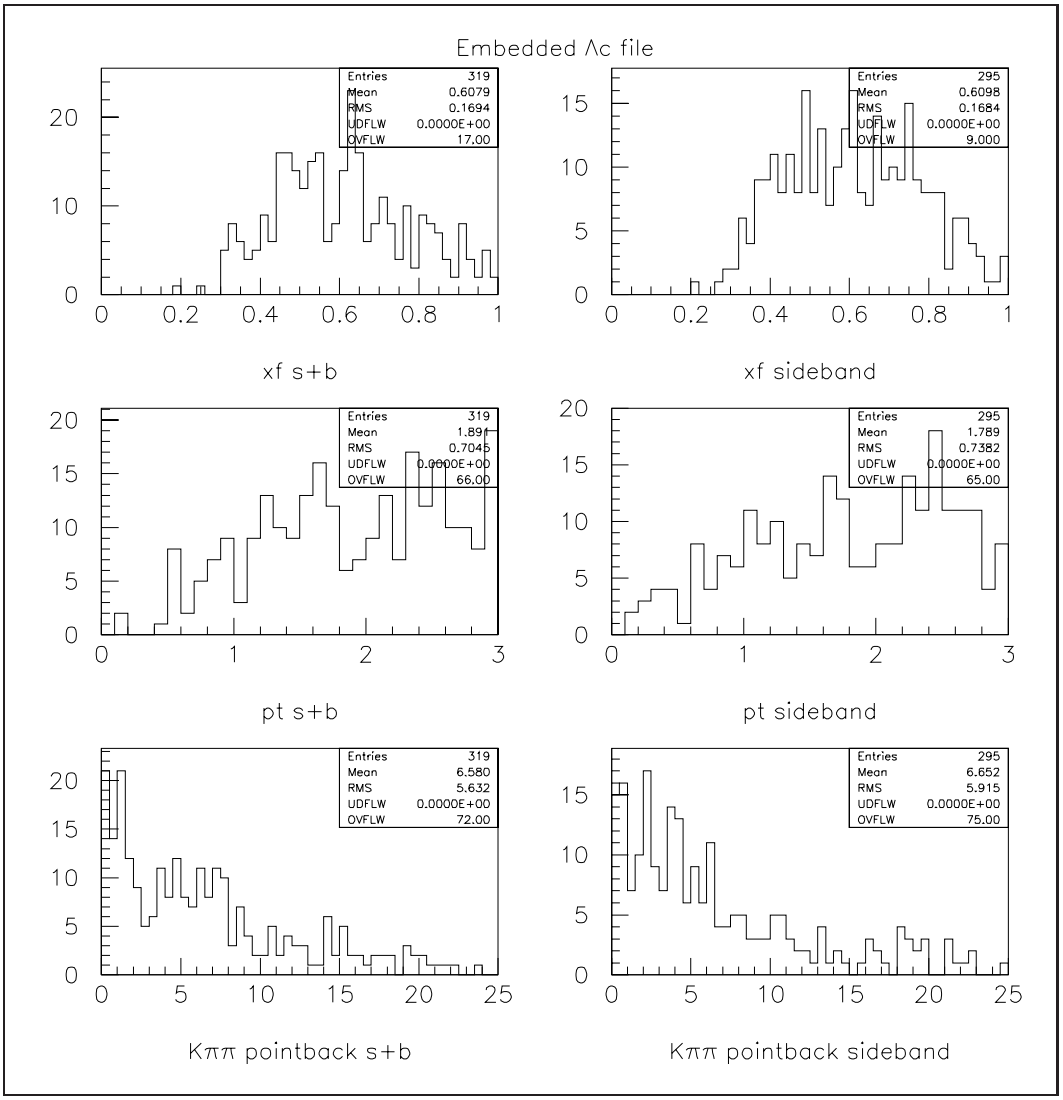

Figure C.4: Comparisons with beam for embedded Λ_c. Page 4 of variable list.

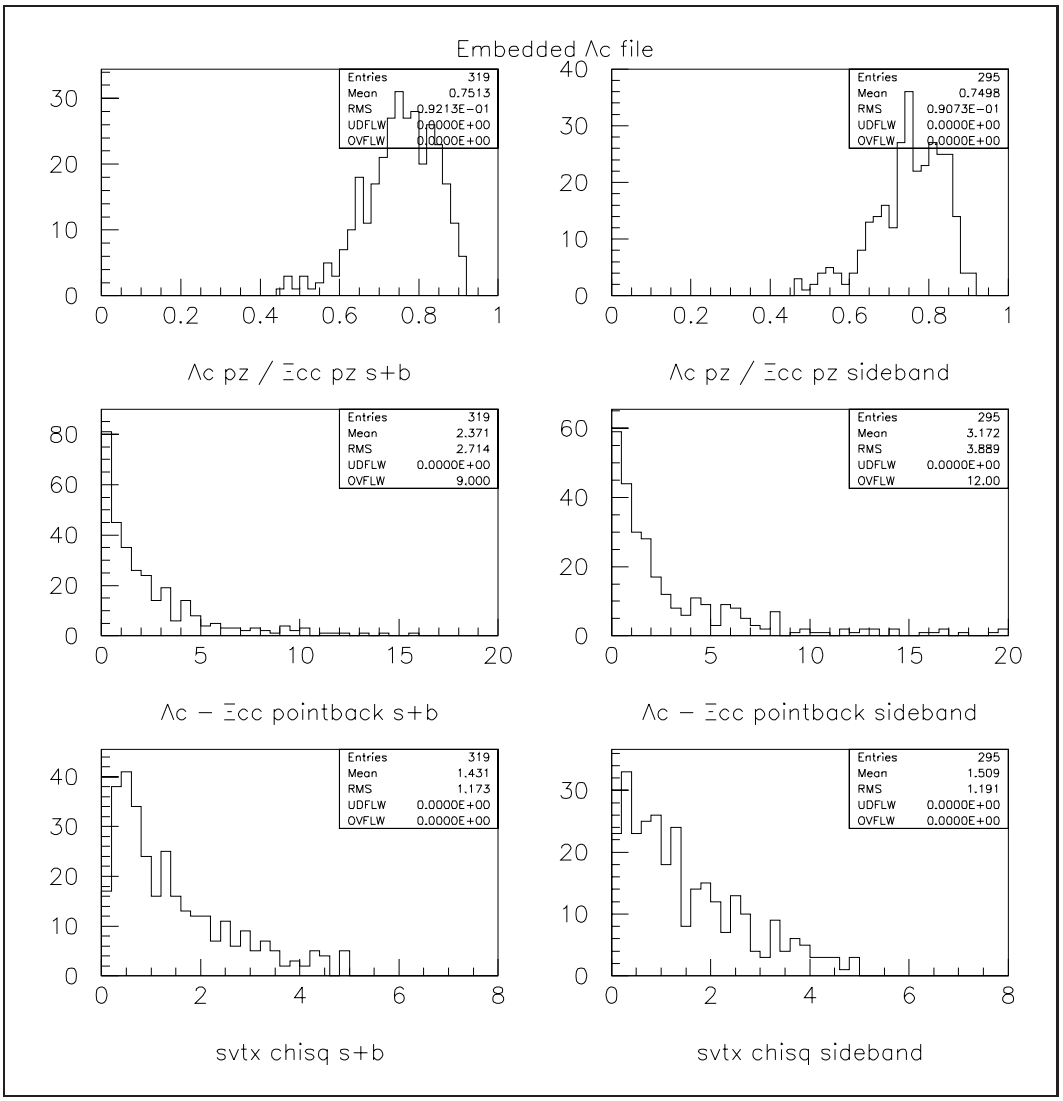

Figure C.5: $K\pi\pi$ comparisons for embedded Λ_c. Page 5 of variable list.

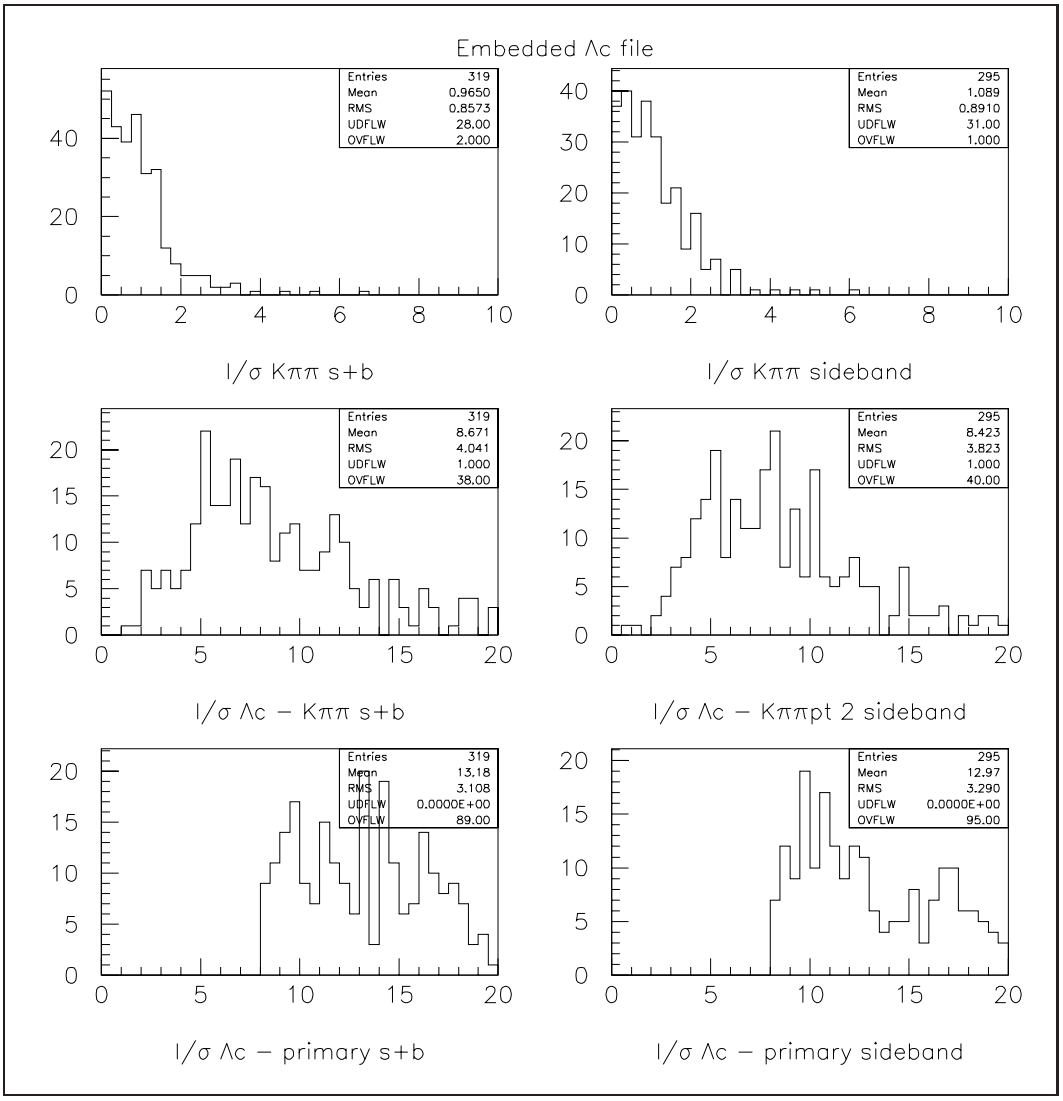

Figure C.6: L/σ for embedded Λ_c. Page 6 of variable list.

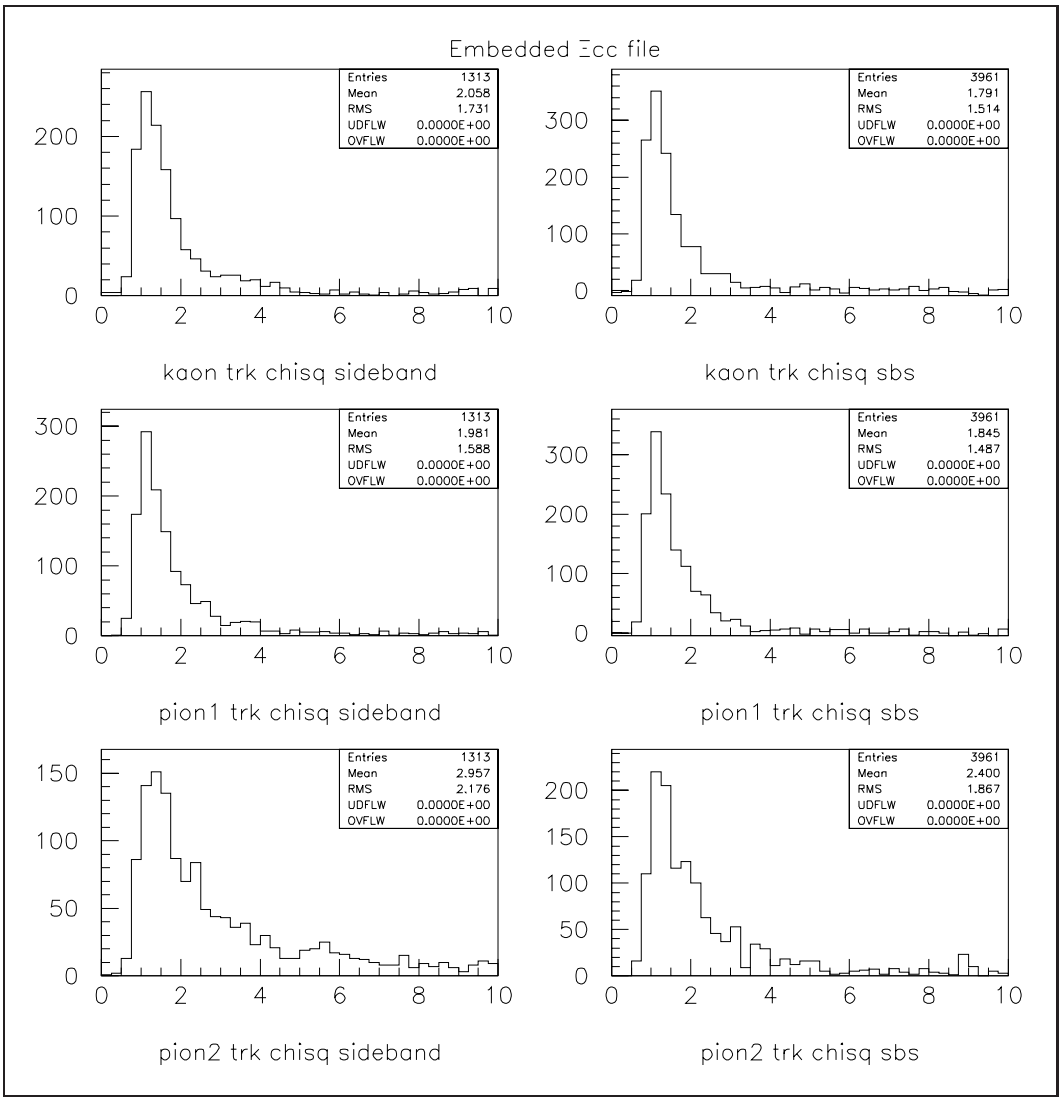

Figure C.7: Track χ^2 for embedded Ξ_{cc}. page 1 of variable list.

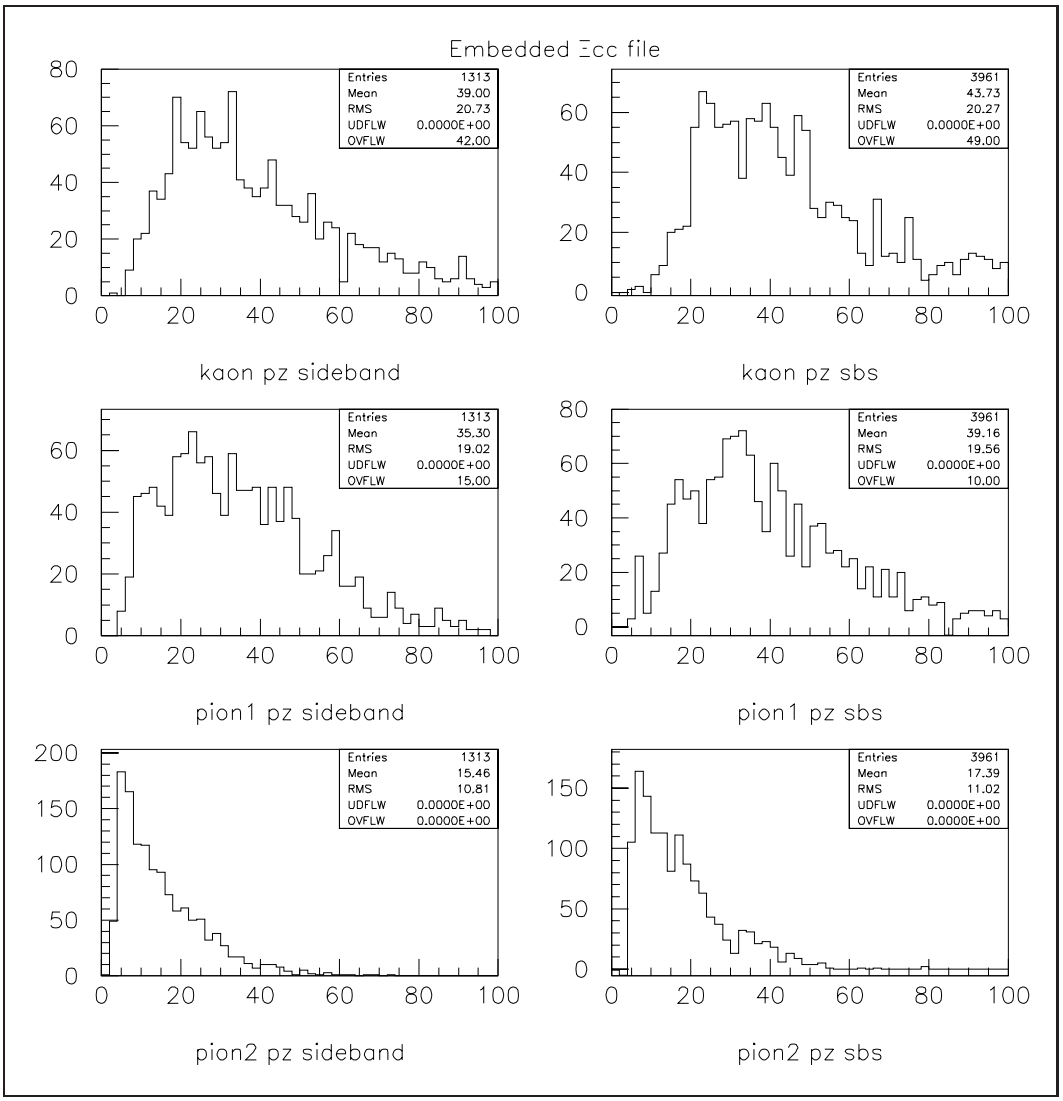

Figure C.8: Track z momentum for embedded Ξ_{cc}. Page 2 of variable list.

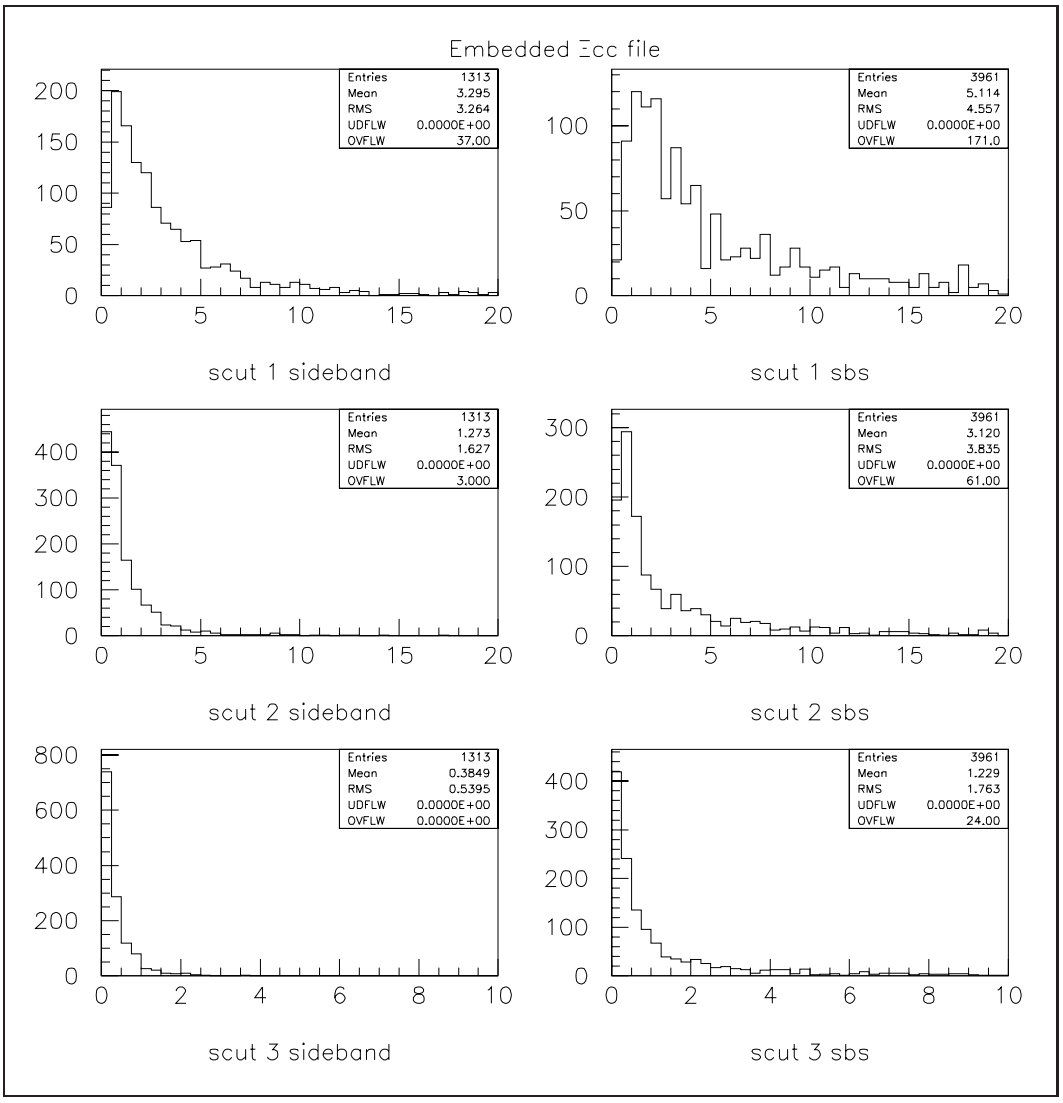

Figure C.9: Value of scut for embedded Ξ_{cc}. Page 3 of variable list.

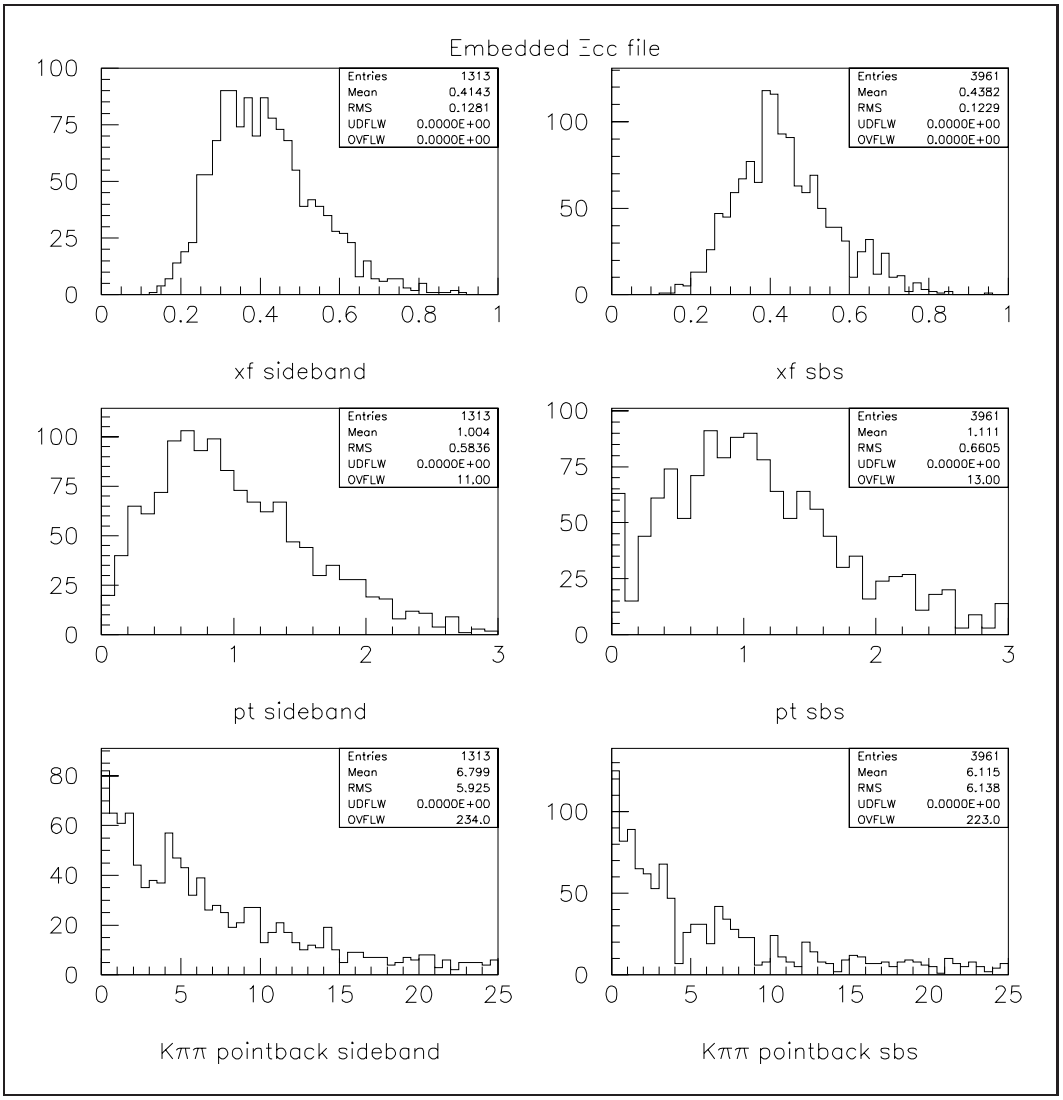

Figure C.10: Comparisons with beam for embedded Ξ_{cc}. Page 4 of variable list.

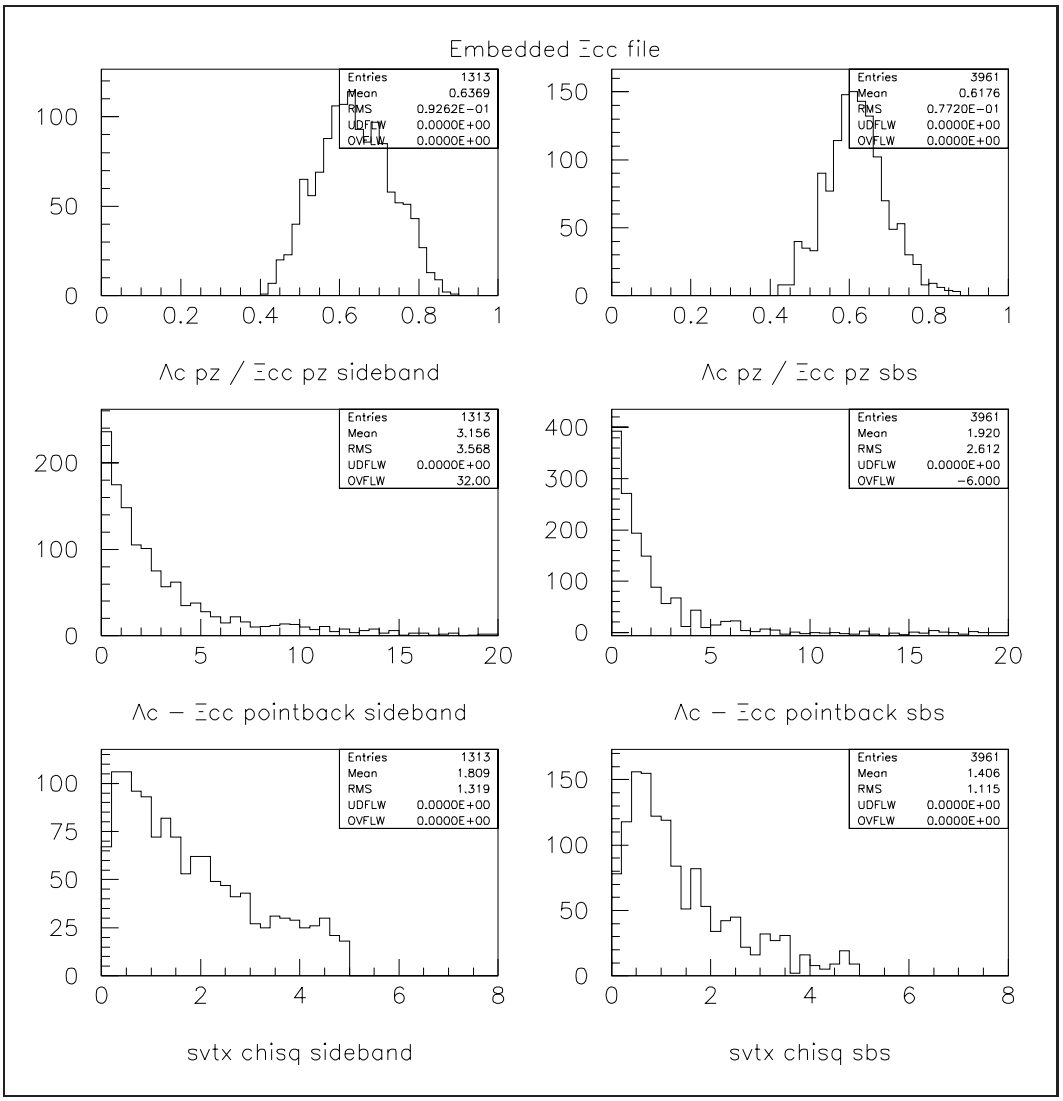

Figure C.11: $K\pi\pi$ comparisons for embedded Ξ_{cc}. Page 5 of variable list.

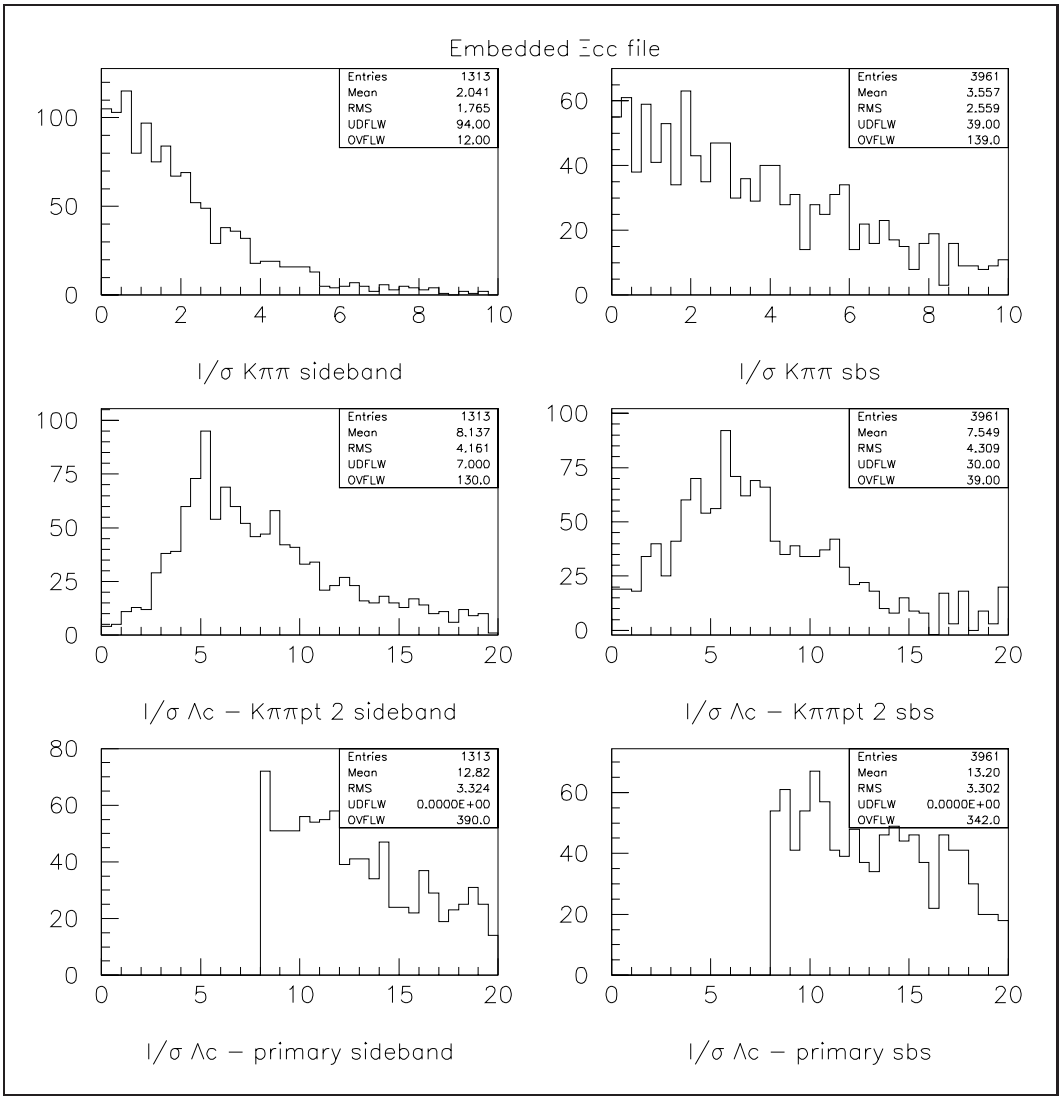

Figure C.12: L/σ for embedded Ξ_{cc}. Page 6 of variable list.

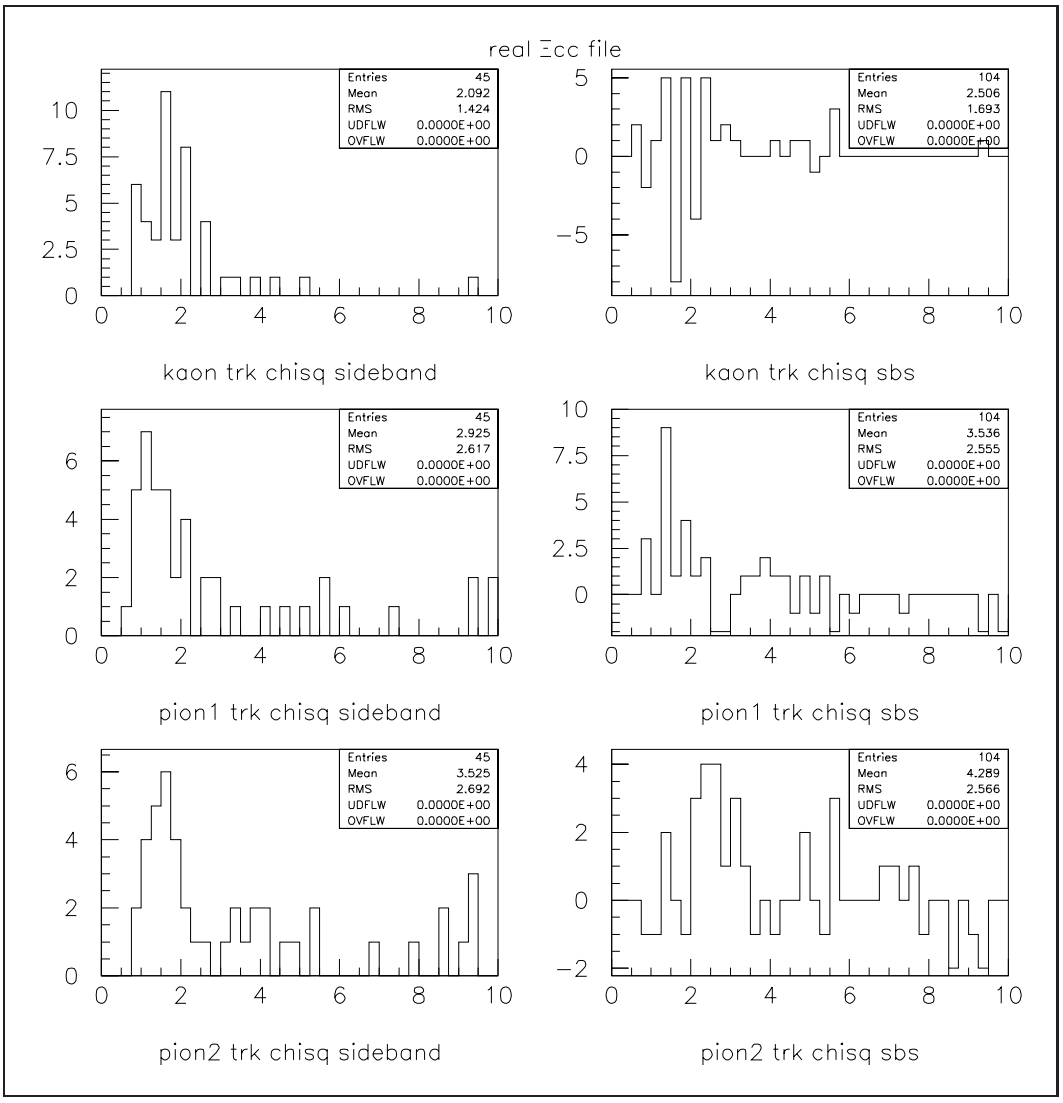

Figure C.13: Track χ^2 for real data. page 1 of variable list.

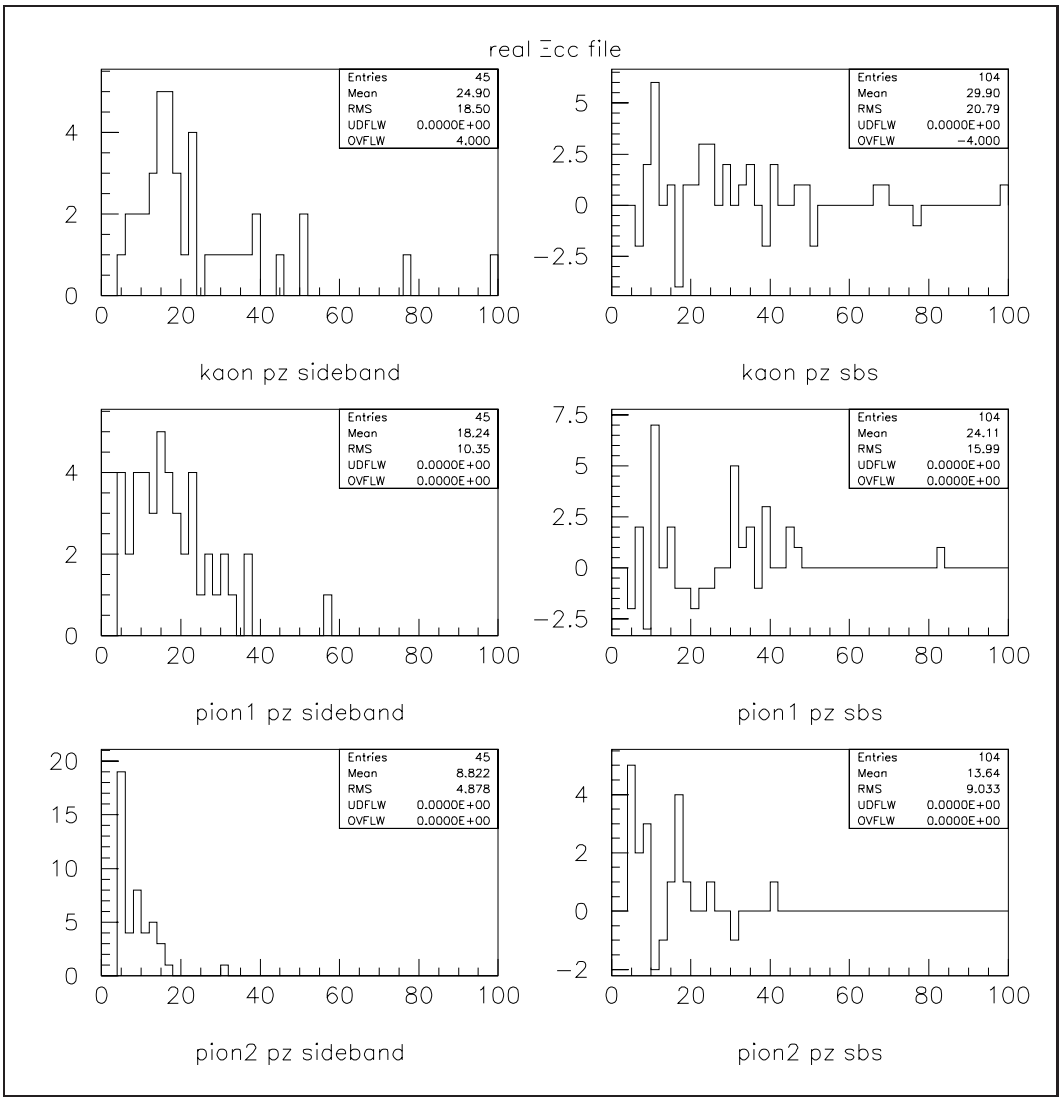

Figure C.14: Track z momentum for real data. Page 2 of variable list.

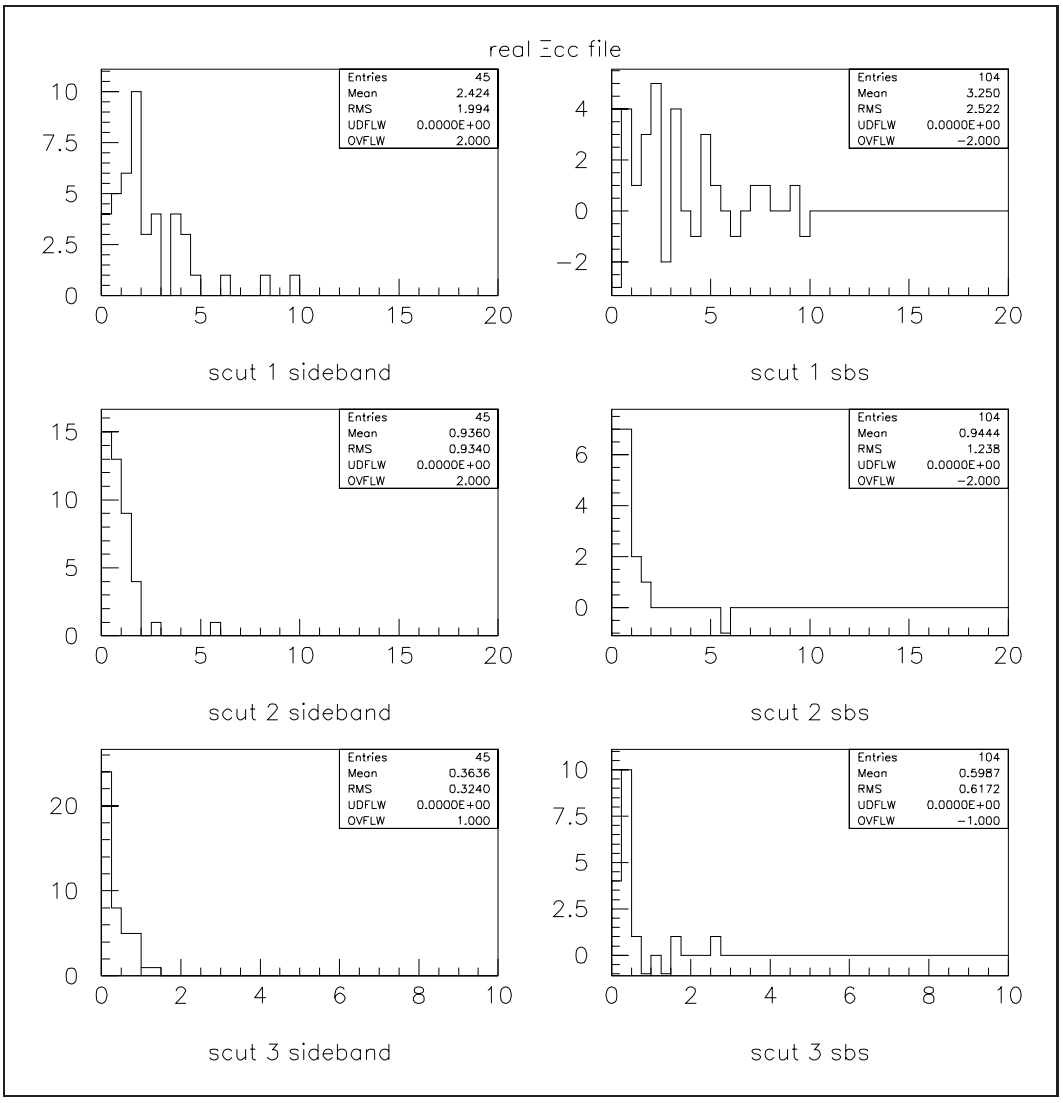

Figure C.15: Value of scut for real data. Page 3 of variable list.

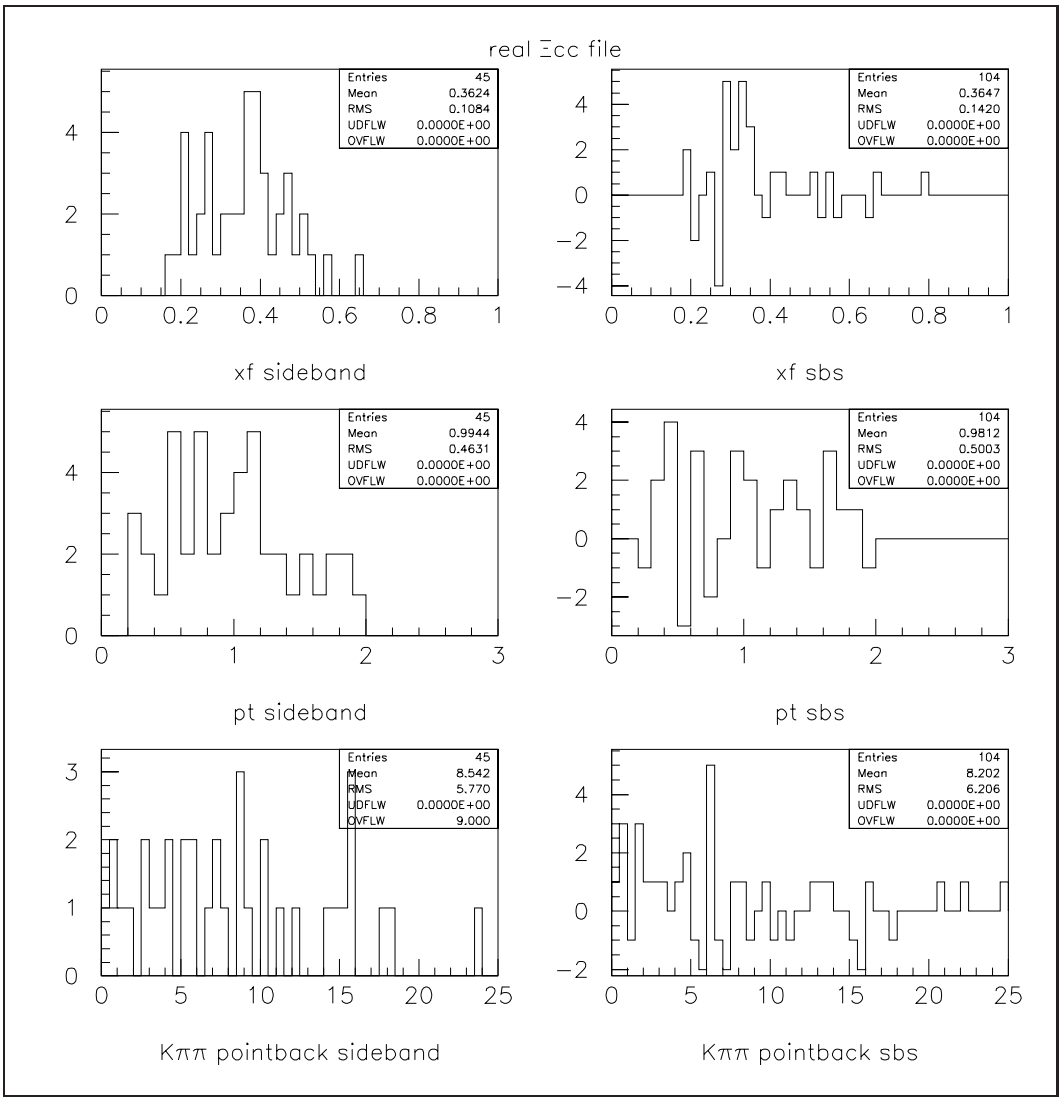

Figure C.16: Comparisons with beam for real data. Page 4 of variable list.

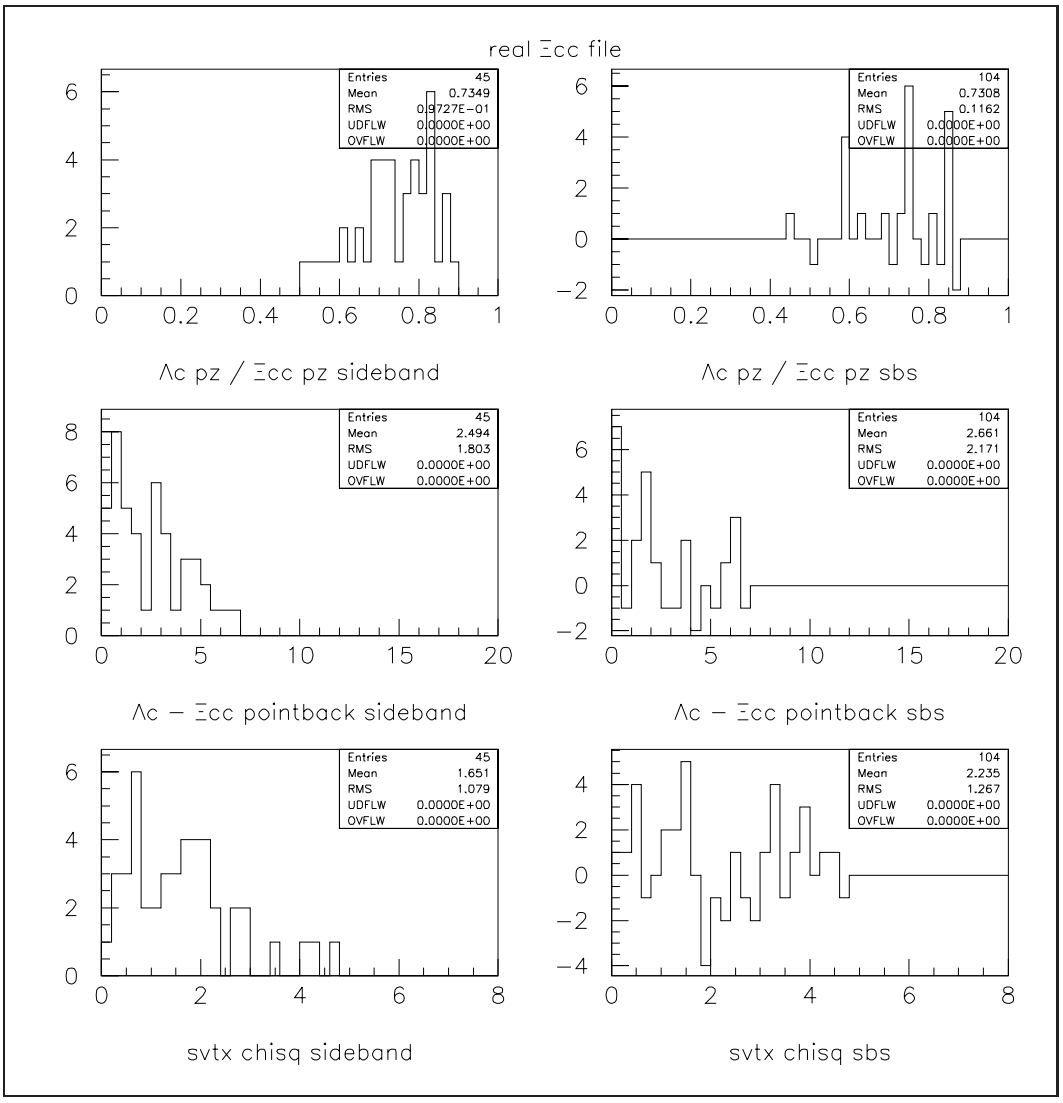

Figure C.17: $K\pi\pi$ comparisons for real data. Page 5 of variable list.

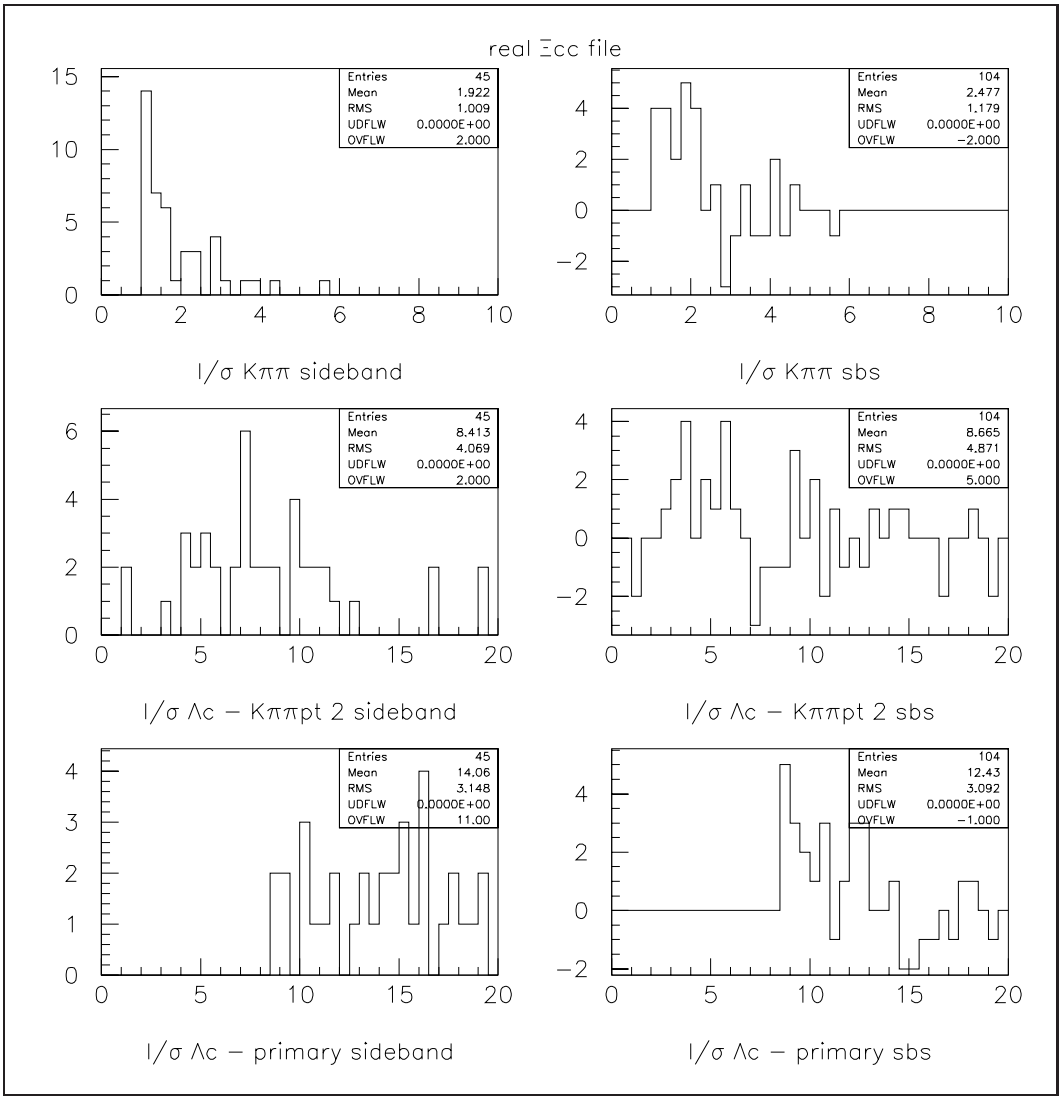

Figure C.18: L/σ for real data. Page 6 of variable list.

Bibliography

[1] T.-P. Cheng and L.-F. Li, *Gauge theory of elementary particle physics*. Oxford University Press, 1984, 1992.

[2] D. E. G. et al, "Review of Particle Physics," *The European Phys. Journal* **C15** (2000) 1+.

[3] M. J. Savage and M. B. Wise, "Spectrum of baryons with two heavy quarks," *Phys. Lett.* **B248** (1990) 177–180.

[4] P. Cooper, J. Grunhaus, and J. Russ, "Search for Doubly Charmed Baryons Using 600 GeV/c Hyperon and Pion Beams," H-Note 718, SELEX Internal Report, 1994.

[5] M. A. Moinester, "How to search for doubly charmed baryons and tetraquarks," *Z. Phys.* **A355** (1996) 349–362, `hep-ph/9506405`.

[6] J. D. Bjorken, "IS THE CCC A NEW DEAL FOR BARYON SPECTROSCOPY?," *Submitted to Int. Conf. on Hadron Spectroscopy, College Park, MD, Apr 20-22* (1985).

[7] A. DeRujula, H. Georgi, and S. Glashow, "Hadron masses in a gauge theory," *Phys. Rev.* **D12** (1975) 147–161.

[8] C. Itoh, T. Minamikawa, K. Miura, and T. Watanabe, "Doubly charmed baryon masses and quark wave functions in baryons," *Phys. Rev.* **D61** (2000) 057502.

[9] R. Lewis, N. Mathur, and R. M. Woloshyn, "Charmed baryons in lattice QCD," *Phys. Rev.* **D64** (2001) 094509, `hep-ph/0107037`.

[10] D. Ebert, R. N. Faustov, V. O. Galkin, and A. P. Martynenko, "Mass spectra of doubly heavy baryons in the relativistic quark model," hep-ph/0201217.

[11] V. V. Kiselev and A. K. Likhoded, "Baryons with two heavy quarks," hep-ph/0103169.

[12] S.-P. Tong *et al.*, "Spectra of baryons containing two heavy quarks in potential model," *Phys. Rev.* **D62** (2000) 054024, hep-ph/9910259.

[13] R. Roncaglia, D. B. Lichtenberg, and E. Predazzi, "Predicting the masses of baryons containing one or two heavy quarks," *Phys. Rev.* **D52** (1995) 1722–1725, hep-ph/9502251.

[14] D. Ebert, V. O. Galkin, and R. N. Faustov, "Mass spectrum of orbitally and radially excited heavy-light mesons in the relativistic quark model," *Phys. Rev.* **D57** (1998) 5663–5669, hep-ph/9712318.

[15] J. Körner, M. Krämer, and D. Pirjol, "Heavy baryons," *Prog. Part. Nucl. Phys.* **33** (1994) 787–868, hep-ph/9406359.

[16] H. Kaur and M. P. Khanna, "Masses of heavy hadrons," hep-ph/0005077.

[17] A. Kushnirenko, *Precision measurements of the* Λ_c^+ *and* D^0 *lifetimes*. PhD thesis, Dept. of Physics, Carnegie Mellon University, 2000.

[18] V. V. Kiselev, A. K. Likhoded, and A. I. Onishchenko, "Lifetimes of doubly charmed baryons: Xi/cc+ and Xi/cc++," *Phys. Rev.* **D60** (1999) 014007, hep-ph/9807354.

[19] S. Aoki *et al.*, "THE DOUBLE ASSOCIATED PRODUCTION OF CHARMED PARTICLES BY THE INTERACTION OF 350-GeV/c pi- MESONS WITH EMULSION NUCLEI," *Phys. Lett.* **187B** (1987) 185.

[20] **NA3** Collaboration, J. Badier *et al.*, "psi psi PRODUCTION AND LIMITS ON BEAUTY MESON PRODUCTION FROM 400-GeV/c PROTONS," *Phys. Lett.* **B158** (1985) 85.

[21] D. A. Gunter and V. A. Saleev, "Hadronic production of doubly charmed baryons via charm exitation in proton," *Phys. Rev.* **D64** (2001) 034006, `hep-ph/0104173`.

[22] A. V. Berezhnoi, V. V. Kiselev, A. K. Likhoded, and A. I. Onishchenko, "Doubly charmed baryon production in hadronic experiments," *Phys. Rev.* **D57** (1998) 4385–4392, `hep-ph/9710339`.

[23] J. L. Langland, *Hyperon and anti-hyperon production in p-Cu interactions*. PhD thesis, University of Iowa, 1996. UMI-96-03058.

[24] J. Langland, "Hyperon beam flux parameterization for E781 based on E497 data," H-Note 693, SELEX Internal Report, 1994.

[25] **SELEX** Collaboration, U. Dersch *et al.*, "Total cross section measurements with π^-, Σ^- and protons on nuclei and nucleons around 600 GeV/c," *Nucl. Phys.* **B579** (2000) 277, `hep-ex/9910052`.

[26] P. Mathew, *Construction and evaluation of a high resolution silicon microstrip tracking detector and utilization to determine interaction vertices*. PhD thesis, Dept. of Physics, Carnegie Mellon University, 1997.

[27] N. Bondar *et al.*, "E781 beam transition radiation detector," H-Note 746, SELEX Internal Report, 1995.

[28] **SELEX** Collaboration, A. Atamantchuk *et al.*, "Design and performance of the Fermilab E781 (SELEX) hardware scattering trigger," *Nucl. Instrum. Meth.* **A425** (1999) 529–535.

[29] J. S. Russ, R. Yarema, and T. Zimmerman, "Studies of the LBL CMOS integrated amplifier/discriminator for randomly timed inputs from fixed targer experiments," *IEEE Trans. Nucl. Sci.* **NS-36** (1989) 471.

[30] U. Dersch *et al.*, "Mechanical design of the large angle silicon detectors," H-Note 804, SELEX Internal Report, 1998.

[31] K. Vorwalter, *Determination of the Pion Charge Radius with a Silicon Microstrip Detector System*. PhD thesis, Max-Planck-Institut fur Kernphysik, 1998.

[32] V.Maleev *et al.*, "Description and test results for DPWC and TRD in E781," H-Note 747, SELEX Internal Report, 1995.

[33] **SELEX** Collaboration, J. Engelfried *et al.*, "The E781 (SELEX) RICH detector," *Nucl. Instrum. Meth.* **A409** (1998) 439.

[34] M. K. A. Antonov, G. Dsyubenko, "Geometry of the assembled E781 Photon 1, 2 detectors," H-Note 748, SELEX Internal Report, 1995.

[35] V. V. G. Davidenko, M. Kubantsev, "Photon database for E781," H-Note 767, SELEX Internal Report, 1996.

[36] L. E. T. Lungov, "Vector drift chambers database," H-Note 779, SELEX Internal Report, 1997.

[37] P. Pogodin *et al.*, "Drift chambers of the M1 spectrometer: the detector, electronics and software," H-Note 788, SELEX Internal Report, 1997.

[38] **E687** Collaboration, P. L. Frabetti *et al.*, "Description and performance of the Fermilab E687 spectrometer," *Nucl. Instrum. Meth.* **A320** (1992) 519–547.

[39] **E791** Collaboration, E. M. Aitala *et al.*, "Correlations between D and $\overline{D}$ mesons produced in 500 GeV/c π^--nucleon interactions," *Eur. Phys. J. direct* **C4** (1999) 1–67, `hep-ex/9809029`.

[40] I. Eschrich, *Measurement of the Σ^- charge radius at the Fermilab hyperon beam.* PhD thesis, Max-Planck-Institut fur Kernphysik, 1998.

[41] A. Kulyatsev *et al.*, "E781 hardware trigger preliminary design," H-Note 676, SELEX Internal Report, 1994.

[42] D. M. J. Engelfried, P. Cooper, "The E781 trigger and DAQ System," H-Note 643, SELEX Internal Report, 1995.

[43] **SELEX** Collaboration, J. Russ *et al.*, "Radiative width of the a2 meson," `hep-ex/9901014`. Presented at 29th International Conference on High-Energy Physics (ICHEP 98), Vancouver, Canada, 23-29 Jul 1998.

[44] U. Dersch, *Messung totaler Wirkungsquerschnitte mit* Σ^-*,* p*,* π^- *und* π^+ *bei* 600 GeV/c *Laborimplus.* PhD thesis, Max-Planck-Institut fur Kernphysik, 1998.

[45] J. You, "Event Embedding in SELEX," H-Note 815, SELEX Internal Report, 1998.

[46] **SELEX** Collaboration, S. Y. Jun *et al.*, "Observation of the Cabibbo suppressed decay Xi/c+ –> p K- pi+," *Phys. Rev. Lett.* **84** (2000) 1857–1861, `hep-ex/9907062`.

[47] G. Moliere *Z. Naturforsch* **2a** (1947) 133.

[48] H. A. Bethe, "Moliere's Theory of Multiple Scattering," *Phys. Rev.* **89** (1953) 1256–1266.

[49] G. R. Lynch and O. I. Dahl, "Approximations to multiple Coulomb scattering," *Nucl. Inst. and Methods in Physics Research* **B58** (1991) 6–10.